Towards a Membrane Electrode Assembly for a Thermally Regenerative Fuel Cell

By

Mark A. Skerritt

A thesis submitted to the Graduate Program in Chemistry

in conformity with the requirements for the

Degree of Master of Science

Queen's University

Kingston, Ontario, Canada

April 2013

Copyright © Mark A. Skerritt, 2013

Abstract

The thermally regenerative fuel cell (TRFC) concept that is analyzed is a polymer electrolyte membrane fuel cell (PEMFC), powered by the electro-oxidation of H_2 and the electro-reduction of propiophenone. The main products of this fuel cell should be 1-phenyl-1-propanol and electricity. The 1-phenyl-1-propanol should then be converted back to propiophenone, while hydrogen is regenerated by using waste heat and a metal catalyst (Pd/SiO_2).

The first objective was to find a compatible polymer that would work as either an ionomer/binding agent and as a membrane in the membrane electrode assembly (MEA) of the TRFC. This was achieved by checking the compatibility of each polymer with 1-phenyl-1-propanol and propiophenone (the alcohol-ketone pair). Catalyst coated gas diffusion layers or catalyst coated membranes were made to test the stability of the polymers in the catalyst bed when exposed to the alcohol-ketone pair. If the polymer was compatible with the alcohol-ketone pair, MEAs were constructed using this polymer. The second objective was to test these MEAs inside a H_2/propiophenone fuel cell that would prove the concept of our envisioned TRFC. It was found that the only polymer that was stable in the alcohol-ketone pair was mPBI (m-phenylene polybenzimidazole). The mPBI had to be doped with H_3PO_4 to enable H^+ conductivity. Unfortunately, some H_3PO_4 leached out of the H_3PO_4-doped mPBI when in the presence of the alcohol-ketone pair. MEAs that were created using H_3PO_4-doped mPBI were found to work for H_2/air and H_2/propiophenone fed PEMFCs. The best performance achieved with the H_2/propiophenone powered fuel cell was 6.23 μW/cm2. Unfortunately, the presence of the 1-phenyl-1-propanol product could not be proved by EIS or CV on the fuel cell, or by GC-FID of the cathode effluent. Other unknown products were seen in the GC-FID spectrum of the

cathode effluent. Therefore, it is possible that the propiophenone did reduce at the cathode but it produced an unknown product.

In conclusion, the viability of the proposed TRFC system was not verified. H_3PO_4 leaching from the MEA makes it impossible to use H_3PO_4-doped mPBI as the electrolyte in the final version of the MEA in the TRFC system.

Acknowledgements

Thank you to Dr. Philip Jessop and Dr. Brant Peppley for their stewardship throughout my degree. Your ideas helped to made this project a reality. Both of you are truly an inspiration to science. Thank you to the members of the Jessop Group, especially Vanessa Little and Nurul Choudhury for their help, friendship and understanding. I could not have done this degree without you. Thank you to Dr. Ela Halliop and Dr. Dzmitry Malovich for their support at the Fuel Cell Research Centre, Dr. Franscoise Sauriol for her help with NMR spectroscopy and Dr. Jiaxi Wang for his support with mass spectroscopy. I am also grateful to Steven Cogswell and Dr. Louise Weaver (University of New Brunswick) for their help with SEM and TEM.

Special thanks to my family who have given their full support to me throughout my life. They were there when I needed them the most, through the good times and the bad. Your support has really made a difference to me.

My time at Queen's University has been full of interesting tales. My roommates at all three of my homes over the last two years have taught me many things about life. I wish to especially thank Sarah Ahmed for her company and friendship during the early days of this degree. Certainly the best roommate ever! I would also like to acknowledge all of my friends from Carleton University, especially Andrew Lushington and Ryan Reshke for their unwavering friendship for the last six years. Above all, thank you to everyone who I have had the pleasure of interacting with during this degree. It will certainly be a chapter in my life I will not forget.

Table of Contents

List of Figures

List of Tables

Abbreviations

CCGDL	Catalyst coated gas diffusion layers
CCM	Catalyst coated membrane
CDPS PBI	Cross linked m-phenylene polybenzimidazole membrane
CHU	Carver: hydraulic unit
CV	Cyclic voltammogram
DMAc	Dimethylacetamide
DMF	Dimethylformamide
DMI	1,3-dimethyl-2-imidazolidinone
DMSO	Dimethylsulfoxide
DPS PBI	Danish Power Systems mPBI membrane
EI	Electrochemical impedance
EIS	Electrochemical impedance spectroscopy
ESI-MS	Electrospray ionization - mass spectrometry
FT-IR	Fourier transform - infrared spectroscopy
GE	General Electric
GC	Gas chromatography
GC-FID	Gas chromatography - flame ionization detector
GDL	Gas diffusion layer
GPCP	Gold plated copper plate
HMPA	Hexamethylphosphoramide
HOR	Hydrogen oxidation reaction
HPLC	High performance liquid chromatography
HTPEMFC	High temperature polymer electrolyte membrane fuel cell

IPA	Isopropanol
IR	Infrared
MEA	Membrane electrode assembly
MeOH	Methanol
mPBI	m-phenylene polybenzimidazole
MPL	Microporous layer
MW	Molecular weight
NASA	National Aeronautics and Space Administration
NMP	1-methyl-2-pyrrolidone
NMR	Nuclear magnetic resonance
OCV	Open circuit voltage
ORR	Oxygen reduction reaction
PAA	Poly(allylamine)
PAEB	Polyaniline emeraldine base
PAADP	Poly(allylamine) dihydrogen phosphate
PAMAC	Poly(diallyldimethylammonium) chloride
PAMADP	Poly(diallyldimethylammonium) dihydrogen phosphate
PAMAOH	Poly(diallyldimethylammonium) hydroxide
PBI	Polybenzimidazole
PBI 0.8IV	mPBI powder from PBI Performance Products
PBI S26	26 wt% m-Phenylene polybenzimidazole in DMAc
PC	Polarization curve
PDC	Power density curve
PEM	Polymer electrolyte membrane
PEMFC	Polymer electrolyte membrane fuel cell

PPA	Polyphosphoric acid
PPS	Polyphenylsulfone
PRU	Per repeating unit
PTFE	Polytetrafluoroethylene
PVP	Polyvinylpyrrolidone
PVP 8	Polyvinylpyrrolidone (MW 8,000)
PVP 40	Polyvinylpyrrolidone (MW 40,000)
RHE	Relative to hydrogen electrode
RTMI	Relative to the total mass of the ink
RTMM	Relative to the total mass of the mixture
SEM	Scanning electron microscopy
SEM-BEI	Scanning electron microscopy - backscattered electron imaging
SEM-EDS	Scanning electron microscopy - energy dispersive x-ray spectroscopy
SHE	Standard hydrogen electrode
SS26	Sulfonated m-phenylene polybenzimidazole
TEM	Transmission electron microscopy
TBAF	Tetrabutylammonium fluoride
THF	Tetrahydrofuran
TRFC	Thermally regenerative fuel cell

List of Symbols

α	Charge transfer coefficient/Kamlet-Taft parameter (H^+ donating ability)
β	Kamlet-Taft parameter (H^+ accepting ability)
$\Delta\phi$	Galvani potential
$\Delta\phi_{Anode}$	Anode Galvani potential
$\Delta\phi_{Cathode}$	Cathode Galvani potential
ΔG	Change in Gibbs free energy
$\Delta G^{\ddagger}$	Gibbs free energy of activation
ΔG_{rxn}	Gibbs free energy of reaction
ΔH	Change in enthalpy
ΔS	Change in entropy
η	Reduction in Galvani potential
$\eta_{act\ (A)}$	Overpotential at the anode
$\eta_{act\ (C)}$	Overpotential at the cathode
η_{ohmic}	Voltage drop due to ohmic resistance
π^*	Kamlet-Taft parameter (ability of a solvent to stabilize a charge or dipole)
σ	Conductivity
a	Thermodynamic activity of a reactant or product
A	Cross-sectional area
C^o_R	Bulk concentration of reactant
C^*_R	Reactant concentration in the catalyst layer
e^-	Electron
E	Nernst Voltage
E^0	Thermodynamic cell voltage

E^0_{inc}	Incremental voltage loss
E^0_{Nernst}	Nernst voltage using the bulk concentration of reactants
E^*_{Nernst}	Nernst voltage using the reactant concentration in the catalyst layer
F	Faraday's constant
H^+	Proton
i	Current
j	Charge flux (current density)
K	Electron from the 1st electron shell of an atom
L	Length/Electron from the 2nd electron shell of an atom
M	Metal/Electron from the 3rd electron shell of an atom
n	Number of electrons/Number of repeating units in a polymer
P	Power
R	Resistance/Universal gas constant
T	Temperature
V	Voltage
[X]	Concentration of X
Z_Ω	Impedance due to ohmic resistance
Z_A	Impedance due to the anode charge transfer reaction
Z_C	Impedance due to the cathode charge transfer reaction
Z_i and Z_{img}	Imaginary component of impedance
Z_r and Z_{real}	Real component of impedance

Chapter 1 Introduction

1.1 The energy story: why we need thermally regenerative fuel cells

Utilizing energy from external sources has played an important role in how humanity has evolved over millennia. Arguably, fire was humanity's second attempt at controlling and manipulating energy for our own gain, after crafting tools that utilized our muscles more efficiently.[1] With fire, we could break down starchy foods into smaller sugars that could more effectively fuel the body and the brain.[1] This in turn increased our metabolic efficiency and made us smarter, more able beings.[2] We then proceeded to use the sun to bake our bricks to build our houses and grow our crops.[1] This allowed us to settle down and concentrate on developing new skills other than hunting. These new skills included making art, forming a social order, and creating new products to make life easier. We used oil to power lights more efficiently than wood fire. However, with the advent of the kiln, we could smelt ore to create copper, bronze and iron. These metals replaced chiseled stone as a lighter, easier to mold material. Metalworking brought about great change in how society could function. Iron enabled the industrial revolution, and the arrival of mass production of goods. No longer would we have to do without. We could eat and consume as much as our earnings would allow.

This brings us to the 19th century. Nikola Tesla's invention of electricity would again change the world as we knew it. It would produce energy in a portable form that could be delivered to wherever

and whenever you wanted it. Suddenly, our energy use was centralized, which meant large reactors had to be built to serve the community. At first, these reactors primarily used coal; hydrocarbons that can be harvested from the earth and burned like wood for energy. Wood and charcoal were expensive during the early years of the industrial revolution, so coal was preferred as a cheaper alternative.[1] Unfortunately, coal was very dirty to work with and produced horrible smog in the areas it was used. Coal was also not very portable for the emerging personal transportation industry. The rediscovery of liquid oil would eventually allow personal transport vehicles to work on a more portable fuel. These vehicles would operate on petroleum distillates such as gasoline and diesel.

Oil formed from dead plants that lived in a marine environment millions of years ago.[1] A slow process of heating and pressurizing this organic matter over millions of years created the oil we use today.[1] Oil has been extracted for up to four thousand years and its ancient uses ranged from mummification to caulking boats.[1] Edwin L. Drake was the first person to pump large quantities of oil to the surface in Titusville, Pennsylvania, USA (1859).[1] In just three years, they pumped three million barrels a year from 75 different wells.[1] This increased to half a million barrels a day across the USA in 1909.[1] Although oil is more expensive to extract than coal or natural gas, it still has several advantages. These include better storage capabilities in comparison to natural gas and its liquid nature makes it easy to use in portable applications.[1]

Today, oil is mostly used for its energy, rather than its use as a feedstock for making more complex products, with 47% of the distillate products going towards transport (gasoline, kerosene and diesel), and up to 84% for all energy uses combined.[1] As of 2008, there are 157 Gt (1.13 trillion barrels) of oil reserves in the world, with a demand rate of 3.5 Gt per year (25 billion barrels per year) as measured in 2002.[1,3] World reserves of oil increased by 325 billion barrels between 2000-2009, while average consumption has increased by 26 billion barrels over the same period.[3] Currently we are able to

add extra reserves for future demand. This is due to the discovery of new oil fields and new methods of oil extraction since 2000.[4] However, as emerging markets like China and India catch up to the developed world in the consumption of oil, it is a constant challenge as to whether humanity can keep up with the demand.[1]

The other major concern with oil is that as a combustible, it produces H_2O and CO_2 as products. The concentration of CO_2 in the atmosphere continues to increase due to burning of fossil fuels such as oil, coal and natural gas.[5] Computer models prepared by the scientific community suggest that increasing concentrations of greenhouse gases in the atmosphere is the root cause of our warming world climate.[1] Anthropogenic greenhouse gas emissions are generally regarded as the reason why the climate of Earth is warming.[5] A warming world could cause major problems in some locations around the world. For instance, food supplies could be threatened irrevocably due to changes in the climate. Sea levels could also rise due to melting glaciers and thermal expansion of the oceans, threatening coastal communities with flooding and crop destruction.[5]

In order to prepare our energy market for any complications with the supply of oil, other renewable energy sources need to be considered to fulfill our energy needs. These include wind, solar, biomass, and geothermal. Wind turbines can create electricity from the power of a steady breeze.[5] Photovoltaic cells can convert radiant energy from the sun (light quanta) into electrical energy.[5] Biomass is a renewable organic fuel that can be harvested from plants.[1] Once the biomass is combusted, the CO_2 produced in this reaction will be consumed by other plants via photosynthesis.[1] This will allow new biomass to grow, facilitating further extraction of the biomass fuel. Geothermal energy is heat captured directly from the Earth via the evaporation of liquid water to steam, which then powers a turbine.[5]

Renewable sources are important, but so is the technology used to convert those sources into usable energy. A fuel cell can turn the chemical energy stored in a fuel into electrical energy.[6] However,

the fuel cell is not a source of energy, rather it is a tool to convert chemical energy into usable energy. These fuels may or may not be collected from renewable resources. However, there is another kind of fuel cell that can convert thermal energy from any heat-producing process into electricity through the use of a fuel cell.[7] The heat is used to power an electrochemical cycle in a closed system.[7,8] This fuel cell is called a thermally regenerative fuel cell (TRFC).[7]

If a TRFC system is combined with a diesel-powered vehicle, wasted thermal energy could be captured from the engine to create electricity. An internal combustion engine designed to burn diesel for use in passenger vehicles only uses approximately 20% of the available chemical energy within the diesel fuel to move the vehicle forward.[8] Between 2-10% of the available chemical energy is needed to power electrical equipment via the use of an alternator.[9,10] Of the total available energy, another 6% is lost to overcoming friction and 17% is lost for vehicular idling.[8] The remaining 45-55% of the available chemical energy from the diesel is lost as heat.[10] If enough electrical energy could be produced by a TRFC operating on the waste heat to replace the alternator entirely, then up to 10% more of the fuel's energy could be used for motion instead of auxiliary power.[8] As only 20% of the available chemical energy of the diesel fuel is used to move the vehicle forward, an additional 10% would represent a 50% relative improvement of fuel utilization. If all of the transport trucks in Canada had been fitted with this TRFC system in 2009, then of the 17.3 billion kg of CO_2 that was produced by the trucks,[8] several billion kg could have been eliminated. If applied globally, this could significantly reduce the output of CO_2 into the atmosphere.

The main objective of this work is to fabricate a fuel cell using custom made MEAs that will work under TRFC conditions originally described by Carrier et al.[11]

1.2 Polymer electrolyte membrane fuel cells

There are 5 main types of fuel cell, which are differentiated from one another by their electrolyte.[6] TRFCs have previously been made using H^+ conducting polymer electrolytes.[7,12,13] The TRFC that will be analyzed in this work will also be of the polymer electrolyte type. The 5 main types of fuel cell are listed below.

- Phosphoric acid fuel cell
- Polymer electrolyte membrane fuel cell (PEMFC)
- Alkaline fuel cell
- Molten carbonate fuel cell
- Solid-oxide fuel cell

The PEMFC was invented by Thomas Grubb and Leonard Niedrach at General Electric (GE) in the 1960's.[14] Initially, they created a H_2/air cell that was fueled by hydrogen produced by the hydrolysis of LiH. This fuel cell was sold to the U.S military.[14] The LiH fuel canister was disposable and replaceable, but the amounts of platinum catalyst used in the fuel cell were cost prohibitive at that time.[14]

The National Aeronautics and Space Administration (NASA) was also interested in the PEMFC design. They needed a longer duration fuel source for their Apollo lunar space modules than traditional batteries had given for their Gemini space program. The GE PEMFC design was selected for testing, but due to technical difficulties with O_2 leakage through the membrane, NASA picked an alkali based fuel cell instead. GE continued to improve the technology, and by the 1970's, they had developed PEM water electrolysers for underwater life support. In the 1980's, Ballard Power Systems of Vancouver, Canada

would bring the required refinement and increased power density needed to support new applications, such as the powering of vehicles and portable electronics.

The PEMFC, as shown in Figure 1.1, is a fuel cell that utilizes a membrane sandwiched between two electrodes that contain the electrolyte required for the proton transfer to occur. The membrane provides a gas tight barrier between the anodic and cathodic regions. The membrane electrolyte in addition to preventing gas crossover, is also ion conducting and electrically non-conducting. As a result, the measured voltage (potential) of the fuel cell will be approximately equal to a value that is closer to the theoretical maximum as defined by the Nernst equation. Generally, PEMFCs are powered by hydrogen gas at the anode and oxygen gas at the cathode. Equations 1.1 and 1.2 show the electrochemical half-reactions at the anode and cathode of a H_2/O_2 powered PEMFC. Equation 1.3 shows the net electrochemical reaction of the H_2/O_2 powered PEMFC and a general schematic of a H_2/O_2 powered PEMFC is shown in Figure 1.1.

$$H_2 \rightarrow 2H^+ + 2e^- \quad (1.1)$$

$$O_2 + 4H^+ + 4e^- \rightarrow H_2O \quad (1.2)$$

$$2H_2 + O_2 \rightarrow 2H_2O \quad (1.3)$$

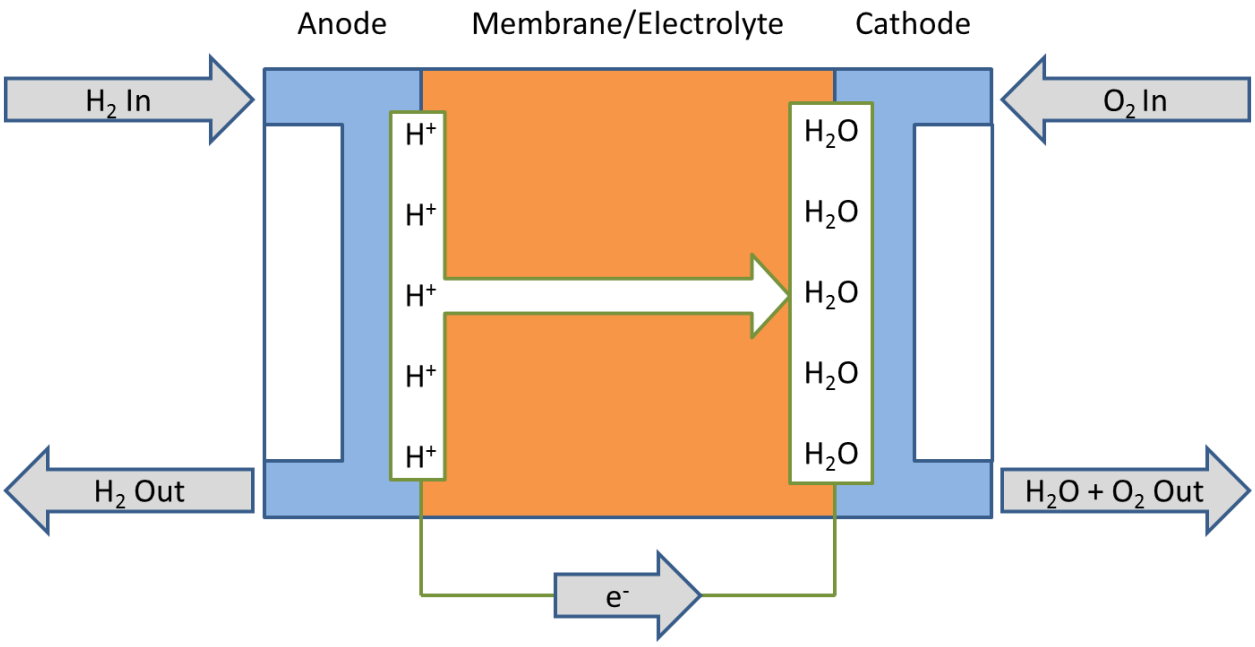

Figure 1.1: A general schematic of a H_2/O_2 powered PEMFC.

For a H_2/O_2 powered PEMFC, oxygen can be supplied directly from the air, whereas H_2 must be supplied from some external source such as a storage tank or a steam-reformer. This means that for applications where large energy storage capacities are required (for example, when greater than 40 kWh equivalent), hydrogen fuel cells can provide greater energy density that can be stored in secondary batteries.[6] In its diatomic form, hydrogen can rival lithium ion batteries on gravimetric and volumetric energy density.[6,15] Therefore, hydrogen gas is not as desirable as batteries for volume sensitive applications, such as portable electronics. For vehicles, hydrogen has the weight advantage over batteries, so the extra volume required can be accommodated either by the use of a hybrid battery-fuel cell, or by sacrificing extra volume within the vehicle to store the hydrogen storage carrier/material. Sources of hydrogen include biomass, fossil fuels, and water.[8] Hydrogen gas itself is not found in significant quantities on earth, and is usually found locked in with another material.

The membrane (as shown in Figure 1.1) must be thin to reduce resistance to ion transport, gas impermeable to reduce gas crossover, and resistant to electrochemical reduction.[6] Most PEMs are made from polymeric materials, and rely on water transfer mechanisms for H^+ conduction. Many of these polymeric membranes are aryl or perfluorinated, functionalized by sulfonic acid groups to promote H^+ transfer.[6]

The main polymeric membrane used in PEMFCs today is Nafion®.[6] It is a variation of a sulfonated polytetrafluoroethylene (PTFE), and utilizes pendant sulfonic acid chains to allow for H^+ conductivity inside a humidified membrane. Another popular membrane is m-phenylene polybenzimidazole (mPBI). This particular membrane does not utilize functionalized acid groups and water as its main H^+ conductors, which allows this membrane to be used at temperatures higher than 100 °C.[16] mPBI itself is poorly H^+ conductive, but can be made conductive by doping the membrane with a strong acid, such as ortho-phosphoric acid.[17] However, sulfonic acid functionalized mPBI membranes can be made, which could utilize water as its main H^+ transfer conductor.[18] The different types of H^+ transfer mechanisms that are used within PEMFCs are discussed in the following section.

1.3 Proton transport mechanisms

There are two mechanisms that are currently considered plausible in the literature.[6,19] These are called the vehicle mechanism and the Grotthus mechanism.[6,19]

The vehicle mechanism is a process by which ions are transported through free-volume spaces by attaching themselves onto a free-flowing species. In the case of Nafion®, or any other sulfonic acid functionalized polymer, the acid groups dissociate protons, where they then attach to a free local water molecule to make hydronium (H_3O^+). Once a potential is applied across the MEA, the hydronium ions travel through the membrane, toward the cathode. Nafion® may have sulfonic acid charge sites but it must have a charge carrier in the form of water to act as an additional electrolyte. This is because there are not enough charge transfer sites on Nafion® to facilitate direct proton transfer between the electrodes.[6,14]

In the Grotthus mechanism, H^+ hop from one transfer site to the next in quick succession to enable H^+ transport between the electrodes.[19] The H^+ transfer site in the case of H_3PO_4 is its hydroxyl groups.[16] The H_3PO_4 H^+ transfer mechanism can be envisioned with a H_3PO_4 molecule next to several others, all exchanging their protons via physical interaction.[16] The potential applied across the MEA drives the movement of H^+ across the membrane, just like the vehicle mechanism. The H^+ transfer mechanism for Nafion®-based PEMFCs uses both Grotthus and vehicle mechanisms, but the vehicle mechanism is thought to dominate H^+ transfer.[20]

1.4 Fuel cell characterization methods and theory

There are many ways to characterize a fuel cell. The main technique is measuring the polarization curve, which shows the voltage as a function of current density. Current density is the electric current in a material (in this case an electrode) per unit area. An example is shown in Figure 1.2. This figure also shows the three major regions of the polarization curve where a voltage is dropped due to intrinsic processes during the operation of the fuel cell.

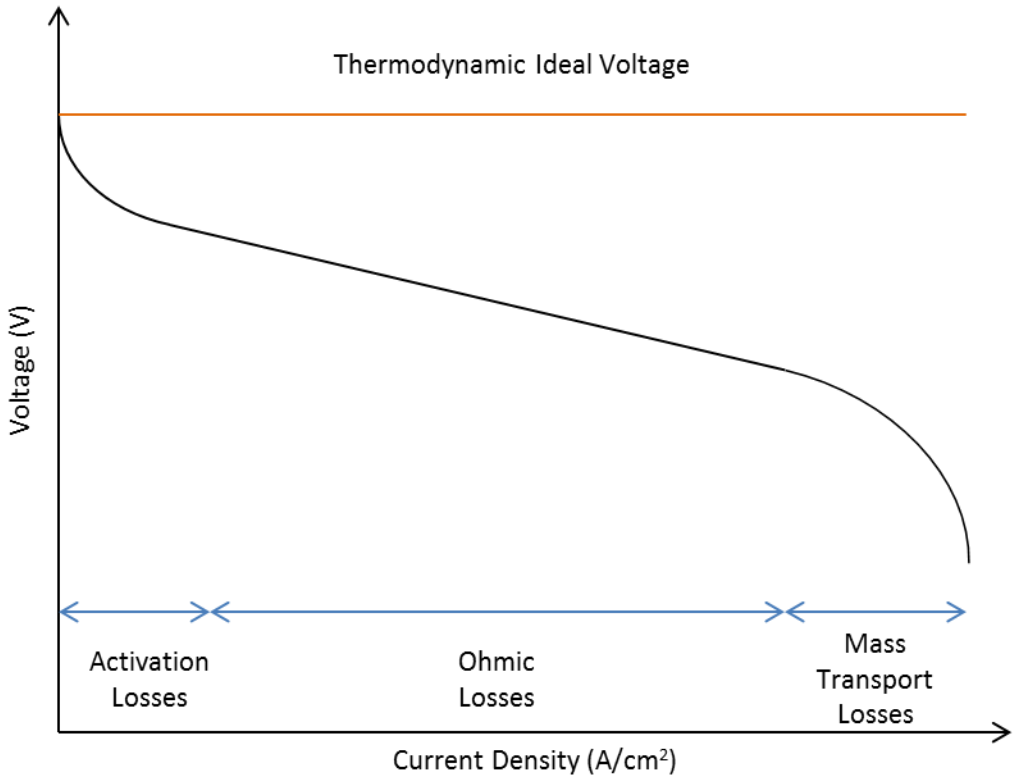

Figure 1.2: Polarization curve of a generic fuel cell, showing the main diagnostic regions of the curve where losses occur.

The activation losses region in Figure 1.2 is due to the kinetics of the electrochemical reaction.[6,14] This region shows a voltage that needs to be sacrificed in order to overcome the activation barrier that is associated with the electrochemical reactions of the fuel cell. A voltage drop is also shown in the ohmic losses region. This voltage drop is caused by an increasing resistance of the charge flow as more current is demanded from the system.[6,14] The mass transport losses region shows a voltage drop due to a lack of available diffused fuel in the electrode structure to provide the current demanded of the system.[6,14]

1.4.1 Activation losses and kinetics theory

The activation losses in the case of a H_2/air fuel cell are mainly due to the kinetics of the oxygen reduction reaction (ORR), which is slow compared to the hydrogen oxidation reaction (HOR) at the anode and cathode, respectively.[6] As an activation energy is required to initiate the reaction, there is a voltage drop associated with driving the electrochemical reaction.[6] An activation overpotential (overvoltage) is a voltage that must be sacrificed to overcome the activation energy of both electrochemical reactions of the fuel cell.[6,14]

At equilibrium, the reverse and forward reaction rates of both HOR and ORR are equal and would yield a zero net current density.[6] The Gibbs free energy of the chemisorbed hydrogen charge transfer reaction is shown in Figure 1.3. Initially, the forward reaction proceeds (Figure 1.3A) as this reaction has a negative Gibbs free energy of reaction (ΔG_{rxn}).[6] However, there will be a buildup of electrons at the electrode and H^+ in the electrolyte until the reaction is at equilibrium.[6] This buildup of

opposing charges creates a voltage between the electrode and the electrolyte as shown in Figure 1.3B (blue line). The blue line in Figure 1.3C shows how this voltage causes the ΔG_{rxn} to equal 0.

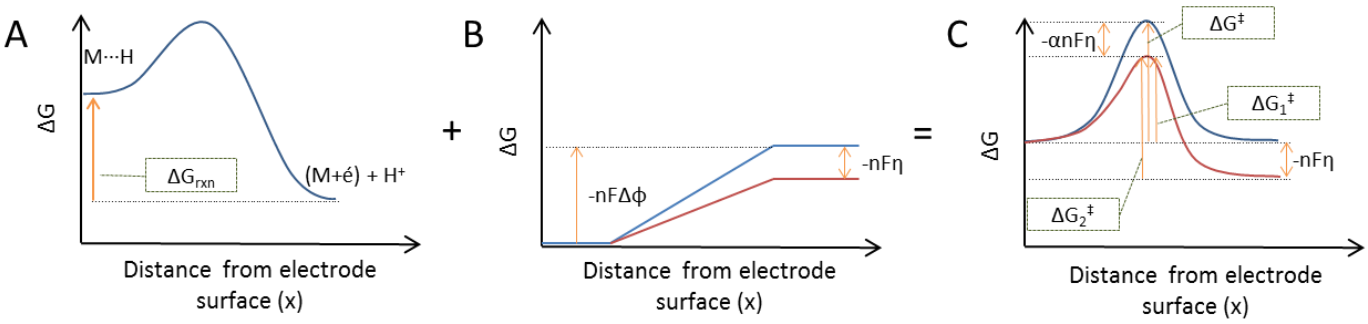

Figure 1.3: At equilibrium (blue lines), the Gibbs Free energy difference of the energetics of the chemisorbed hydrogen charge transfer reaction (A), with the potential difference accumulated over that reaction (B), combines to yield the net ΔG for the charge transfer reaction (C). When the voltage is reduced (red lines), the ΔG shifts from zero (equilibrium) to a negative value (charge transfer reaction proceeds).

Figure 1.3 also illustrates why the activation energy equals the overpotential (overvoltage). As stated previously there is a charge buildup both in electrons and H^+, a potential exists between the electrodes. However, this charge buildup means that the HOR at the anode is at equilibrium. The same is true for the ORR at the cathode. In order to overcome these equilibrium states, the voltage must be reduced to create the favourable conditions for the forward reactions to proceed with a free energy difference of –nFη (red line in both Figure 1.3B and 1.3C). The reduction of the Galvani potential (Δϕ) is represented by 'η' in volts; 'n' equals the number of electrons; and 'F' is Faraday's constant. The same

principles apply to the cathode and produce the overall same result when both anodic and cathodic reactions are taken together. The Δϕ of both the anode and cathode add to form the thermodynamic cell voltage E^0 as shown in Figure 1.4.[6]

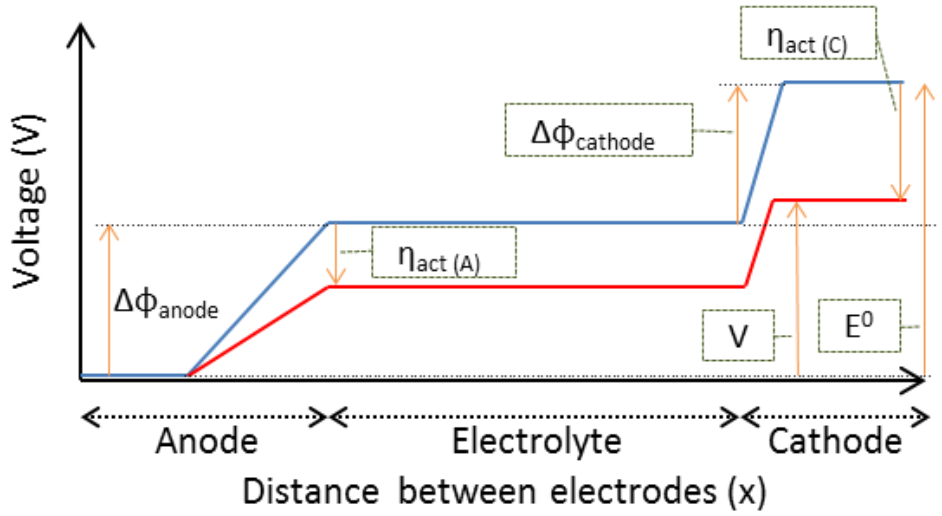

Figure 1.4: A hypothetical voltage profile of a fuel cell MEA at equilibrium (blue) and not at equilibrium (red). The flat slopes between the electrodes are the voltage profiles of the electrolyte (membrane in the PEMFC).

If the equilibrium case for the entire two-electrode and electrolyte system is unsettled by reducing the voltage, as seen in Figure 1.4, it is understood that both half-cell reactions must be reduced to form an overall reduction in voltage.[6] The overpotential is the difference between the thermodynamic, theoretical voltage the system can produce, and the real voltage measured in order for the system to produce a current.[6] In Figure 1.4, overpotential is known as η_{act} and can be calculated by subtracting the measured voltage from the thermodynamic voltage, E^0.[6]

It is also shown in Figure 1.3, that the ΔG difference shown by -nFη is not necessarily the same as the decrease in $\Delta G^{\ddagger}$. The charge transfer coefficient, α, takes into account this difference. α expresses how the change in electrical potential across the reaction interface changes the $\Delta G^{\ddagger}$.[6] The charge transfer coefficient also reflects how each reaction is not symmetrical, because reducing the voltage from E^0 causes the activation barrier of the forward reaction to decrease, while increasing that of the reverse reaction.[6]

Therefore, in order for the reaction to proceed, a voltage drop must be applied to the fuel cell. Without this voltage drop, the HOR and ORR will remain in equilibrium and the fuel cell will not be able to withstand an electrical load.

1.4.2 Ohmic losses and charge transport

The increasing resistance to ion charge flow is another hindrance to maximizing the power of a PEMFC.[6,14] The flow resistance of electrons is generally negligible compared to the flow resistance of ion transfer.[6,14] Increasing the distance between the electrodes, or the thickness of the electrolyte, increases the amount of resistance the ions feel.[6,14] As a voltage has to be applied to the fuel cell in order to transport H^+ and electrons through the electrolyte, an increasing ohmic resistance means that less current will be created at a specific voltage.[6,14] Therefore, if the current is to be kept the same then the voltage must be dropped when the resistance of the fuel cell is increased. Ohmic losses can be minimized by reducing the thickness of the electrolyte or by using a material that is highly ion-conductive.[6,14]

In a PEMFC, H^+ and electrons accumulate at the anode and are consumed at the cathode.[6] This creates a voltage gradient between the two electrodes, driving the transport of H^+ and electrons.[6] However, for H^+ there is also a concentration (chemical potential) gradient within the electrolyte as well.[6] This will also influence the transport of H^+ between the electrodes. However, in most situations the electrical effect of the accumulated H^+ is more influential to the driving force of the fuel cell than the chemical potential effect.[6]

Charge transport is not a frictionless process, as ionic conductors have intrinsic resistance to charge flow.[6] This will result in a voltage loss. The charge flux, as shown in Equation 1.4, can ultimately show this concept.[6] Flux measures the flow of a material per unit area, per second.[6] It differs from flow rate in that it is normalized by cross-sectional area.[6] Charge flux, which is also called current density (C/cm^2s) is useful for measuring the flux of electricity through a medium.[6]

$$j = \sigma \frac{V}{L} \tag{1.4}$$

Equation 1.4 considers the charge flux 'j' of a conductor, with cross-sectional area 'A', conductivity 'σ', and length 'L'. Rearranging the equation to solve for voltage yields Equation 1.5.[6,14]

$$V = j\left(\frac{L}{\sigma}\right) \tag{1.5}$$

Equation 1.5 can be manipulated to resemble Ohm's law (as shown in Equation 1.6) by exchanging current density for current 'i' and coupling the area term 'A' with the length and conductivity. This coupled term is resistance.[6,14]

$$V = i\left(\frac{L}{A\sigma}\right) = iR \qquad 1.6$$

This relationship shows that by increasing the length of the electrolyte between the electrodes the voltage drop increases. It also shows that by increasing ionic conductivity, the voltage drop decreases. Equation 1.6 also describes how an electrolyte of length 'L' and cross-sectional area 'A' must have a resistance value 'R'. Therefore, the voltage must drop in order to allow the ion transfer to occur between the electrodes. Looking back at the voltage profile seen in Figure 1.4, the ohmic losses can now be taken into account as shown in Figure 1.5. Figure 1.5 shows how the overall voltage of the fuel cell has to drop by η_{ohmic} when the ohmic resistance of the electrolyte is taken into account. As a consequence, the total voltage of the fuel cell must also decrease by η_{ohmic}. When the activation energy is taken solely into account, the voltage drop is represented by the red line. The total voltage of the fuel cell in this case is 'V_1'. When both the activation energy and the ohmic resistance of the electrolyte are considered, the voltage drop is exemplified by the green line. The total voltage of this scenario is represented by 'V_2'. The voltage drop due to ohmic resistance can be calculated by using Equation 1.6, where 'R' would represent the total resistance of the fuel cell including ionic and electronic resistance and 'i' is the measured current of the fuel cell.[14] As electronic resistance is negligible, 'R' represents the total ohmic resistance of the fuel cell.[14]

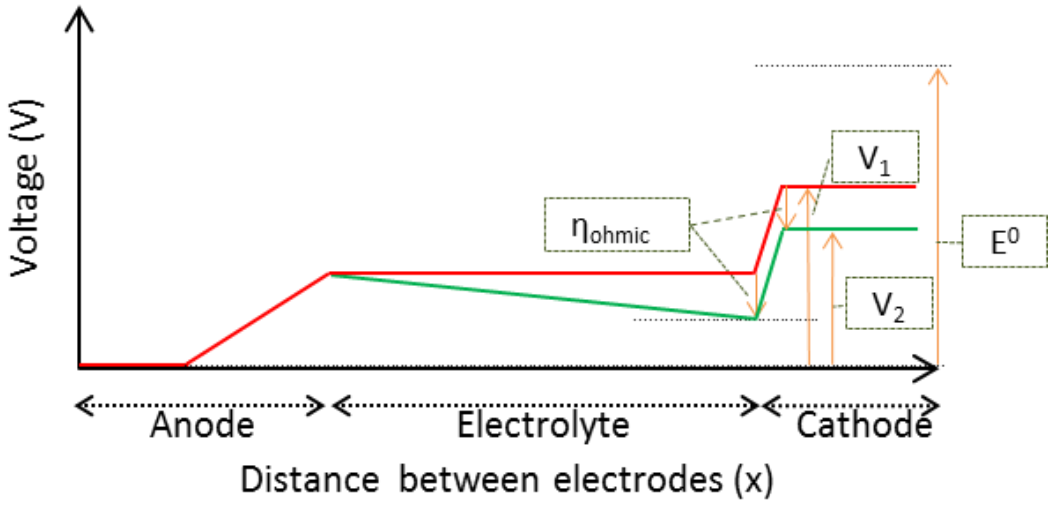

Figure 1.5: Hypothetical voltage profile of a fuel cell taking into account just the voltage loss from the activation energies of both the anodic and cathodic electrochemical processes (red line). The green line represents another hypothetical voltage profile of a fuel cell but includes the activation energy voltage losses shown with the red line as well as the ohmic losses from the electrolyte.

1.4.3 Fuel and waste transport at the electrodes

The way in which fuel is delivered to the fuel cell can have significant effects on its electrochemical performance. Therefore, the fuel must be fed to the catalyst bed in an efficient way to promote the electrochemical performance of the fuel cell. The fuel ratios must also be optimized for the electrochemical reaction to proceed at the highest efficiency. The stoichiometric flow-rate ratio between each reactant flowing to the anode and the cathode, respectively, is defined as the fuel ratio. In a classic PEMFC, this would be the stoichiometric flow-rate ratio between H_2 and O_2. Variables that typically affect the performance of the fuel cell are flow rate; how the fuel is supplied to the catalyst

surface and by what geometry; how the fuel interacts with the electrode; and how the waste is cleared away. The main two regions for fuel transport are the flow structure and the electrode, where the difference between these two regions is scale.[6]

For the flow structure, flow patterns consist of well-defined channel arrays that are amenable to the laws of fluid dynamics. Transport in these channels is dominated by fluid flow and convection, where the flow is considered on the bulk scale to be under the action of a mechanical force.[6] Convection occurs because the fuel is pumped by force through the channel array.[6] High flow rates will ensure that a concentration gradient does not exist between the gas inlet and outlet. As the fuel is constantly reacting over the catalyst surface, the concentration of the fuel would decrease if the flow rate is too slow. A concentration gradient must exist between the flow channel and the catalyst bed. This concentration gradient is the driving force for the diffusion of the fuel inside the electrode to the reaction sites.[6]

For the electrode, the transport of the fuel is dominated by diffusion. The electrochemical reaction within the electrode changes the concentration of the fuel across the thickness of the electrode (Figure 1.6). As the fuel travels through the catalyst layer and toward the membrane, the concentration of the fuel approaches zero. Therefore, the catalyst utilization decreases in these regions and therefore, reduces the overall performance of the fuel cell. As diffusion is driven by this concentration gradient, and transport is not available by convection due to the electrode structure stopping the convective flow, these effects must be tolerated. The gradient between the electrode and the main flow channel is shown in Figure 1.6. The fuel in this case is shown to be H_2 at the anode and O_2 at the cathode.

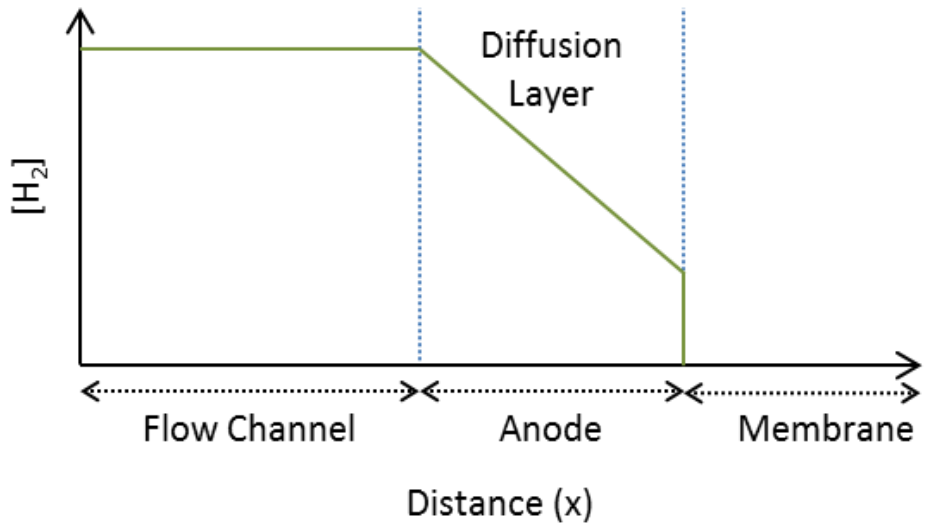

Figure 1.6: General schematic of H_2 concentration within the anode and flow channel of a H_2/O_2 powered PEMFC. This is also true for O_2 at the cathode.

Mass transport losses as shown in Figure 1.2 occur when the concentration ratio of the reactants change between the bulk of the reactants in the flow channel and the reactants present in the catalyst layer.[6,14] This change in ratio is much more pronounced than the natural concentration gradient produced by the diffusion of the reactants in the catalyst layer. The Nernst voltage of the fuel cell will change if this ratio is manipulated. This voltage is the theoretical reversible voltage of an electrochemical reaction.[6] The Nernst voltage is calculated from Equation 1.7.[6,14] The Nernst voltage is represented by 'E'; 'E^0' is the standard state reversible Nernst voltage; 'R' is the universal gas constant; 'T' is the temperature at which the electrochemical reaction is taking place; 'n' is the number of electrons; 'F' is Faraday's constant and 'a' is the thermodynamic activity of the reactant or product. The incremental voltage loss (E_{inc}) due to a decrease in reactant concentration in the catalyst layer can be calculated from Equation 1.8.[6,14] 'E^0_{Nernst}' is the Nernst voltage using the bulk concentration of the

reactants and 'E^*_{Nernst}' is the Nernst voltage using the reactant concentration in the catalyst layer. This is the same voltage loss shown in the mass transport region of Figure 1.2.

$$E = E^0 - \frac{RT}{nF} ln \frac{\Pi a_{products}}{\Pi a_{reactants}} \quad 1.7$$

$$E_{inc} = E^0_{Nernst} - E^*_{Nernst} \quad 1.8$$

Equation 1.8 can be expanded to form Equation 1.9, and then simplified to form Equation 1.10.[6,14] These two equations assume that there is only one reactant in the electrochemical reaction and that product accumulation in the system is irrelevant. 'C^0_R' is the bulk concentration of the reactant and 'C^*_R' is the reactant concentration in the catalyst layer.

$$E_{inc} = \left[E^0 - \frac{RT}{nF} ln \frac{1}{C^0_R}\right] - \left[E^0 - \frac{RT}{nF} ln \frac{1}{C^*_R}\right] \quad 1.9$$

$$E_{inc} = \frac{RT}{nF} ln \frac{C^0_R}{C^*_R} \quad 1.10$$

Waste products, like H_2O in a H_2/O_2 powered PEMFC, are formed as the reactants are stoichiometrically consumed. These products diffuse away from the electrode and into the flow channel where they are transported away from the MEA.[6,14] The structure of the catalyst bed can help remove the waste from the system.[6,21] Changes to this structure can alter the convective flow of the fuel and therefore, possibly improve the diffusivity of the products and reactants of the fuel cell.[6] For example;

PEMFCs can use a hydrophobic microporous layer (MPL) next to the electrode bed.[22] This layer is usually applied to a gas diffusion layer (GDL) that is pressed onto the catalyst layer to enhance H_2O diffusion throughout the electrode structure.[6,22] It has been proven that a MPL applied onto the GDL keeps the membrane hydrated, while reducing the amount of water moving through the electrode bed.[22]

The GDL is usually made from porous, electrically conductive carbon paper or cloth. Carbon paper and carbon cloth are both made from carbon fibre but carbon cloth is a woven fabric whereas carbon paper is not.[23] The GDL allows the excess waste water not dealt with by the MPL to be ejected from the system so it does not flood.[14] Electrical contact is provided by the GDL between the electrode and the flow plates, enabling the current produced by the fuel cell to be collected. The GDL also prevents excess water from the humidified gases (in the case of a Nafion® based system) from entering the catalyst bed.[14] The GDL also allows the fuel to diffuse evenly across the catalyst surface to maximize the contact surface area of the catalyzed membrane.[14]

1.4.4 Other characterization methods

Power density can be calculated from the polarization data by utilizing Equation 1.11 and is representatively shown with its accompanying polarization curve in Figure 1.7.

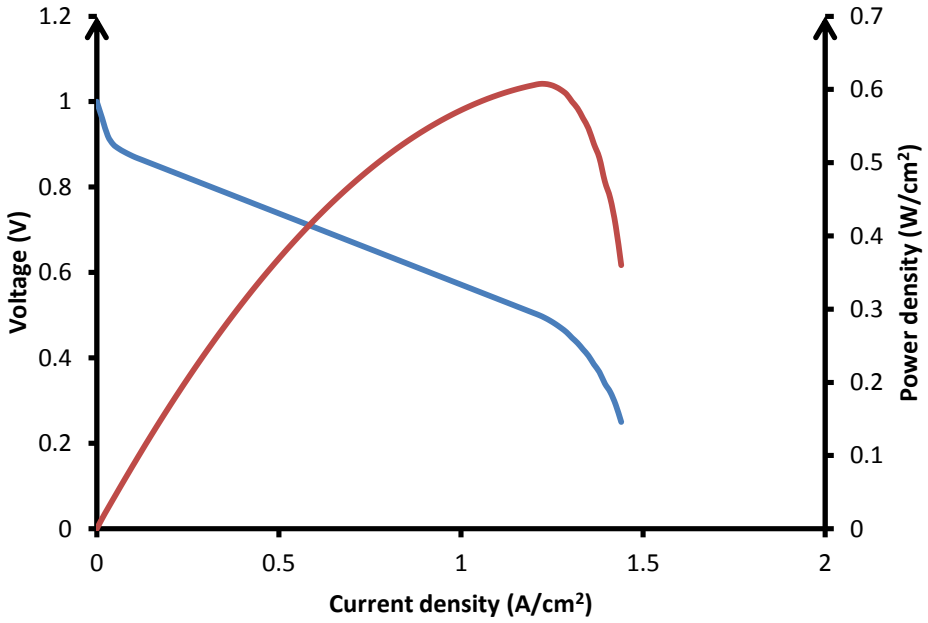

Figure 1.7: Power density versus current density (red line, the power curve) calculated from a typical, associated polarization curve (blue line).

$$P = IV \qquad 1.11$$

Power is directly related to the polarization curve. The maximum power of the fuel cell is usually generated just before the mass transport voltage losses take effect, as shown in Figure 1.7. The power curve is important as it describes the performance of the fuel cell. Power is the rate at which energy is used and the power curve shows where the maximum performance of the fuel cell lies.[6]

Electrochemical Impedance Spectroscopy (EIS) is a characterization technique that can show the ohmic resistance of the electrolyte and the impedance of the reactions happening at each electrode. EIS can more accurately determine where each region as described in Figure 1.2 is occurring and by what quantity, over a polarization curve. Impedance is a measure of the ability of a system to impede electrical flow.[6] Whereas resistance is the ratio of voltage over current, impedance is the ratio between time dependent voltage over time dependent current.[6] This means that impedance can be measured with respect to frequency or time at a constant voltage. This is very useful for time or frequency dependent processes like electrochemical reactions.[6] A Nyquist diagram plots the real component of impedance versus the imaginary component of impedance over a range of frequencies at a specific voltage.[6] The Nyquist plot from a PEMFC can show many characteristics, including the magnitude of the activation losses for the anodic and cathodic electrochemical reactions and the ohmic resistance of the MEA.[6] These characteristics vary depending on the voltage selected for the EIS experiment. EIS can also show if mass transport losses (Warburg impedance) are occurring in the fuel cell. Figure 1.8 is a general Nyquist plot that shows some of the possible characteristics seen when impedance is measured on a PEMFC. The ohmic resistance of the fuel cell at a specific voltage and temperature can be determined by reading the first x-intercept (no imaginary impedance component) on the Nyquist plot. This is shown on the Nyquist plot in Figure 1.8 as 'Z_{Ω}'. This value is recorded at the highest scanned frequency.[6] The frequency is scanned from high to low where the highest value could be up to 1 MHz depending on the capability of the equipment used to capture the impedance data.[6] The lowest frequency value depends on the facileness of the anodic and cathodic electrochemical reactions.[6] If no Warburg impedance is

found then a second x-intercept will occur to complete the cathode activation-losses band. Once this x-intercept is found or if Warburg impedance is measured, the frequency sweep is complete. The anode activation losses (Z_A) may not show in the Nyquist plot for a H_2/O_2 powered PEMFC as the HOR is too facile to capture with EIS.[6] Therefore, it is possible that only the cathode activation-losses band may be seen in a Nyquist plot of a H_2/O_2 powered PEMFC. The cathode activation losses (Z_C) are usually much greater than the anode activation losses in an H_2/O_2 powered PEMFC as the ORR is a much slower reaction than the HOR.[6] The Warburg impedance is a line with a positive slope that shows mass transport losses are occurring.[6] The mass transport losses occur at the lowest measured frequencies.[6]

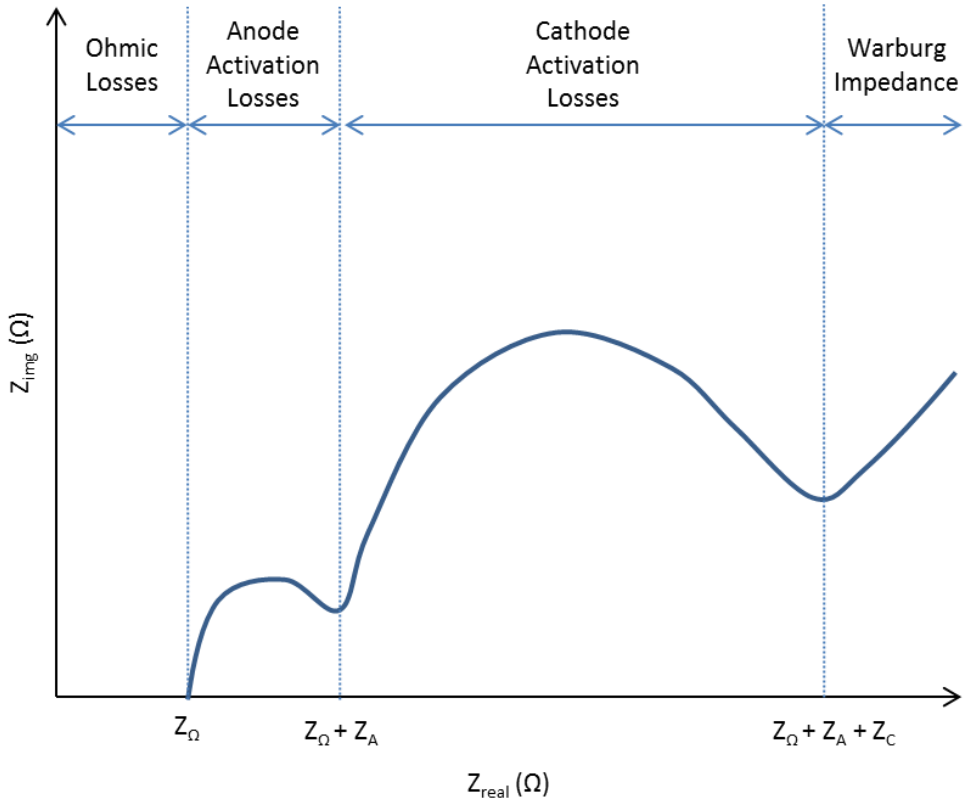

Figure 1.8: A general Nyquist plot from a PEMFC showing some of the possible regions that may appear when measuring the impedance of a PEMFC.

When measuring the impedance of a PEMFC at high voltages, the activation losses of the ORR and HOR will dominate the spectrum.[6] When the Nyquist plot is measured at lower voltages for a PEMFC, Z_A and Z_C will decrease. The Warburg impedance effect is shown when a voltage is selected within the mass transport losses region (lowest voltages) on the polarization curve seen in Figure 1.2.

Gas leak tests for the fuel cell can determine if there are any holes either around the outside of the MEA, or if holes have developed inside the MEA itself. In a basic gas leak test, gas is fed to the anode side of the fuel cell with the outlet tube on the cathode side submerged in water. Both the inlet port on the cathode side and the outlet port on the anode side are blocked. Gas bubbles will appear in the water if there is a leak. In order to detect a leak, the holes would have to be sufficient in number or size as the test is rather primitive. A more accurate technique that can discern pin-holes in the MEA utilizes thermal imaging to find heat that is produced due to the reaction of H_2 with O_2 on the catalyst surface.[24] This reaction is shown in Equation 1.12. Crossover of reactants limits the performance of the fuel cell as it short circuits the desired reaction pathway.[24]

$$H_{2(g)} + \frac{1}{2} O_{2(g)} \rightarrow H_2O_{(l)} + 286\ kJ/mol \qquad 1.12$$

Scanning electron microscopy (SEM) and transmission electron microscopy (TEM) can both be used to analyze the integrity of the MEA. It can determine how much the membrane has swollen or degraded.[25,26,27] It can also determine whether the catalyst has changed morphology or degraded.[28] SEM and TEM have also been used to show whether there has been any physical damage to the MEA.[25,28,29] SEM energy dispersive x-ray spectroscopy (SEM-EDS) can be used to map the distribution of the

elements on the surface of the electrode.[14,29] This technique can show the distribution of the catalyst and the ionomer throughout the catalyst layer of the MEA.

Analyzing the effluent of the fuel cell can also determine the presence and concentration of its products. The presence of products in the effluent would suggest that the desired electrochemical reactions in the fuel cell are working properly. The effluent can be measured by gas chromatography (GC), or nuclear magnetic resonance (NMR) spectroscopy, depending on the product's compatibility with these techniques.

1.5 The ionomer-catalyst interface

Inside a MEA, there is an interface known as the three-phase boundary. It is of great importance to the operation of a PEMFC as these phases are needed to facilitate the electrochemical reactions in the PEMFC.[30,31] The three phases are the ionomer; the catalyst agglomeration; and the voids between them, which are filled with electrochemically active species.[30,31] If the fuel does not react at a triple phase boundary, the fuel cell will not work.[30,31] The boundary is made by the electrolyte reaching into or partially flooding the porous electrode.[32] The fuel must travel in between the voids left by these components and react on an available catalytic site.[30] The ions created at the anode must travel toward the membrane where they continue to the cathode.[30] In order for this to happen, an intermediary step is required. The ionomer uses a delivery mechanism (vehicle or Grotthus) that can take the ions created at the catalyst and transport them to the membrane.[30,31] Ionomers can be polymers or small molecules, with Nafion® being the most common in PEMFCs.[30] However, Nafion® needs liquid water to facilitate H^+ transfer and will not work well with water vapour.[30] For high temperature PEMFCs (>100 °C),

H_3PO_4-doped polybenzimidazole (PBI) may be used as the membrane/electrolyte.[33] H_3PO_4 interacts with the imide of the PBI to create a [$PBI^+H_2PO_4^-$] ion pair.[16] Hydrogen bonding between the phosphoric acid and the PBI immobilize the $H_2PO_4^-$ anions and form a H^+ transfer network using the Grotthus mechanism.[16] This allows the fuel cell to run under anhydrous conditions and therefore, at higher temperatures.[16] For the cathode, O_2 diffuses through the voids and chemisorbs onto the catalyst where it meets a H^+ and creates H_2O.[30] To exit the PEMFC, H_2O must then travel through the voids of the catalyst layer and into the main flow channel beyond the MEA.[30]

The catalyst particles are generally supported by an electrically conductive material to make sure that there is a supply route of electrons to and from the catalyst surface.[30] Without this support, more catalyst would be needed than necessary to facilitate electron conductivity. This is wasteful and expensive, especially if the catalyst contains platinum group elements.

For H_2/air or H_2/O_2 PEMFCs, Pt/C is the preferred supported catalyst for both the anode and cathode.[6] Individual particles measure 20-40 nm in diameter, and Pt/C agglomerates measure 200-400 nm wide.[30] The agglomerated Pt/C contains voids that measure 20-40 nm in diameter, whereas the voids between agglomerated Pt/C clusters measure 40-400 nm.[30] The platinum itself usually measures 2-5 nm and sits on the surface of the carbon.[30] Nafion® ionomeric regions are clusters created via deposition from the catalyst ink that measure 200+ nm wide.[30] These regions are too big to penetrate inside the catalyst agglomerates and can therefore wet only the outside of the catalyst agglomerates.[30] This reduces the activity of the catalyst considerably.

Voids between the polymeric chains of Nafion® are caused by the interplay between its hydrophobic and hydrophilic regions.[30] The pendant chain containing the sulfonic acid group is hydrophilic, whereas the fluorinated carbon backbone is hydrophobic.[30] The backbone is elongated, which allows for good mechanical stability and the pendant chains form hydrate clusters in the presence

of H_2O.[30] Empty space is created around the clusters, which can be filled by either free water or hydronium (H_3O^+).[30] These voids form continuous channels 1-4 nm wide across the catalyst bed, which allow for ionic conduction.[30] These channels contain reactant and either water vapour or liquid water for a Nafion®-based PEMFC. The H^+ species created from the HOR can attach to water to form hydronium and immediately travel inside the hydrated channels of Nafion® to get to the PEM. As the only areas where the water concentration is high enough to facilitate protonation are the triple phase boundaries, that is where the electrochemical reaction is most likely to occur.[30] Figure 1.9 demonstrates the interplay between ionomer, water, reactants, charged species and catalyst.

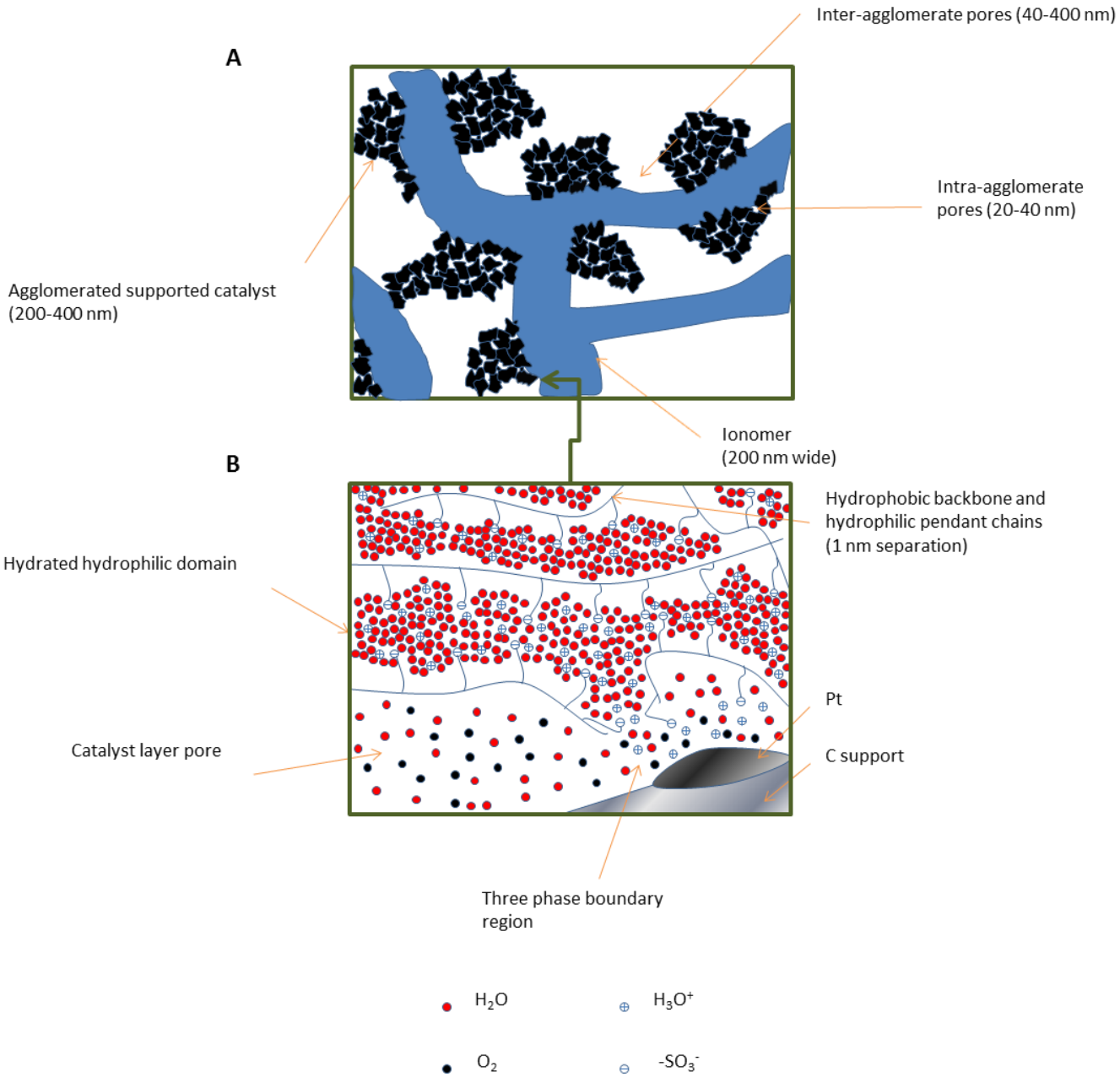

Figure 1.9: A) A macro-view of how the main components of the catalyst layer interact for a Nafion®-based PEMFC. B) The catalyst-ionomer interaction shown at the molecular scale. The structures shown in both A and B are similar for H_3PO_4-doped PBI PEMFCs, where H_3O^+ is replaced with H_3PO_4 and the negatively charged pendants are removed and replaced with negative charges on the polymer backbone.

The interface for phosphoric acid-based PEMFCs is similar, and is also explained by the three phase boundary model by some.[32,34] However, according to Kamat et al., a thin film model is a better fit for this system.[32] The thin film model is described in Figure 1.10. It is a variation on the three-phase boundary, in that the three components are still required in close proximity, but differs in how the reactant and electrolyte interact with the catalyst surface. It details a sandwich of electrolyte between the reactant gas and the catalyst particle.[32] They discovered that the only rate limiting factor is the diffusion of oxygen in the air rather than the electrolyte as the electrolyte layer is thin enough for the rate of diffusion of O_2 to be facile.[32]

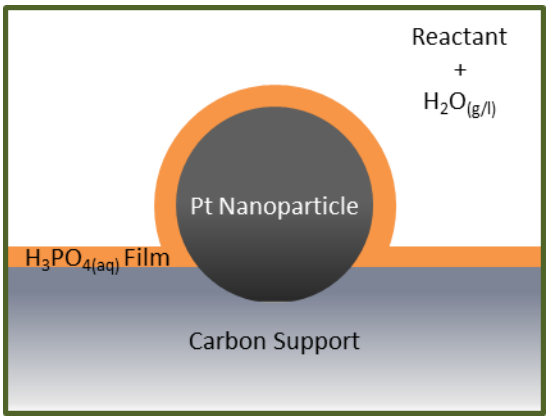

Figure 1.10: A thin-film-boundary electrochemical reaction-zone model for a H_3PO_4 based MEA.[32]

1.6 Thermally regenerative fuel cell

Fuel cells can be used in combinations with other technologies to achieve higher energy utilization for a specific application. An example would be the combination of a PEMFC with lithium ion batteries.[35] In a portable system, the batteries maintain their charge when the appliance is not in use. However, when a PEMFC is combined with the batteries in this system, the fuel cell can act as an external power source to increase the available energy of the system.[35] As the fuel for a PEMFC is external, the fuel can be refilled in as little as 4 min.[35] Unfortunately, batteries are not able to be recharged/refueled in a time frame similar to today's gasoline powered cars.[6,35] A thermally regenerative fuel cell (TRFC) allows captured heat to be turned into electricity via the use of a fuel cell.[11] The way the fuel cell works depends on what reactants are used and how the reactants use the captured heat. There have been several TRFC's proposed over the years.[7,11,12,36,37] The first published TRFC was based on a I_2/PbI_2 concentration cell.[37] Another example of a TRFC was published by Ando et al., who used an aqueous mixture of isopropanol and acetone as the fuel.[7] Isopropanol is oxidized at the anode and acetone is reduced at the cathode (reactions shown in Equations 1.13 and 1.14).[7] Equation 1.13 shows the dehydrogenation at the anode and Equation 1.14 shows the hydrogenation happening at the cathode.

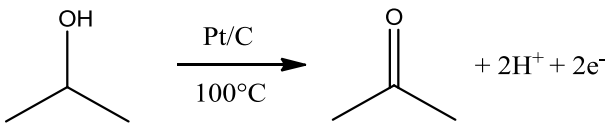

1.13

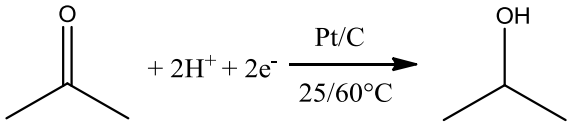

1.14

As the anodic and cathodic reactions of Ando's fuel cell are the forward and reverse of the same reaction, another driving force is required to make the fuel cell work. This can be achieved by changing the temperature between reactions. They envisioned utilizing solar energy to power a heater for the anodic reaction and a cooler for the cathodic reaction.[7] This would introduce a Gibbs free energy differential that would allow the reaction to be spontaneous overall.[7] A later article published by Ando et al. discusses the same system but it uses an external reactor to dehydrogenate isopropanol instead of feeding the isopropanol directly to the fuel cell.[12] This dehydrogenation creates H_2 which is carried to the fuel cell for oxidation.[12] Figure 1.11 shows a diagram of this TRFC system. This version of TRFC system will provide H_2 to the anode where it undergoes oxidation, whilst the previously stated reduction reaction at the cathode remains the same. The isopropanol product is then recycled back to the external reactor. An advantage to applying this system is that the entire fuel cell can run at the same temperature. This ensures that the operation of the fuel cell can be stabilized due to a smaller temperature gradient. The temperature of the dehydrogenation reactor is 82.4°C, whereas the fuel cell is set to either 25°C or 60°C.[7,12] Therefore, due to the thermodynamics of the system the energy captured by the system from the heat applied is small. The total power output was also small as a result. Ando et al. only managed to make 0.6 mW/cm^2 at 50 mA even with the aid of extra H^+ in the form of H_2SO_4.[12] This was achieved with acetone and isopropanol concentrations of 15 v% and 5 v%, respectively.[12] The concentrations of H_2SO_4 and H_2O in this mixture were 20 v% and 60 v%, respectively.[12]

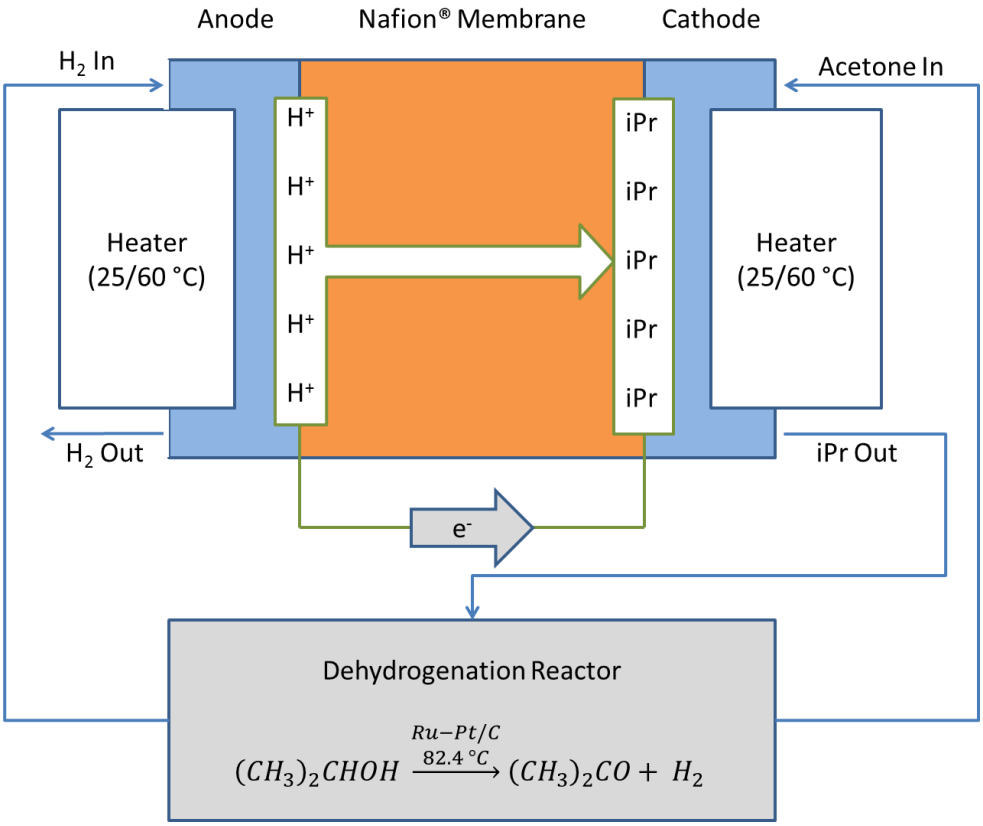

Figure 1.11: A schematic of a TRFC as described by Ando et al.[12] Isopropanol is also described as both 'iPr' and $(CH_3)_2CHOH$. Acetone is also described as $(CH_3)_2CO$.

A similar setup is described by Akimoto.[13] Figure 1.12 shows a general schematic of Akimoto's system. The main difference between his system and the one described by Ando et al. is that the hydrogenation takes place in a separate chamber.[12,13] Another difference is that the dehydrogenation of isopropanol occurs in the gaseous phase instead of the liquid phase.[12,13] The driving force behind Akimoto's system is a concentration cell, where the evolved H_2 from the dehydrogenation splits into H^+ and electrons, travels through a membrane, and then recombines to H_2. A pressure differential between the anode and cathode powers the cell. Isopropanol is then recreated in the presence of H_2, catalyst and acetone under thermo-catalytic (a reaction that occurs in the presence of heat and catalyst) conditions

in the dehydrogenation reactor.[13] This system is complex as it requires multiple chambers in order to split the organic carrier gas and H_2 to ensure that the concentration cell maintains maximum efficacy. The pressure difference of H_2 in the fuel cell is created by the pumps that are positioned in line to both the H_2 feed and the H_2 exhaust. Therefore, the power output from this TRFC must overcome the electrical loads created by the pumps to the system in order for it to be commercially viable.

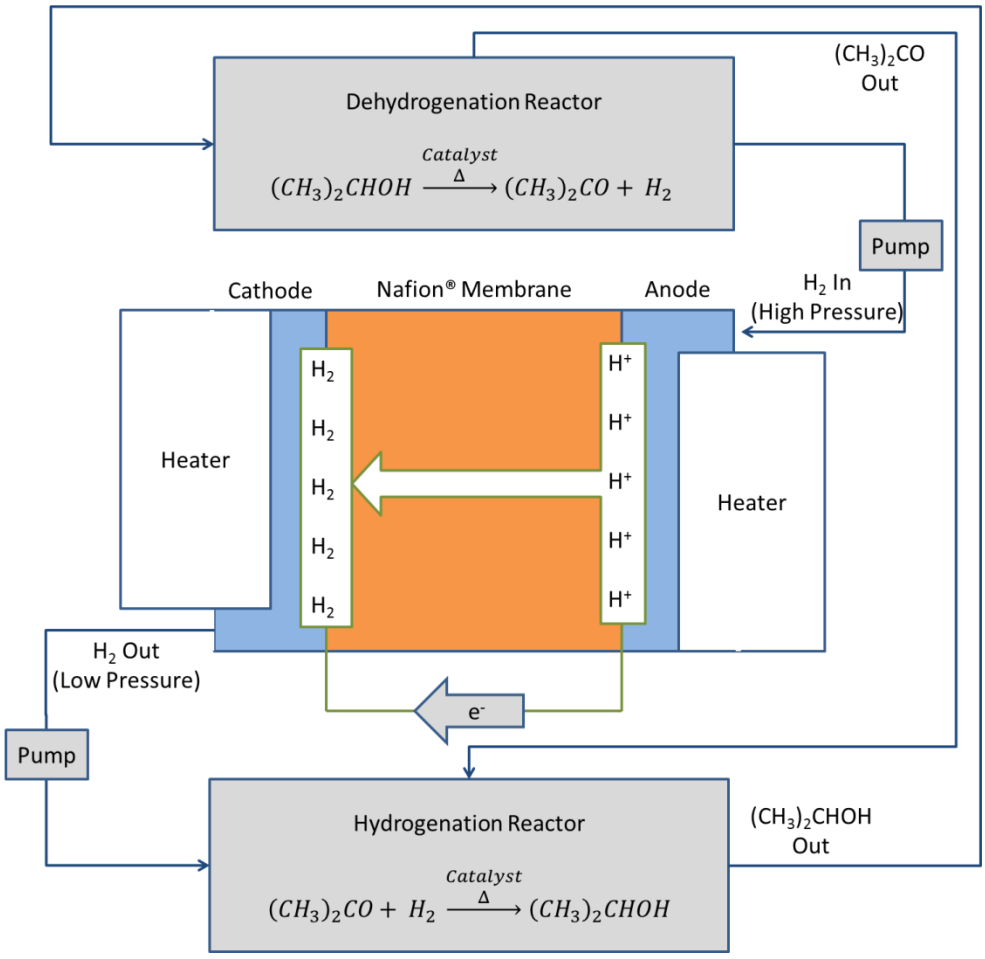

Figure 1.12: A schematic of a TRFC as described by Akimoto.[13] Isopropanol and acetone are described as $(CH_3)_2CHOH$ and $(CH_3)_2CO$, respectively.

The TRFC envisioned by our group is similar to the concepts envisioned by both Akimoto and Ando et al., albeit with some key differences.[11,12,13] It is a system that uses organic liquids with higher boiling points that can both dehydrogenate at high temperature (200-250 °C) and hydrogenate at a lower temperature (100-150°C) in a fuel cell, compared to the lower temperature conditions described by Ando and Akimoto.[11,12,13] The organic liquids in our system are not diluted by a third fluid, as is the case with the Ando and Akimoto systems.[12,13] Figure 1.13 shows a diagram of our envisioned TRFC system. The main application for this TRFC would be to place it inside a large vehicle that contains an internal combustion engine. The TRFC would capture the waste heat from the engine or exhaust system to create electricity.

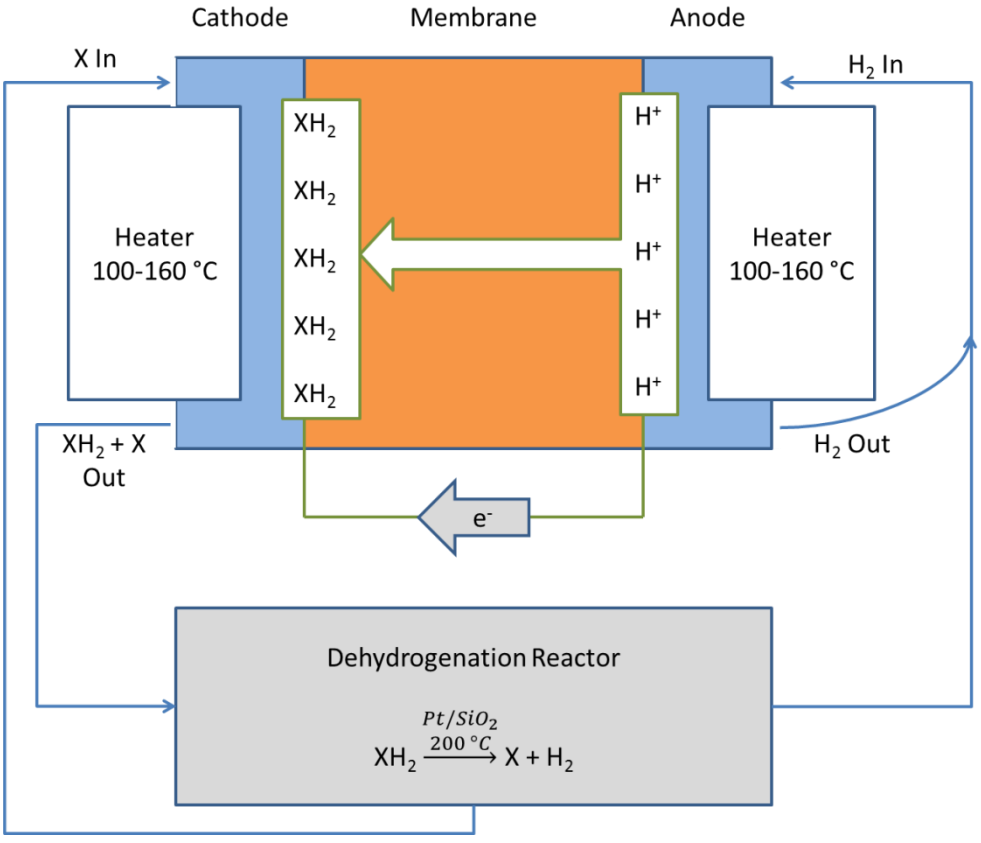

Figure 1.13: A schematic of our envisioned TRFC.[8,11] Propiophenone and 1-phenyl-1-propanol are described as X and XH_2, respectively.

Our system uses an alcohol-ketone pair, just like Ando and Akimoto, but our alcohol-ketone pair has higher boiling points. This pair is 1-phenyl-1-propanol and propiophenone. This pair as a mixture in solution is to be known as the working fluid of the TRFC. Other organic hydrogen carriers were considered, but were deemed inadequate because of poor reversibility, decomposition, weak selectivity, or weak conversion.[38] Organic hydrogen carriers that were not alcohol-ketone pairs were also screened out due to inferior enthalpy of dehydrogenation.[38] A large negative ΔH is necessary to allow for the largest possible ΔG, which would result in a large working voltage within the fuel cell. The reactions for the 1-phenyl-1-propanol/propiophenone system are displayed in Equations 1.15-1.17, where Equation 1.15 represents the 1-phenyl-1-propanol dehydrogenation reaction in a separate chamber, and Equations 1.16 and 1.17 show the anode oxidation (HOR) and the cathode hydrogenation of propiophenone inside the fuel cell, respectively.

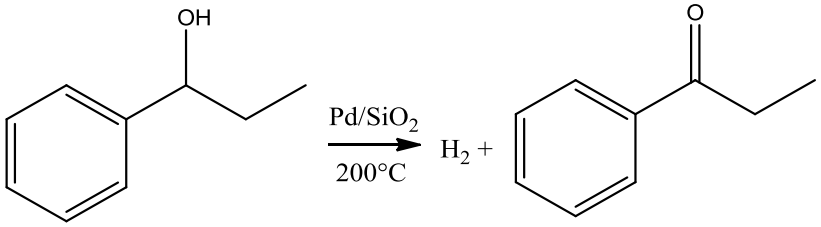

1.15

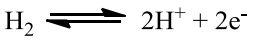

1.16

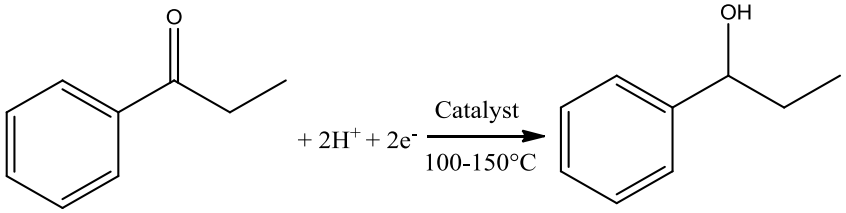

1.17

As the boiling points for 1-phenyl-1-propanol and propiophenone are 208°C and 218°C, respectively, the temperature of the dehydrogenation reactor must be limited to 200 °C. Therefore, the alcohol-ketone pair should also be in the liquid phase in both the fuel cell and the dehydrogenation chamber. However, a large vapour pressure of each compound would exist in the dehydrogenation reactor.

According to Carrier et al. both the hydrogenation and dehydrogenation reactions yield trace amounts of by-products.[11] However, their hydrogenation experiments were achieved via chemical, rather than by electrochemical means.[8,11] Therefore, the mechanism of the chemical hydrogenation reaction may be different than the electrochemical reaction, causing a production of different by-products as a result. Carrier et al. also completed dehydrogenation experiments on 1-phenyl-1-propanol.[11] These experiments were also completed under chemical, rather than electrochemical conditions. As the dehydrogenation happens by chemical means in our envisioned TRFC system, the by-products seen by Carrier et al. would also be produced during the operation of the TRFC. By-products that were seen in the dehydrogenation reaction were propyl benzene, 1-cyclohexylpropane, and 1-cyclohexyl-1-propanol, cyclohexyl ethyl ketone, and 1-cyclohexyl ethyl ketone.[11] As there is convergence between the dehydrogenation and hydrogenation reactions, many of the by-products are shared between the two processes.[11]

The enthalpy and entropy of hydrogenation for propiophenone at 100 °C are -56.3 kJ/mol, and 119.1 J/molK, respectively.[11] Equation 1.18 shows how the Gibbs free energy of the reaction could be calculated using the values of ΔH and ΔS as stated above. Equation 1.19 shows the relationship between Gibbs free energy and voltage. The theoretical maximum voltage of an electrochemical system can be calculated using this equation by solving for 'E' once the ΔG of the electrochemical reaction is known. This theoretical maximum should be the best open circuit voltage that the system can handle.

$$\Delta G = \Delta H - T\Delta S \quad 1.18$$

$$\Delta G = -nFE \quad 1.19$$

Therefore, using the thermodynamic data made available by Carrier et al. the theoretical maximum voltages for a fuel cell running on H_2 and propiophenone at 100 °C and 140 °C are 61.5 mV and 36 mV, respectively.[39] These values were calculated assuming there was no variance of ΔH and ΔS with temperature.

1.7 Objectives

There are two main objectives to complete for this work. The first is to describe which polymers are compatible as membranes and ionomers in the TRFC system. Propiophenone and 1-phenyl-1-propanol are very good solvents, so solubility and degradation tests must be completed on selected polymers. Polymers also need to be screened for their compatibility inside the system as a whole. Polymers that would be unstable as a membrane in highly acidic conditions and high temperatures will be avoided. Polymers that swell too much in the presence of propiophenone or 1-phenyl-1-propanol are to be avoided, as crossover of fuel or oxidant is unacceptable in a fuel cell. Currently there are no commercially available membranes that must meet the operating requirements of the TRFC. Membranes made from acceptable polymers will be created by casting the polymer into a film. Sufficient focus will be placed on developing polymer matrices that can facilitate H^+ transfer under

anhydrous conditions by using H_3PO_4 as the H^+ transfer medium. In order to create an MEA, some catalyst coated GDLs or membranes must be made with ink solutions containing these polymers. These ink mixtures, results and application techniques will also be described.

The second objective is to test a MEA in a fuel cell that re-hydrogenates the ketone as would occur in the complete TRFC system. In order to test the initial viability of the MEA, the MEA will initially be tested in a fuel cell under H_2/air. Prepared MEAs placed inside a fuel cell setup will be tested via some of the characterization methods discussed above. These characterization tests will prove whether the fabricated MEA was assembled correctly, and whether or not the TRFC actually functioned as expected.

Chapter 2 Experimental Procedures

2.1 Materials

The following compounds were purchased from Sigma Aldrich:

- Nafion® 117 solution (31175-20-9, 5 wt% in aliphatic alcohols)
- Polyvinylpyrrolidone (PVP40) (9003-39-8, 40,000 MW)
- Polyaniline emeraldine base (PAEB) (25233-30-1, 20,000 MW)
- Isethionic acid sodium salt (1562-00-1, 98%)
- Polyphosphoric acid (8017-16-1, 115% H_3PO_4)
- Calcium chloride anhydrous (10043-52-4, 99.99%)
- Hexamethylphosphoramide (HMPA) (680-31-9, 99%)
- Polyphenylsulfone (PPS) (SKU: 428310, unknown MW)
- Poly(diallyldimethylammonium) chloride solution (PAMAC) (26062-79-3, 20 wt% in H_2O, 400,000-500,000 MW)
- Silver nitrate (7761-88-8, 99.0%)
- Amberlite® MB20 (SKU: 74451)
- 1-phenyl-1-propanol (93-54-9, 97+%)
- Butadiene sulfone (77-79-2, 98%)
- Tetrabutylammonium fluoride hydrate (TBAF) (22206-57-1, 98%)

- Sodium fluoride (7681-49-4, 99.99%)
- Glycerol (56-81-5, 99.5+%)
- Poly(allylamine) solution (PAA) (30551-89-4, 20 wt% in H_2O, 65,000 MW)
- Lithium chloride (7447-41-8, 99+%)
- Formic acid (64-18-6, 95+%)
- Fuming sulfuric acid (8014-95-7, 30% free SO_3)
- 1-methyl-2-pyrrolidone (NMP) (872-50-4, 99.5+%)
- 1,3-dimethyl-2-imidazolidinone (DMI) (80-73-9, reagent grade)
- Platinum on Vulcan XC-72 (40 wt% Pt loading on XC-72 carbon)
- Celite® 545 (68855-54-9)

The following compounds were purchased from Acros Organics:

- Polyvinylpyrrolidone K16 18 (PVP8) (9003-39-8, 8,000 MW)
- Propiophenone (93-55-0, 99%)

The following compounds were purchased from Premetek:

- Platinum on Vulcan XC-72 (P30A200, 20 wt% Pt loading on XC-72 carbon)
- Platinum on Vulcan XC-72 (P30A400, 40 wt% Pt loading on XC-72 carbon)

The following materials were purchased from The Fuel Cell Store

- SpectraCarb® 2050-A carbon paper
- Untreated carbon cloth (SKU: 7302003)
- Nafion® 117 membrane (SKU: 591239)

The following materials were purchased from PBI Performance Products:

- m-Phenylene polybenzimidazole (PBI 0.8IV, powder) (SKU: 90330)
- m-Phenylene polybenzimidazole (PBI S26 solution, 26 wt% in dimethylacetamide, 1.5 wt% LiCl)

The following membranes were donated by Danish Power Systems:

- m-Phenylene polybenzimidazole membrane (DPS PBI)
- Cross linked m-phenylene polybenzimidazole membrane (CDPS PBI)

The following materials were purchased from Fibre Glast:

- Kevlar® hybrid sample pack (SKU: 4004-A)
- Kevlar® pulp (SKU: 544-A)

The following compound was purchased from TCI America:

- Dimethylacetamide (127-19-5, 99.0%)

Various adhesives that were used to make custom templates for membrane casting:

- Seal-All: Contact Adhesive and Sealant
- LePage: Speed Set Epoxy
- LePage: Multi-Surface Adhesive Gel
- GE: Silicone I (All Purpose)
- Instant Krazy Glue

Various gases that were used

- MEGS: hydrogen gas (SKU: UN1049)
- MEGS: nitrogen gas (SKU: UN1066)
- Praxair: high purity argon gas
- Praxair: Ultra Zero compressed air

List of instruments, equipment and software used

- Autolab version 4.9.007 for Windows
- Autolab potentiostat (SKU: PGSTAT302N)
- Waters: 515 HPLC pump (SKU: WAT207000)
- Barnant: Temperature Controller 689
- Arbin Instruments: BT-2000 battery test station
- MITS Pro version 3.0, build 5.28 (software control centre) for Arbin Instruments BT-2000
- Fluke: 8840A multimeter

- Hioki: 3560AC milliohmmeter
- MKS Instruments: Mass FLO Controller (SKU: 1179A13CS1BV)
- Iwata: Eclipse HP-CS airbrush
- Fisher Scientific: FS30 Ultrasonic Cleaner
- Fisher Scientific: Sonic Dismembrator 100 with ultrasonic converter
- 2 steal square hole templates: 2.54 cm bezel, 1 cm x 1 cm square hole in centre, 3 mm thickness
- 2 steal square hole templates: 2.54 cm bezel, 2.22 cm x 2.22 cm square hole in centre, 3 mm thickness
- Plas-tech Fabrications: Plexiglas templates x2: 3 cm bezel, 1 cm x 1 cm square hole, 6 mm thick.
- Scientific Industries: Vortex Genie 2
- Mettler Toledo: New Classic MF ML204 mass balance
- Mettler Toledo: SB12001 mass balance
- Mettler Toledo: Volumate Liquisystems 20-200 µL micropipette
- Gilson: Pipetman 1000 µL micropipette
- Shimadsu: GC-17A gas chromatograph
- Shimadsu client/server version 7.3, build 18
- Nicolet Avatar: 360 FT-IR spectrometer
- EZ Omnic E.S.P 5.2 software for Nicolet Avatar: 360 FT-IR spectrometer
- Millipore: Synergy UV (SKU: SYNSV0000) water deionizer
- Fisher Scientific: Micromaster microscope
- Westover Scientific: Micron 2.0.0, revision 2962 for Fisher Scientific Micromaster microscope
- Fisherbrand: microscope slides
- Fisher Scientific: Isotemp 281A vacuum oven
- Procise 210-2372 Vernier caliper

2.2 Polymer preparation

2.2.1 Poly(diallyldimethylammonium) dihydrogen phosphate (PAMADP)

Amberlite® MB20 was poured into a chromatography column until it reached the bottom of the reservoir bulb. Poly(diallyldimethylammonium) chloride solution in H_2O (PAMAC) was added in concentrations of either 2.0 wt%, 5.4 wt%, 7.9 wt% or 20 wt%. A positive pressure of argon was then applied to the top of the column to facilitate the initial movement of the solution down the column. Depending on the concentration of PAMAC, a positive pressure of argon may also be required to push the solution through the column in its entirety. The flow of argon was moderated at the bottom end of the column using a PTFE stopcock. The aqueous yellow-tinged product (poly(diallyldimethylammonium) hydroxide solution in H_2O) (PAMAOH) was collected into a beaker. Once collected, the product was tested with $AgNO_3$ to determine if the PAMAC had reacted completely. The solution was then acidified by 85% $H_3PO_{4(aq)}$ to create PAMADP for use in a catalyst ink. The amount of acid added would reflect the desired number of equivalents of H_3PO_4 per repeating unit of PAMADP in the catalyst ink as shown in Table 3.9. Amberlite® MB20 was then regenerated with 4.5 M $KOH_{(aq)}$ and washed with H_2O to eliminate all of the free KOH. PAMAOH would have been subjected to further treatment through Amberlite® MB20 if the ion exchange was not complete. React-IR spectrum (H_2O) 2347 cm^{-1} (m, P-O stretch, $H_2PO_4^-$)[40], 1181 cm^{-1} (s, P=O stretch, $H_2PO_4^-$)[40], 1076 cm^{-1} (m, P=O stretch, $H_2PO_4^-$)[40], 997 cm^{-1} (s, P-O stretch, $H_2PO_4^-$)[40], 954 cm^{-1} (m, P-O stretch, $H_2PO_4^-$)[40]. Titration of 0.25 wt% aqueous PAMAOH with 12 mM $HCl_{(aq)}$ established that the polymer was actually a PAMAC/PAMAOH copolymer with a mole

ratio of 9:1. It was then assumed that acidification of this copolymer with H_3PO_4 would react with all of the ^-OH sites to yield PAMAC/PAMADP in a mole ratio of 9:1.

2.2.2 Poly(allylamine) dihydrogen phosphate (PAADP)

PAA solution was acidified directly with the addition of 85% $H_3PO_{4(aq)}$ to yield PAADP. The amount of H_3PO_4 added was either stoichiometric or 3 eq of H_3PO_4 per repeating polymeric unit. However, the amount of acid added in both cases should have been sufficient to create the $H_2PO_4^-$ salt at every available amine site on the polymer. React-IR spectrum (H_2O) 1583 cm^{-1} (s), 1263 cm^{-1} (s), 1096 cm^{-1} (s), 1021 cm^{-1} (s), 798 cm^{-1} (s).

2.2.3 Sulfonated m-phenylene polybenzimidazole (SS26)

PBI membrane strips (1.09 g total, approx. 2 mm x 5 mm each strip) and fuming sulfuric acid (100 mL) were placed inside a 250 mL round bottom flask, along with a magnetic stir bar. The contents of the flask were heated to 80 °C by a silicone oil bath and then magnetically stirred for 6 h. In less than 1 h, the PBI membrane had dissolved. After the 6 h period, the product was precipitated out of solution by adding it drop-wise to 400 mL of 4.9 M $KOH_{(aq)}$. This volume of the mixture was increased to 3 L with distilled H_2O to dissolve the precipitated sulfates that had come from the neutralization of H_2SO_4. However, the product still remained out of solution as a potassium salt during this time. The mixture was then vacuum filtered using a Buchner funnel to collect the potassium salt of the desired product.

The product was then washed with room temperature deionized H_2O until the filtrate was pH neutral. The product was placed in a vacuum oven at 100 °C overnight to dry. ^{1}H NMR spectrum (ppm) (DMSO-d_6) δ 7.1-9.4 (br, m). ^{13}C NMR spectrum (ppm) (DMSO-d_6) δ 125-136 (br, m), δ 152-153 (br, m), δ 154-156 (br, m). FT-IR spectrum (KBr pellet), 3421 cm^{-1} (b, N-H stretch), 1623 cm^{-1} (m, C=N stretch),[41] 1533 cm^{-1} (m), 1461 cm^{-1} (m), 1425 cm^{-1} (m), 1279 cm^{-1} (m), 1190 cm^{-1} (m, S=O stretch),[41] 1139 cm^{-1} (m, S=O stretch, H_2SO_4),[41] 1051 cm^{-1} (m, S=O stretch, R-SO_3H).[41]

The FT-IR spectrum was collected by creating a KBr pellet (1.5 mg SS26 to 100 mg KBr) and using a Nicolet Avatar 360 E.S.P. to collect the FT-IR spectrum.

2.3 Ink preparation

2.3.1 Nafion®

The Nafion® starting material is a pre-dissolved mixture of aliphatic alcohols and Nafion® polymer. A solubility trial was conducted using a number of solvents to determine if they could replace aliphatic alcohols in this mixture to aid in faster evaporation of the solvent. This is shown in Table 3.1. Once a solvent was selected, the Nafion® in aliphatic alcohols solution was evaporated to dryness. The resulting film was re-dissolved into the new solvent at 5 wt%. Pt/C (10 wt% Pt loading on carbon) was then added to varying concentrations of 10 wt%, 15 wt%, and 20 wt% Pt/C relative to the total mass of the mixture (RTMM). This mixture is now an ink. After the ink had been mixed, a sonicator bath (Fisher Scientific: FS30) was used to sonicate the ink for 15 min at 100 W.

2.3.2 Polyvinylpyrrolidone and Nafion® blend

A solution of 2.5 wt% Nafion® and 2.5 wt% PVP8 or PVP40 was created in MeOH. Pt/C was then added to the solution (10 wt% Pt loading on carbon) to make its concentration in the solution 10 wt% Pt/C, RTMM. This ink was sonicated in a sonicator bath for 20 min at 100 W just before deposition.

2.3.3 Poly(diallyldimethylammonium) dihydrogen phosphate

Aqueous PAMAOH solution in concentrations of either 2 wt%, 5.4 wt% or 7.9 wt% were acidified with H_3PO_4 to a varying amount of equivalents (Table 3.9) of H_3PO_4 per repeating unit of the polymer to make PAMADP in the acidified H_2O solution. The PAMADP in this acidified H_2O solution was then reduced in mass fraction to between 1-5 wt% PAMADP (relative to the total mass of the ink, RTMI) by the addition of glycerol and Pt/C (10 wt% Pt loading on carbon) to create an ink. Glycerol concentrations were 0 wt%, 2 wt% or 5 wt% (Table 3.9), (RTMI). Pt/C concentrations were 5 wt% or 10 wt% in solution, RTMI. The ink was exposed to a sonicator bath for 15 min at 100 W before application.

2.3.4 m-Phenylene polybenzimidazole (PBI S26 and DPS PBI)

The following procedures (**A**-**C**) were used to create different variations of m-phenylene polybenzimidazole inks.

A) The 26 wt% PBI S26 solution in DMAc was diluted to 2 wt% by adding more dimethylacetamide. The total amount of PBI S26 solution would be 0.850 g, or 85 wt% of the total mass of the ink. The 0.850 g of PBI S26 solution was poured into a 5 mL glass vial. Glycerol was added to this solution at a concentration of 5 wt%, RTMI. Pt/XC-72 (20 wt% Pt loading on XC-72 carbon) or Pd/XC-72 (20 wt% Pd loading on XC-72 carbon) was then poured into this solution to create an ink at a concentration of 10 wt%, RTMI. A sonicator probe (Fisher Scientific: Sonic Dismembrator 100 with ultrasonic converter) was used to sonicate the ink in this 5 mL vial for 1 min at 0.05 W.

B) A variation of the previous procedure included upgrading Pt/XC-72 and Pd/XC-72 to 40 wt% Pt/Pd loading on XC-72 carbon. Isopropanol and deionized water were also added to allow for easier evaporation of the ink. The ink contained a mixture of PBI S26 polymer, dimethylacetamide (DMAc), isopropanol, deionized H_2O, glycerol and Pt/XC-72, in a w/w ratio of 2:43:40:5:3, respectively, RTMI. With Pd/XC-72 (40 wt% Pd loading on XC-72 carbon), the ratio changed to 2:63:20:5:3 as the PBI polymer precipitated with the 2:43:40:5:3 w/w ratio. At first, in one 5 mL glass vial the 2 wt% PBI S26 solution in DMAc was diluted with glycerol. In a second 5 mL glass vial, isopropanol and water were mixed with the catalyst and agitated via a Vortex Genie. The two solutions were combined by pipetting the PBI S26 solution into the Isopropanol

ink, which together measured a total of 1 g. The same sonicator probe as **A** was used to sonicate the final ink for 1 min at 0.05 W.

C) Seland et al. provided the third method that was used, although with some alterations.[34] The PBI that was used was DPS PBI. Three separate inks were made to deposit as sequential layers on the surface of the carbon paper. For the first ink preparation, 0.31 g of glycerol (10 wt%, RTMI) was dissolved in isopropanol. Activated carbon (Vulcan XC-72) was then added to the mixture at 10 wt% concentration, RTMI. This ink was sonicated by the same sonicator probe as **A** for 1 min at 0.20 W. For the second preparation, a 50:50 w/w solution of isopropanol and deionized H_2O was created. Vulcan XC-72 carbon was added to the mixture at 10 wt% (RTMM), and sonicated at 0.20 W for 1 min. For the third preparation, 38.1 mg of DPS PBI was dissolved in 2.50 g of DMAc at 150 °C using a silicone oil bath. When cooled to room temperature, 296 mg of Pt/C (10 wt% Pt loading on XC-72 carbon, 10 wt%, RTMI) and 148 mg glycerol (5 wt%, RTMI) were added to the DMAc solution. The concentration of DPS PBI was 1.26 wt%, RTMI. This ink was then sonicated using the same sonicator probe seen in **A** at 0.20 W for 1 min.

2.4 Membrane casting

2.4.1 Poly(diallyldimethylammonium) dihydrogen phosphate

The following procedures (**A**-**C**) are three different ways PAMADP was prepared as a membrane.

A) A PAMAOH aqueous solution (2 wt% PAMAOH in H_2O, 70 g total mass) was acidified by adding 1 g of 85% $H_3PO_{4(aq)}$ in a beaker. The predicted yield of PAMADP was calculated to be 90%, or 0.90 eq of H_3PO_4 per repeating unit of PAMADP, assuming that all of the H_3PO_4 reacted with PAMAOH. This PAMADP solution was reduced in volume to 20 mL at 100 °C using a hot plate, poured into a glass petri dish and further evaporated to dryness at 94 °C using a hot plate.

B) A PAMAOH aqueous solution (2 wt% PAMAOH in H_2O, 20 g total mass) was acidified by adding 0.76 g of 85% $H_3PO_{4(aq)}$. This amount of H_3PO_4 should equal 1.4 eq of H_3PO_4 per repeating unit of PAMADP. This acidified solution was reduced in mass to 2 g by evaporation at 100 °C using a hot plate. The 2 g of solution was cast onto a small glass petri dish (5 cm diameter) and placed into a vacuum oven at 50 °C overnight to yield a clear film that stuck firmly to the glass.

C) A PAMAOH aqueous solution (2 wt% PAMAOH in H_2O, 10 g total mass) was acidified with 0.14 g of 85% H_3PO_4 to produce PAMADP in a predicted 85% yield assuming that all of the available acid reacted with the PAMAOH. The solution was then poured into a Teflon® lined glass petri dish (5 cm diameter). The dish was placed inside a vacuum oven at 50 °C and left overnight to yield a non-uniform clear membrane. The membrane separated with ease from the liner.

2.4.2 m-Phenylene polybenzimidazole (PBI S26)

A template consisting of a plate glass floor (15 cm x 15 cm) and a steel cylinder (12 cm diameter) wall was constructed (Figure A6, appendix). These two objects were held together by gravity. The cylinder and the plate glass were subjected to an acid pre-treatment (50% $H_2SO_{4(aq)}$) for 15 min, before being washed with distilled H_2O and then acetone. Both the cylinder and the plate glass were dried in an oven at 100 °C for 1 h. PBI S26 in DMAc (6.1 g total mass of solution, 5 wt% [PBI S26]) was prepared and poured into the template. The template was heated to 50 °C on a hot plate under a slow argon flow in an inert atmosphere bag for 4-5 h to produce a thin film. The cylinder was separated from the template by cutting around both the inside and outside of the cylinder with a scalpel. Once completed, the film was carefully peeled away by a small spatula, and placed inside a vacuum oven at 100 °C overnight. This film was roughly 40 µm in thickness. The film was then soaked in distilled H_2O for 2 h at 80 °C using a hot plate to remove LiCl, and dried in a vacuum oven for 3-5 h, at 100 °C. The membrane was eventually cut into squares of 9 cm^2 for doping with H_3PO_4 and MEA fabrication.

Other preparations included:

- Two PBI S26 solutions (12 g and 1.5 g solutions, 5 wt% PBI S26, each in DMAc) were poured into 14 cm and 5 cm diameter Pyrex petri dishes, respectively. They were then heated to 80 °C on a hot plate until a dry film appeared. Both dishes were heated in open atmosphere.
- A solution of PBI S26 (1.5 g total solution, 5 wt% in DMAc) was poured into a 5 cm Pyrex petri dish, and then covered with a large beaker. It was then heated to 80 °C on a hot plate until a dry film appeared.

- A 14 cm Pyrex petri dish was placed in a large acrylic box, covered only by paper towels at the top. A solution of PBI S26 (12 g total solution, 5 wt% in DMAc) was poured into the dish and heated on a hot plate to 80 °C until a dry film appeared.
- A solution of PBI S26 (12 g total solution, 5 wt% in DMAc) was poured into a 14 cm Pyrex petri dish and evaporated to dryness at room temperature in open air.
- A solution of PBI S26 (12 g total solution, 5 wt% in DMAc) was poured into a 14 cm glass petri dish and heated on a hot plate at 80 °C until a dry film appeared. The membrane was peeled off the petri dish and cut into small pieces measuring approximately 1 mm x 5 mm. Formic acid (11.4 g) was placed inside a 50 mL beaker, along with 600 mg of the small PBI S26 pieces and a magnetic stir bar. The mixture was magnetically stirred at room temperature for several minutes until dissolved. This made a solution of PBI S26 in formic acid at 5 wt% concentration. This solution was poured into a 14 cm Pyrex petri dish and left for 4 d at room temperature in open air. The result was a cracked membrane that is shown in Figure 3.18B.
- A square template, bottomed by plate glass (15 cm x 15 cm), and walled by plate glass microscope slides (75 mm long, 25 mm high, each), was fabricated (shown in Figure A5, appendix). The adhesive used to glue the template together was Silicone I (All Purpose) made by General Electric. A PBI S26 solution (4.5 g total solution, 5 wt% in DMAc) was poured into the template and heated to 100 °C using a hot plate for 1 h until a dry membrane was formed.

2.4.3 m-Phenylene polybenzimidazole from PBI Performance Products (PBI 0.8IV)

m-Phenylene polybenzimidazole from PBI Performance Products (PBI 0.8IV, powder, 2 g) was poured into a 250 mL round bottom flask along with 98 g of DMSO and a magnetic stir bar. A condenser was then attached to the flask. The flask was then heated to 180 °C for 27 h using a silicone oil bath. During this time, most of the PBI 0.8IV had dissolved. However, a white solid had also condensed on the condenser wall and was analyzed by ESI-MS and ^{1}H NMR spectroscopy to find out what it was. After the 27 h period, the remaining particulates were removed by filtration of the hot mixture through Celite® 545 and glass wool into a 250 mL beaker. The filtrate was a saturated 1.5 wt% solution of PBI 0.8IV in DMSO. This concentration of PBI 0.8IV in DMSO took into account the solid that did not dissolve into the DMSO. The mass of the white solid that was collected on the condenser was subtracted from the initial mass of starting material to calculate the [PBI 0.8IV] in DMSO after filtration. At room temperature, the filtered PBI 0.8IV solution retained a similar viscosity and concentration when compared to the same solution at 180 °C. This solution at room temperature was poured into a 14 cm Pyrex petri dish and evaporated to dryness at 80 °C using a hot plate. The resulting membrane was then placed in a vacuum oven at 120 °C overnight. When the membrane was taken out of the vacuum oven, the membrane was observed to be uneven and brittle. The thickness of this membrane was measured by caliper (Procise 210-2372) to be between 50-170 µm thick, depending on where the thickness was measured on the membrane. The following spectral data is for the white solid that was captured during the dissolution of PBI 0.8IV. ^{1}H NMR spectrum (ppm) (DMSO-d_6) δ 2.08 (m, J = 1.52 Hz), δ 2.10 (s), δ 2.33 (m), δ 2.37 (br, s), δ 2.42 (s), δ 2.54 (s), δ 2.67 (m, ^{2}J = 3.79 Hz, ^{3}J = 1.77 Hz), δ 2.71 (d, J = 1.77 Hz), δ 3.22 (s), δ 3.25 (s), δ 3.47 (br, m), δ 3.49 (br, m), δ 3.99 (br, m), δ 4.43 (s), δ 4.46 (s), δ 4.47 (s), 4.53 (d, J = 1.01 Hz), 4.56 (d,

J = 1.52 Hz), δ 4.57 (s), 4.59 (s), δ 4.64 (d, J = 2.02 Hz), δ 4.68 (d, J = 4.04 Hz), δ 4.70 (s), δ 4.78 (d, J = 1.26 Hz), δ 4.79 (dd, ^{2}J = 6.06 Hz, ^{3}J = 1.52 Hz), δ 4.80 (m, ^{2}J = 6.06 Hz), δ 4.87 (s), δ 4.88 (s), δ 4.89 (dd, ^{2}J = 1.77 Hz, ^{3}J = 1.01 Hz), δ 4.99 (dd, ^{2}J = 2.02 Hz, ^{3}J = 1.52 Hz), δ 5.09 (s), δ 5.10 (s), δ 5.12 (s), δ 8.13 (s), δ 8.30 (s), δ 9.11 (s), 9.34 (s), 9.57 (s). ^{13}C NMR spectrum (ppm) (DMSO-d_6) δ 81.9, δ 84.0, δ 84.9, δ 85.2, δ 85.3, δ 86.2, δ 87.2, δ 87.5, δ 87.6, δ 88.3, δ 88.6, δ 88.7, δ 89.0. ESI-MS (m/z) 151.025, 153.047, 153.546, 154.044, 154.543, 155.044, 156.989, 158.041, 159.040, 160.040, 161.040, 164.050, 169.110, 169.553, 171.106, 180.095, 188.084, 189.082, 195.572, 197.070, 203.044, 222.013, 242.284, 383.116, 404.041, 443.137, 563.179, 568.566, 569.569, 572.930, 575.413, 586.946, 593.190, 596.598, 597.600, 599.580, 607.391, 612.592, 622.613, 623.200, 627.611, 639.408, 647.459, 653.211, 663.453, 713.232, 747.505.

Another method of casting PBI 0.8IV involved pouring 0.1 g of PBI 0.8IV into a 20 mL glass vial, along with 9.9 g of DMSO and a magnetic stir bar. The mixture was heated at 180 °C using a silicone oil bath. Almost all of the PBI 0.8IV dissolved to create an approximate 1 wt% solution of PBI 0.8IV in DMSO. The hot mixture was filtered through Celite® 545 and glass wool to isolate the undissolved solids. The filtrate was collected directly into a Pyrex glass petri dish and left to evaporate to dryness at 80 °C on a hot plate for 5 h. The resulting membrane peeled off the glass petri dish with ease and the membrane was placed inside a vacuum oven at 120 °C for 16 h. The thickness of the membrane was measured by caliper (Procise 210-2372) to be uniform, measuring 25 µm.

2.4.4 Sulfonated m-phenylene polybenzimidazole (SS26)

A template consisting of a borosilicate plate glass bottom (15 cm x 15 cm) and a steel cylinder wall (12 cm diameter) was pre-treated according to the procedure outlined in 2.4.2. It is the same setup as seen in Figure A6 (appendix), except with a borosilicate glass bottom instead of a silicate glass bottom. Finely ground SS26 (0.45 g), 8.51 g of DMSO, and 24 mg of LiCl were poured into a 20 mL glass vial along with a magnetic stir bar. The mixture was magnetically stirred and heated to 160 °C by a silicone oil bath for 1 h. During this time the SS26 had dissolved into the DMSO to produce a 5 wt% SS26 solution in DMSO. The solution was then filtered hot through Celite® 545 and glass wool. The filtrate was directly poured into the template. This template was preheated to 70 °C on a hot plate, open to air. The casting solution of SS26 and DMSO was too viscous to form a uniform layer on the glass at first, but after 10 min, it had flattened out. After 1 h, cracks started to appear in the middle of the membrane. At this point, the casting process was terminated.

Another variation of this procedure was tried using a different solvent. SS26 polymer (1.5 g) and 28.5 g of 98% $H_2SO_{4(aq)}$ were poured into a 50 mL beaker along with a magnetic stir bar. The mixture was heated to 170 °C using a silicone oil bath and was magnetically stirred for several minutes to dissolve the SS26 polymer in H_2SO_4. The [SS26] was 5 wt% in $H_2SO_{4(aq)}$. The solution was then poured into the same template described in the previous paragraph, which was preheated to 170 °C using a hot plate. The solution filled template was left for 3 d at this temperature. A membrane had still not formed after 3 d so the temperature was increased to 220 °C and left for another 2 d. After the 2 d had passed, a precipitate had formed but it was still very wet. It appeared as if the polymer had precipitated as a powder, rather than formed a membrane. At this point, the casting process was terminated.

2.5 MEA fabrication

2.5.1 Ink deposition: PAMADP/PVP/Nafion®

The prepared inks of PAMADP and Pt/C (as described in chapter 2.3.3) and PVP and/or Nafion® and Pt/C (as described in sections 2.3.1-2) were individually poured into the reservoir of an Iwata Eclipse HP-CS airbrush just before the deposition of each ink. The airbrush was connected to a Praxair high purity argon gas tank. A piece of untreated carbon cloth was cut to roughly 2 cm x 2 cm and sandwiched in the centre of two plates of Plexiglas®. These plates were then clamped in place using two Bulldog® clips. Each plate of Plexiglas® had a square hole measuring 1 cm^2 in its centre, a bezel of 3 cm and a depth of 6 mm. The carbon cloth was placed such that both holes were directly in the centre of the cloth on either side. The ink was sprayed into one of these square holes with a back pressure of 30 PSI at a distance of 2 cm to create a catalyst coated gas diffusion layer (CCGDL). This assembly is shown in Figure 2.1, along with the airbrush in Figure 2.2. As the ink was applied, the airbrush was repeatedly pivoted from left to right to produce an even coverage. The catalyst loading of the CCGDL ranged mostly between 0.3-0.5 mg Pt/cm^2. The quality of the CCGDL was judged by how the spray flowed from the airbrush and how the catalyst bed looked under an optical light microscope.

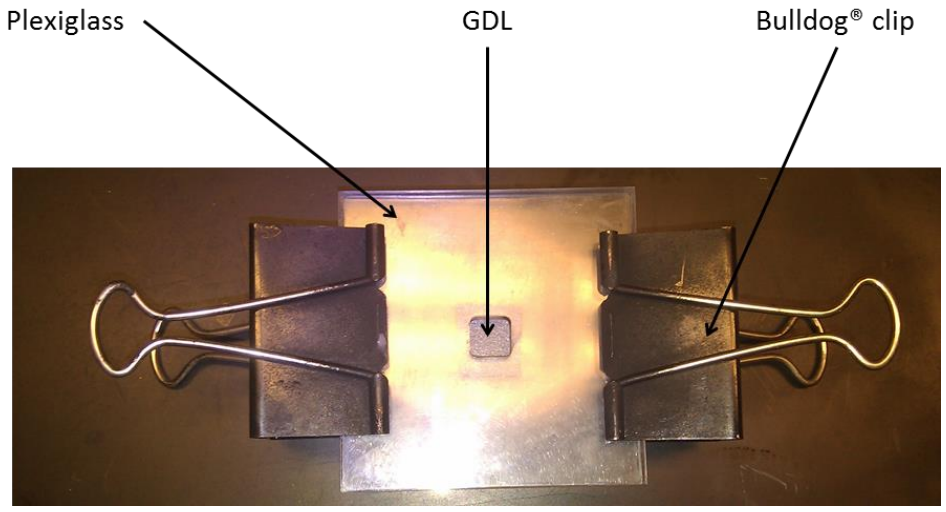

Figure 2.1: The assembly that was used to hold the GDL in place whilst spraying the PAMADP, PVP or Nafion®-based ink onto the GDL surface.

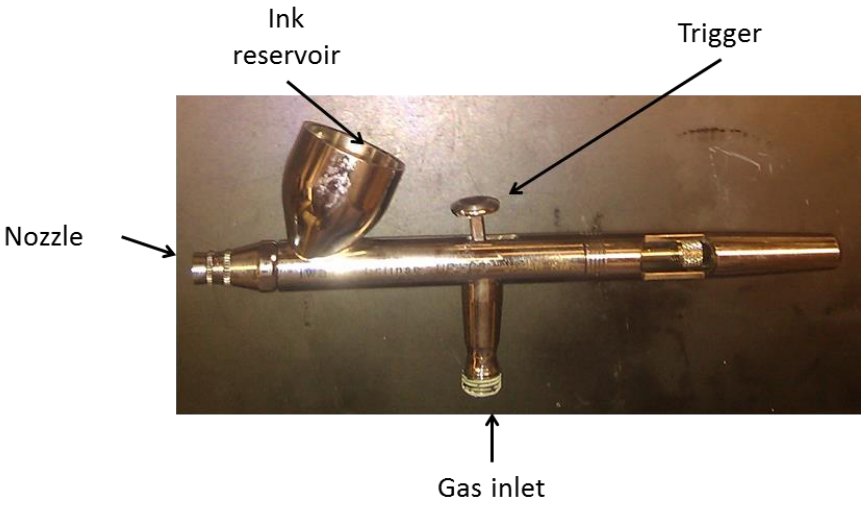

Figure 2.2: Iwata Eclipse HP-CS airbrush.

2.5.2 Ink deposition: PBI S26/DPS PBI

A large sheet of SpectraCarb 2050-A carbon paper was cut into many 3 cm x 3 cm squares. One of these squares was sandwiched at the centre of two steel plates. Both plates had a square hole measuring 5 cm^2 in the centre, a bezel of 2.54 cm and a depth of 3 mm. These plates were then clamped in place using two Bulldog® clips. The carbon paper was placed such that both holes of the plates were directly in the centre of the paper on either side. This assembly is shown in Figure 2.3.

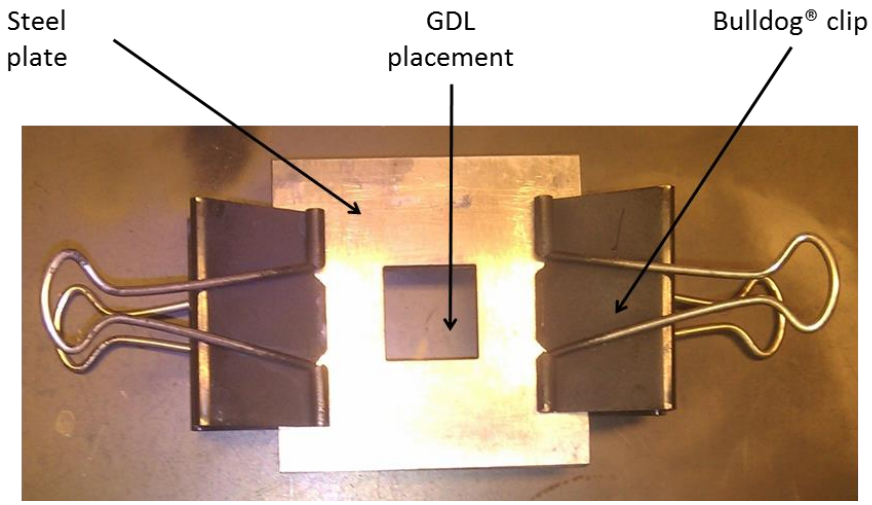

Figure 2.3: The assembly that was used to hold the GDL in place whilst spraying the PBI S26 or DPS PBI-based ink onto the GDL surface.

The prepared ink (chapter 2.3.4A for PBI S26-based inks and chapter 2.3.4C for DPS PBI-based inks) was poured into the reservoir of the airbrush and then sprayed onto the surface of the paper at a rate of 2 mL/min, with a back pressure of argon gas between 1-5 PSI. This ink was sprayed onto the

paper in a zigzag pattern. This was achieved by moving the airbrush from left to right in a downward direction whilst spraying the ink. Once the surface of the paper had been completely covered once with the ink, the steel plate and CCGDL assembly was rotated 90° and the spraying process was repeated to ensure even coverage of the ink on the surface of the paper. For PBI S26-based CCGDLs the assembly was rotated 3 times to cover all of the area on the surface of the paper. For DPS PBI-based inks, the assembly was not rotated at all as the idea of rotating the assembly had not yet come to mind. This is because the DPS PBI-based CCGDLs were made before the PBI S26-based CCGDLs. The DPS PBI and PBI S26-based CCGDLs were then taken out of the assembly and placed onto a hot plate at 50 °C to evaporate excess solvent. Once dry, the CCGDL was placed back inside the steel plate assembly to begin ink deposition again.

The process that encompasses the deposition of the ink to drying off the excess solvent was repeated many times until the catalyst loading (Pt or Pd) on the surface of the carbon paper was approximately between 0.4-0.5 mg (Pt/Pd)/cm^2. This loading was calculated by weighing the CCGDL on a mass balance (Mettler Toledo: New Classic MF ML204) after it had dried on the hot plate. However, as the CCGDL was still slightly wet with excess solvent, an approximation of the catalyst loading is all that can be determined at this point.

The CCGDLs were then placed inside a vacuum oven at 100 °C overnight. The CCGDLs were then soaked in deionized H_2O for 2 h at 80 °C on a hot plate to eliminate any free LiCl that was present within the CCGDLs. Then the CCGDLs were washed with a deionized H_2O wash bottle for several seconds and then placed inside the vacuum oven at 100 °C for 5 h. The dry CCGDLs were then weighed on a mass balance to accurately determine the catalyst loading. If any more catalyst was required to meet the desired catalyst loading of 0.4-0.5 mg (Pt/Pd)/cm^2, the ink deposition procedure was repeated.

2.5.3 Ink deposition: CDPS PBI

For CDPS PBI, the ink deposition was similar to the other PBI-based inks mentioned in the previous chapter. However, the ink (as prepared in chapter 2.3.4B) was applied to the CDPS PBI membrane rather than carbon paper. At first, a large sheet of CDPS PBI membrane was cut into 6 cm x 6 cm portions and one of them was placed inside the steel plate assembly as described in the first paragraph of chapter 2.5.2. The ink was deposited at a slightly lower flow rate than 2 mL/min at first to prevent the ink from gliding around the surface of the membrane. This gliding was caused by the argon gas flow from the airbrush interacting with the ink on the membrane surface. Once an initial layer of ink was deposited and dried on a hot plate at 50 °C, the flow rate of the ink could return to 2 mL/min in order to deposit the rest of the ink in the same fashion as described in chapter 2.5.2. The newly created catalyst coated membrane (CCM) was placed in a vacuum oven at 100 °C overnight to dry. The CCM was then soaked in deionized H_2O for 1 h at 80 °C to remove any free LiCl embedded in the catalyst bed, followed by treatment in the vacuum oven at 100 °C for 3 h. The dry CCM was subsequently weighed to determine the catalyst loading. If any more catalyst was required, the deposition procedure was repeated.

2.5.4 Acid doping of membranes

For all PBI membranes and PBI-based CCGDLs, except CDPS PBI, the doping procedure was as follows. After the procedure in chapter 2.5.2 was complete, a 12 M solution of $H_3PO_{4(aq)}$ was prepared by

diluting 85% $H_3PO_{4(aq)}$ with deionized H_2O. For each membrane or CCGDL that was to be doped with H_3PO_4, a 5 cm diameter glass petri dish was almost completely filled with 12 M $H_3PO_{4(aq)}$. Then each membrane or CCGDL was placed inside each petri dish filled with 12 M $H_3PO_{4(aq)}$ to soak for a period of 36-48 h at room temperature. The CCGDLs were then quickly rinsed with deionized H_2O for a few seconds using a wash bottle and then patted dry with a lint-free tissue. The naked PBI membranes were only patted dry with a lint-free tissue after they were taken out of the 12 M $H_3PO_{4(aq)}$ solution. Both the naked membranes and the CCGDLs were then placed inside a vacuum oven at 100 °C overnight to evaporate any excess H_2O. The doping levels of the membranes were calculated based on the mass difference between the non-doped membrane before exposure to 12 M H_3PO_4 and the doped membrane after exposure to 12 M H_3PO_4. The mass gain was assumed to be all pure H_3PO_4.

CDPS PBI CCMs were doped with 85% H_3PO_4 for 2 h at 70 °C using a silicone oil bath after the procedure in chapter 2.5.3 was completed. The doped CCMs were then patted dry with a lint-free tissue, and dried in a vacuum oven overnight at 100 °C.

2.5.5 Hot pressing of MEAs

For MEAs that were made using PBI S26 membranes, two H_3PO_4-doped CCGDLs were paired with a H_3PO_4-doped membrane. One CCGDL was assigned to be the anode and the other was assigned to be the cathode of the MEA. The CCGDLs were pre-cut to size (5 cm^2) so that no naked carbon paper was exposed on the same side as the catalyst bed. On a 30.25 sq. in. gold-plated copper plate (GPCP), the CCGDLs were placed underneath and above the membrane so that they vertically aligned with each other. The catalyst bed faced the membrane, whilst the naked carbon paper side of the CCGDL faced

outwards. Another GPCP of the same dimensions was carefully placed into position on top of the MEA and the other plate so that the plates vertically aligned. The MEA and GPCP assembly was then carried to a hydraulic press (Carver: Hydraulic Unit 3925) (CHU). This assembly was placed between the two platens of the CHU. Both platens had been preheated to either 130 °C or 150 °C via pencil rods inserted directly into each platen. The temperature for each platen was controlled by external temperature controllers (Barnant: Temperature Controller 689). In order to make the MEA, 2000-9000 lbs of pressure was then applied to the MEA/GPCP assembly for 2-30 min. Specific conditions for pressure, time and temperature per MEA trial are shown in Table 4.1. To retrieve the MEA from the CHU, the pressure was released and the MEA/GPCP assembly was removed to cool under a concrete brick to room temperature. The plates were then carefully separated, revealing the fused MEA. In many cases, a spatula was required in order to gently peel the MEA off the plate. The MEA was visually inspected for imperfections and irreparable damage.

For the CDPS PBI CCMs, a 0.07 mm reinforced Teflon® gasket with a 5 cm^2 square hole in the middle was placed on top of a flow field plate with the flow field facing the gasket. The gasket was placed such that the square hole uncovered the serpentine flow channels in the centre of the flow field plate. One 5 cm^2 square piece of SpectraCarb 2050-A carbon paper (GDL) was positioned directly in the hole left by the gasket. The CDPS PBI CCM was then placed directly on top of the GDL and the gasket such that the GDL was vertically aligned with the bottom facing electrode of the CCM. The next gasket and GDL of the same size and materials were placed on top of the opposing electrode of the CCM in the same manner as before. A second flow plate was then carefully placed on top of the gasket and GDL to complete the assembly. This assembly was inserted inside the CHU for 2 min at 2,000 lbs of pressure at a temperature of 130 °C.

2.6 Fuel cell setup

2.6.1 Fuel cell assembly

After the fusing of the MEA with a hydraulic press, the MEA was placed between two gaskets and two flow field plates. The gaskets were made from Teflon®, rubber or silicone. The gaskets were cut to fit around the two 5 cm^2 electrodes of each MEA, as well as cover the entire flow field plate surface, so that the gas or liquid fuel for the fuel cell could not cross over to the opposing flow field plate and therefore the opposing electrode. The flow field plates were made from a graphite/aromatic thermoplastic polyester composite material and contained two flow channels that ran parallel to each other from inlet to outlet.[39] In order to cover as much of the catalyst bed as possible, the pattern of the flow field was serpentine in nature; seen on the flow field plate shown in Figure 2.4. Once the MEA, gaskets and flow field plates had been assembled, a current collector and an endplate were added to each side of the MEA. The total assembly was screwed together with 8 screws, each one torqued to 55 inch pounds. Figure 2.4 shows the fuel cell assembly. The resistance of the fuel cell was measured using a milliohmmeter (Hioki: 3560AC) at room temperature. If the resistance of the fuel cell measured above 4 Ω, it was reassembled and then tested for gas leaks by checking for holes in the MEA or loose gaskets. N_2 at 1 barg (1 bar above atmospheric pressure) was applied to the anode side and a leak test was performed on the cathode side to see if the gas had crossed over. If it had, the cell was disassembled and checked for alignment issues or visible holes, reassembled and re-checked for gas leaks and resistance. Figure 2.5 shows how the MEA is placed in between the gaskets.

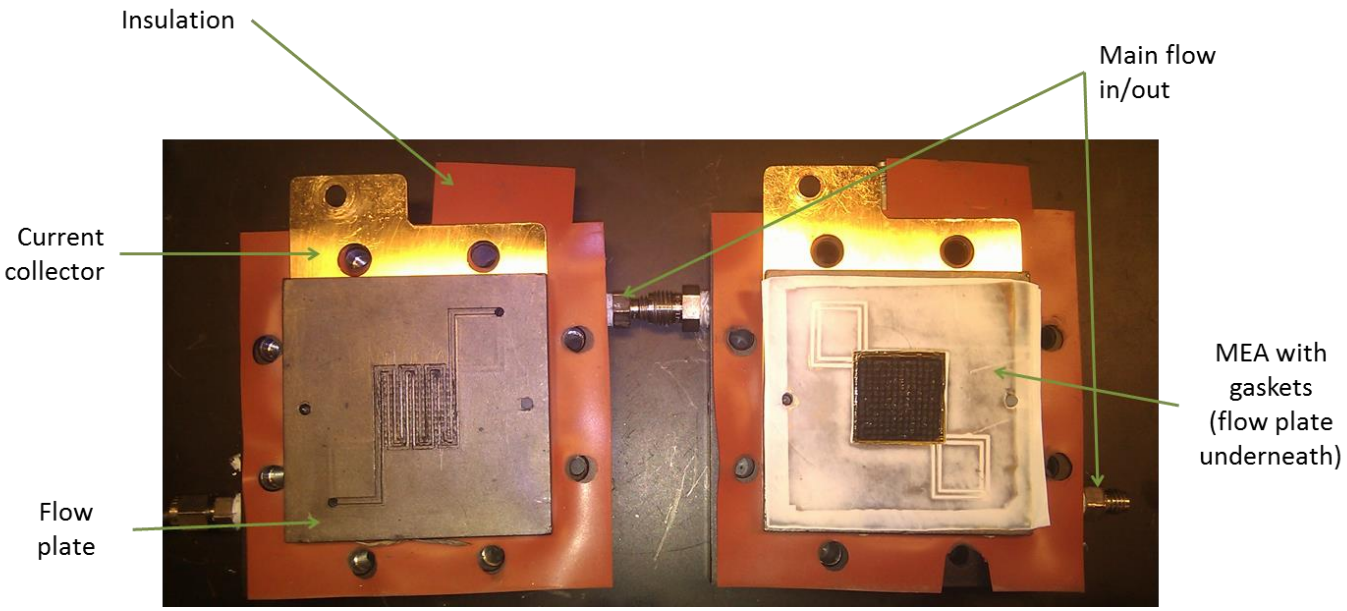

Figure 2.4: Fuel cell assembly for a PEMFC.

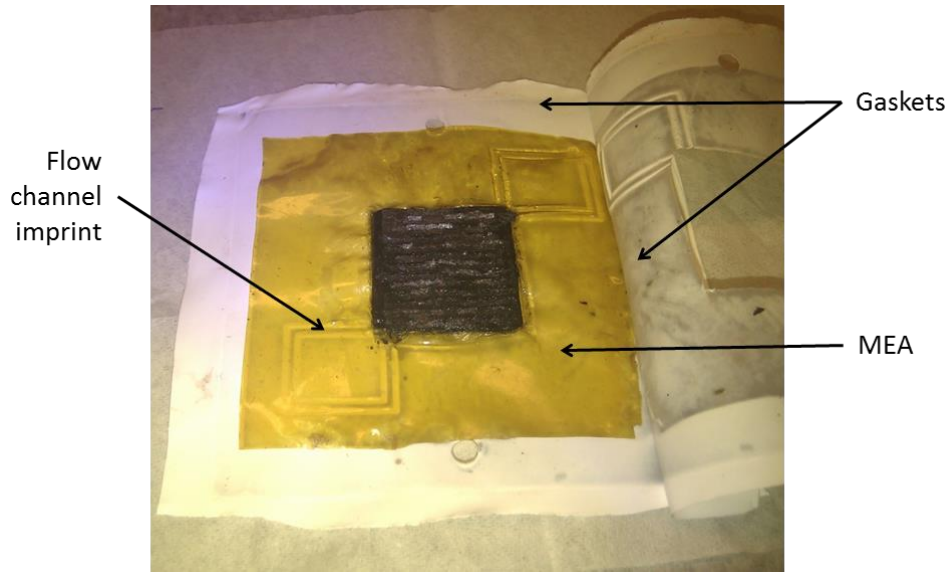

Figure 2.5: The placement of the MEA within the gaskets.

2.6.2 H_2/air fuel cell testing

After the fuel cell was assembled, it was then connected to a testing station. Two different test stations were used for this process, including the Hydrogenics G60 (using HyWare II software) and a custom setup containing an Autolab PGSTAT302 potentiostat and Autolab 4.9.007 software. The custom setup also comprised an Arbin Instruments BT-2000 battery test station, which used MITS Pro 3.0 (build 5.28) software to control gas flow. Two Barnant Company 689 temperature controllers were used in this custom setup to control the endplate temperatures of the fuel cell. Both setups shared the same basic connections to the fuel cell assembly. These included H_2 and air input/output gas lines and electrical load connectors as well as a thermocouple and a heating rod for each endplate.

The HyWare II software monitored gas flow, endplate and gas flow temperatures, and current/voltage relationships. The Hydrogenics G60 setup was galvanostatic in nature, and recorded all of the galvanostatic information in an editable spreadsheet format. The fuel cell was heated to 120-160 °C, and the gas flow was kept at 0.055 L/min for H_2 and 0.100 L/min for air.

For the custom setup, the temperature was also kept to the same range as the Hydrogenics setup but the flow rates were varied between 0.1-1000 mL/min to see if the gas flow rate changed the performance of the fuel cell. The Autolab software monitored just current/voltage relationships as the temperature was controlled via external temperature controllers and the gas flow was controlled by the battery test station. This custom setup was potentiostatic in nature, and all data from the Autolab software was exported to a spreadsheet format for analysis.

2.6.3 H_2/propiophenone fuel cell testing

Most tests were performed on the custom setup using the Autolab potentiostat and software. However, one test was performed with a modified Hydrogenics setup. Both setups were modified to account for the liquid state of propiophenone by exchanging the air gas line with a pump that ran propiophenone to the cathode using steel tubing. In the case of the Hydrogenics setup, this allowed for the transfer of propiophenone (200 g total) to and from a holding flask. This setup is shown in Figure 2.6.

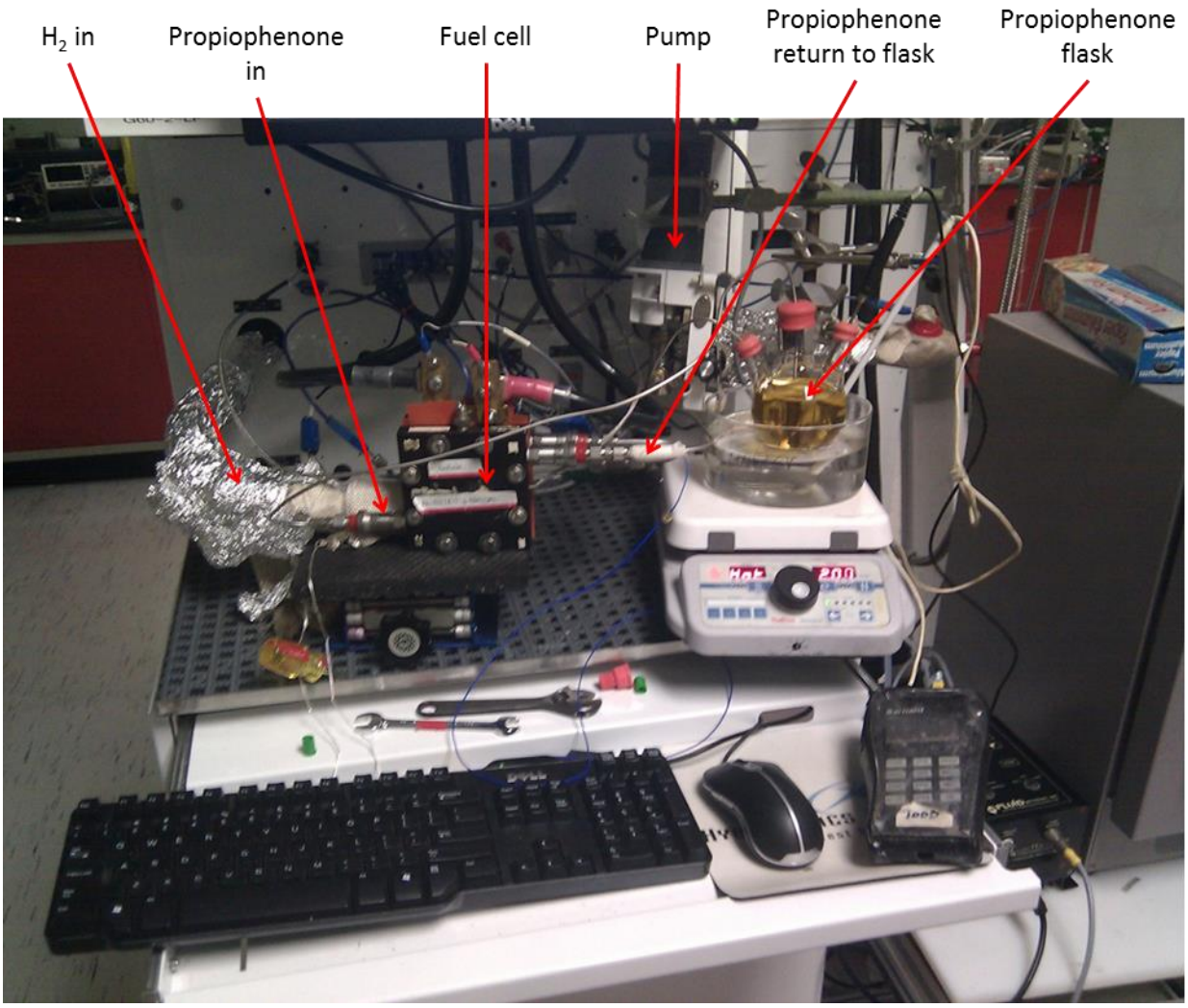

Figure 2.6: H_2/Propiophenone setup (Hydrogenics G60).

The custom setup using Autolab was changed to add a Waters 515 HPLC pump to transfer propiophenone to the fuel cell instead of using the battery test station to control air flow. Propiophenone was collected separately unlike the Hydrogenics setup, and analyzed by GC-FID using a Shimadsu GC-17A gas chromatograph for the presence of 1-phenyl-1-propanol. Arbin was still used to control H_2 flow to the fuel cell. The setup is shown in Figure 2.7.

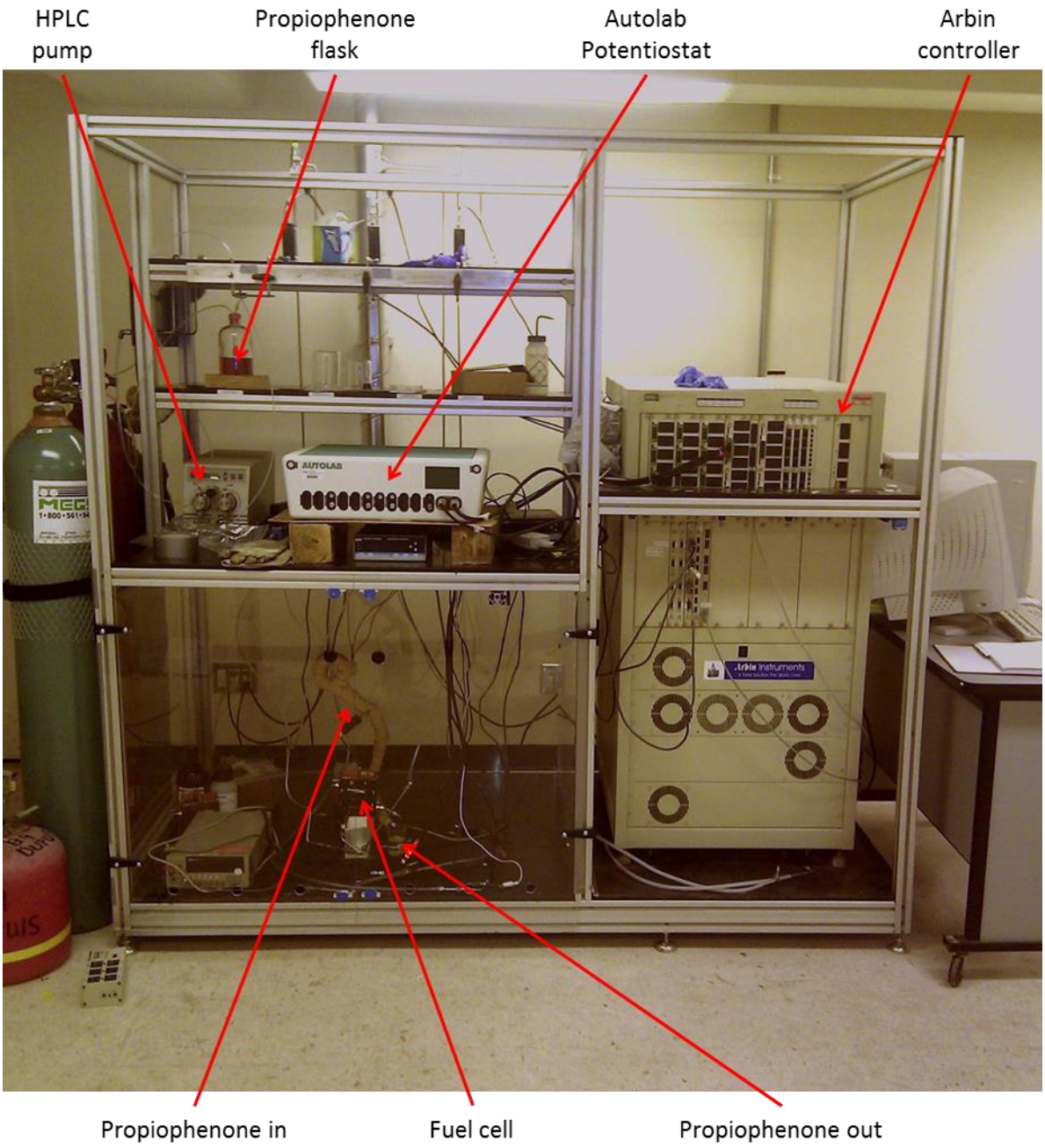

Figure 2.7: Custom setup for the H_2/propiophenone fuel cell.

Chapter 3 Results: Ionomer and Polymer Selection

3.1 Ionomer and membrane selection

Only certain kinds of polymers can be used in the MEA of the proposed TRFC. The conditions of the fuel cell will be highly acidic, and the polymers must not be soluble in or react with propiophenone and 1-phenyl-1-propanol. Also, the polymer must not react with the catalyst at each of the electrodes of the fuel cell. Acceptable functional groups within an ionomer/binding agent or membrane that would be used in the TRFC that is proposed are shown below.

- Alkane
- Imidazole
- Imine
- Ketone
- Nitrogen heterocycle
- Phenyl rings
- Sulfone
- Sulfonic acids
- Thiol

Other functional groups could be affected by hydrolysis, catalytic reduction at the cathode, or reactions with the ketone and alcohol groups of propiophenone and 1-phenyl-1-propanol. Therefore, a search of polymers was conducted to determine whether they were suitable for the proposed TRFC system. The chosen polymers were subjected to solubility tests in propiophenone and 1-phenyl-1-propanol. The polymers were also tested for solubility in the working fluid of the TRFC. The working fluid is defined as the mixture of propiophenone and 1-phenyl-1-propanol that will be

circulating throughout the TRFC. The equilibrium mixture of the working fluid in the dehydrogenation reactor is 46/54 w/w of 1-phenyl-1-propanol and propiophenone, respectively. At the cathode of the TRFC, the working fluid enters the flow field plate at the 46/54 w/w mixture that was created in the dehydrogenation reactor. However, as the fluid passes over the catalyst bed the propiophenone is reacted to 1-phenyl-1-propanol. When the working fluid has flowed past the catalyst bed the working fluid may have reached equilibrium. Whether the working fluid reaches equilibrium depends on the flow rate and the reaction rate of the working fluid. The equilibrium ratio of the working fluid at the cathode of the TRFC was calculated to be either 85/15 w/w at 140 °C or 96/4 w/w at 95 °C of 1-phenyl-1-propanol and propiophenone, respectively.[11] However, in the proposed TRFC system the ratio would be closer to 46/54 w/w, respectively at the entrance of the cathode flow field plate.[11] This is the ratio of the equilibrium mixture that is produced after the dehydrogenation reaction of the working fluid in the dehydrogenation reactor. This mixture will then enter the cathode of the fuel cell.[11] Exposing the polymers to the constituents of the working fluid and its equilibrium mixture at the cathode will determine if the polymers are stable under the proposed TRFC operating conditions. These polymers were also used in an ink preparation that would then be deposited onto a GDL or membrane to make a catalyst coated gas diffusion layer (CCGDL) or catalyst coated membrane (CCM), respectively. Once this was completed, the stability of the catalyst bed was tested in the working fluid. For CCGDLs, once the stability of the polymer was proven, casting of the polymer into a thin (30-50 μm), uniform membrane was attempted. Once the casting of this membrane was achieved, the membrane and the electrode backed by the GDL were unified to form a MEA. For CCMs, there was only one polymer tested (CDPS PBI) and that was already in membrane form as received from the manufacturer. The MEA could be made directly from the unification of the CCM and 2 GDLs.

The MEAs could then be tested inside a fuel cell to prove whether or not the TRFC system can be proven to work as a concept. The polymers that were researched are shown in Figure 3.1 below.

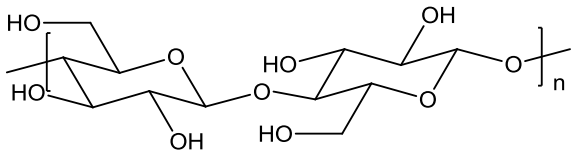

Cellulose

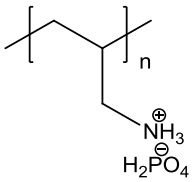

Poly(allylamine) dihydrogen phosphate

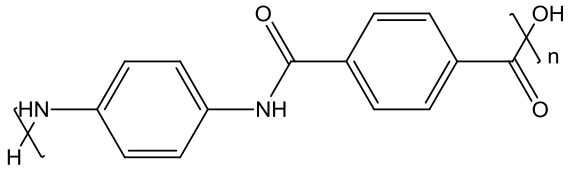

Kevlar®

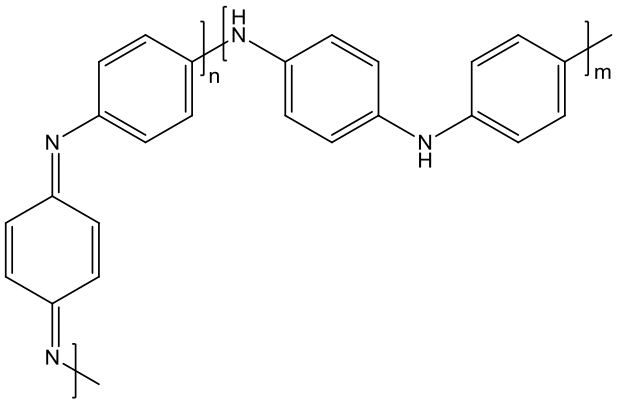

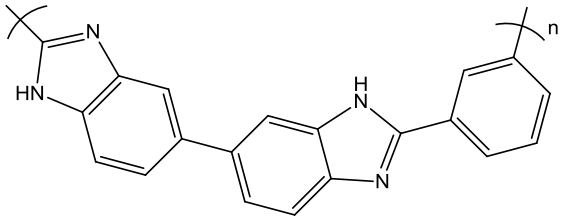

m-Phenylene polybenzimidazole

Polyaniline emeraldine base

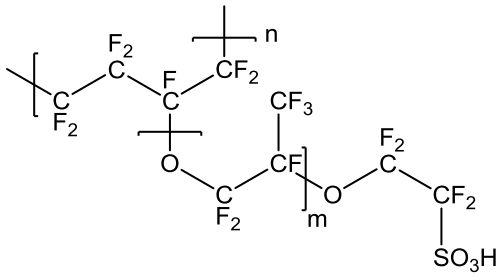

Nafion®

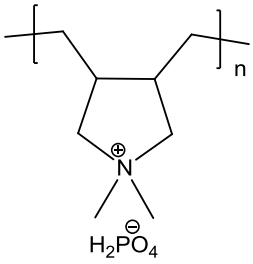

Poly(diallyldimethylammonium) dihydrogen phosphate

Figure 3.1: Possible polymer candidates for this TRFC system.

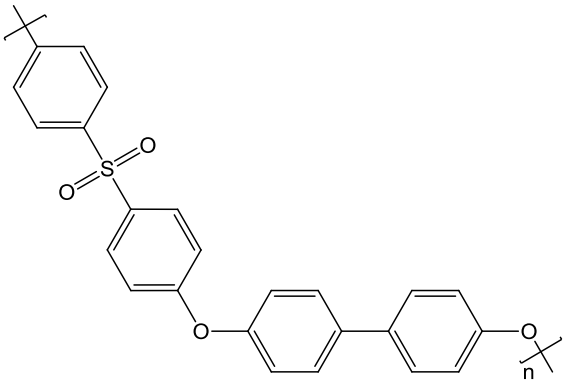

Polyphenylsulfone

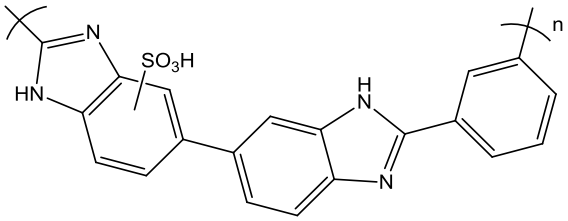

Sulfonated m-phenylene polybenzimidazole

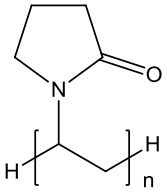

Polyvinylpyrrolidone

Figure 3.1 continued: Possible polymer candidates for this TRFC system.

Nafion® was chosen due to the fact that it has an extensive history in PEMFC.[6,14,17,19,20,38] Nafion® also contained no functional groups that would appear to pose a problem for the proposed TRFC system. Many Nafion®-based electrodes, membranes and standard solutions for ink preparation are available commercially. For these reasons, Nafion® was the ideal candidate to start with for use as a membrane and ionomer in the proposed TRFC system.

Cellulose was evaluated because it is an important feedstock from biowaste. As cellulose is not inherently an ionomer, an ionomeric material would have to be mixed or doped into the cellulose

polymer matrix. This material could be H_3PO_4. However, H_3PO_4 dissolves cellulose at elevated temperatures (> 42 °C when using anhydrous H_3PO_4) which would be of little use as a membrane or ionomer.[42] Cellulose is also degraded in pure H_2SO_4, which also behaves as an ionomer.[43]

Kevlar® was researched due to its inherent strength. The reasoning was that a strong polymer matrix is needed to withstand both the working fluid and the high acidity environment. Kevlar® does have amide groups, which would normally hydrolyze when in contact with a strong acid. However, Kevlar® has strong hydrogen bonding between its polymeric chains which prevents the acid from hydrolyzing the amide groups. Imbibing an inorganic acid into a Kevlar® membrane would facilitate H^+ transfer.

m-Phenylene polybenzimidazole and other PBI-based derivatives also have a PEMFC background like Nafion®.[17,33,34,44,45] PBI is normally used in high temperature PEMFCs (HTPEMFC).[17] Running the fuel cell at a higher temperature increases the electrochemical kinetics of the fuel cell reactants, simplifies water management, and improves CO tolerance for a H_2/O_2 fuel cell.[17,33] The ionic conductivity of H_3PO_4-doped PBI can be similar to Nafion® at its operating temperature.[33] However, conductivity varies considerably with doping level such that the conductivity ratio between PBI and Nafion® can reach at least 4 orders of magnitude.[33] Whilst the power output of a H_2/O_2 fed PEMFC using PBI is lower than a Nafion®-based PEMFC, the performance of the PBI-based PEMFC is remarkable when cell temperature is taken into account.[33] The non-sulfonated derivatives of PBI require doping with strong acids to facilitate H^+ conductivity,[17] as opposed to sulfonated PBI, which needs H_2O to facilitate H^+ transfer.[33,45] Both sulfonated and non-sulfonated PBI were studied for use in the proposed TRFC system.

Poly(allylamine) dihydrogen phosphate has been investigated for its use as part of a polymer electrolyte in H^+ conducting films.[46] However, it has not been investigated for its use as a PEM or ionomer in a fuel cell on its own. The amino groups on poly(allylamine) provide hydrogen bonding to

H_3PO_4,[46] which provides an enclosed environment for the H_3PO_4 to engage in H^+ exchange with itself and the polymer.

Polyaniline has previously been used with Nafion® in the construction of a PEMFC electrode.[47] Polyaniline was used because it could fill the spaces between the Nafion® and the carbon-supported catalyst to enhance catalytic activity by including previously isolated catalyst agglomerations due to its electrical conductivity.[47] However, it was ruled out as a possible candidate when it was discovered that polyaniline dissolved readily in propiophenone.

Poly(diallyldimethylammonium) dihydrogen phosphate has been previously explored as a possible membrane candidate for use inside a PEMFC and other electrochemical devices.[48,49] The H^+ conductivity reaches 10^{-2} S/cm with 3 eq of H_3PO_4 per repeating unit of PAMADP at 100 °C.[48] This conductivity is slightly below Nafion® at slightly lower temperatures.[33,48] The polymer blend with excess H_3PO_4 also showed thermal stability up to 150 °C, with minimal mass loss between 150 °C and 200 °C.[48] Therefore, this polymer blend showed promise for use in the proposed TRFC system.

Sulfonated and phosphonated polyphenylsulfones have been previously reported as membranes in PEMFCs.[50] However, as the main focus of this research is to use anhydrous conditions for the PEMFC, acid groups were not directly grafted onto PPS in this work. For the purpose of this research, PPS was used with the intention of creating a blend with H_3PO_4. The H_3PO_4 would facilitate H^+ transfer within the polymer blend. Nonetheless, it was ruled out as a possible candidate when it was discovered that it dissolved readily in propiophenone.

Polyvinylpyrrolidone (PVP) has been used before in a PEM as a part of a polymeric blend.[51,52] PVP is also reported in this capacity as a blend with silica and H_3PO_4.[53] However, a membrane made of just PVP and H_3PO_4 is not cited in the literature. The rationale behind using this polymer was the same as for PPS.

3.2 Nafion®

3.2.1 Ink preparation and deposition

Nafion® has been used before as an ionomer in the catalyst bed of a MEA.[54] Nafion® based ink mixtures have been made from a combination of Pt/C, isopropanol and Nafion® and were deposited onto either a gas diffusion layer or a Nafion® membrane.[54,55] The ink mixtures that were applied to either a gas diffusion layer or a membrane were deposited through the use of a spray gun or an inkjet printer, respectively.[54,55]

For my experiments, the Nafion® polymer that was used to create catalyst inks was received as a solution in aliphatic alcohols (the exact alcohols are unknown). Nafion® was precipitated out of this solution and then re-dissolved into a more volatile solvent to aid in faster evaporation when depositing the ink onto a GDL. The solvents chosen are shown in Table 3.1.

Table: 3.1: Solubility of a Nafion® 117 precipitated film in various solvents as a 5 wt% solution.

Solvent	Dissolved
Acetone	Yes*
Acetonitrile	Partial
Chloroform	No
Dichloromethane	Partial
Diethyl ether	No
Ethanol	Yes*
Ethyl acetate	No
Methanol	Yes*
Tetrahydrofuran	No
Toluene	Partial

*Dissolution took between 20-60 min using a sonicator bath (Fisher Scientific: FS30) at 100 W at room temperature.

A 5 wt% solution of Nafion® 117 was created in a selection of solvents and Pt/C (10 wt% Pt loading on carbon) was added to the solution to form an ink. Table 3.2 shows the different Nafion®-based ink application trials deposited onto a GDL. The GDL is made from either carbon paper or carbon cloth. Both of them are carbon made from carbon fibre but carbon cloth is a woven fabric whereas carbon paper is not.[23] To determine whether or not the airbrush could spray the ink without clogging or sputtering, the Pt/C concentration was varied within the ink. The best concentration of Pt/C in the ink was determined to be 10 wt% RTMI as the other mixtures (15 wt% and 20 wt% Pt/C RTMI) were too viscous to be sprayed by the airbrush. Therefore, Table 3.2 shows only mixtures that contain 10 wt% Pt/C RTMI.

Table 3.2: Pt loadings and airbrush conditions for Nafion®-based CCGDLs and catalyst inks, respectively. Also includes the mass of the CCGDL before and after exposure to 1-phenyl-1-propanol.

Trial	Ink Solvent	Back Pressure (PSI)	GDL	Pt/Loading (mg/cm^2)	Mass of CCGDL	
					Before Exposure* (mg)	After Exposure[a] (mg)
A	Acetone	5	Carbon paper	0.7	35.6	36.9
B	Acetone	10	Carbon paper	N/A	N/A	N/A
C	Aliphatic Alcohols	30	Carbon paper	0.8	44.3	45.0
D	Aliphatic Alcohols	30	Carbon cloth	0.4	32.0	32.3
E	Ethanol	5-10	Carbon paper	N/A	N/A	N/A
F	Methanol	20	Carbon paper	2.5	39.5	-[b]
G	Methanol	10	Carbon paper	0.6	29.0	29.1
H	Methanol	10	Carbon cloth	0.4	24.6	25.1

[a] Before and after exposure to 1-phenyl-1-propanol at 130 °C for 1 h. [b] See discussion in the text.

These ink deposition trials laid the framework for all further ink applications. As this was the first ink deposition trial, sufficient focus was placed on both optimizing the flow of the ink through the airbrush and learning how the airbrush behaves when spraying different mixtures. The acetone-based ink flowed easier through the airbrush than the others and was easier to remove from the airbrush interior when the spraying was complete. However, the back pressure had to be lowered from 10 PSI (**B**) to 5 PSI (**A**), as 10 PSI was enough to rip the catalyst bed off the surface of the GDL.

When Pt/C was mixed with the Nafion® in aliphatic alcohols solution, it was more difficult to spray out of the airbrush than the inks containing just methanol and acetone as the solvent. The flow of the ink was insufficient with a back pressure of 15 PSI. Therefore, increasing the back pressure to 30 PSI

was necessary to get the ink to flow at a steady rate. This suggests that the viscosity of the ink was either too high or that the aerosol droplets were too big to pass through the nozzle without the application of extra pressure.

The ethanol trial (**E**) proved to be insufficient as well. A back pressure of 5 PSI was too weak to spray the ink at a constant rate, so the trigger of the airbrush had to be pulled in and out in order to move the ink through the nozzle. This created large amounts of ink to be splattered across the GDL each time the trigger was pulled back and then pushed forward. It appeared as though the catalyst particles contained in the ink were too large to pass through the nozzle and as a result, the trial was discontinued.

The methanol trials (**F**, **G**, and **H**) were relatively successful. However, a back pressure of 20 PSI for trial **F** caused the ink to deposit too fast onto the GDL. A fast flow makes controlling Pt loading on the GDL especially difficult. Once the back pressure was reduced to 10 PSI (**G**, **H**), the ink began to flow nicely. The switch to carbon cloth made it easier to spray the ink onto the surface of the GDL as the solvent did not rest on the surface and hinder the deposition process of the polymer/catalyst matrix. The solvent percolated through the cloth, allowing more deposition to occur without having to dry the CCGDL as often. With volatile solvents like MeOH, drying the CCGDL was achieved by blowing argon through the airbrush directly onto the CCGDL.

3.2.2 Compatibility with the working fluid

Nafion® 117 membrane from the Fuel Cell Store was initially tested in a 96/4 w/w mixture of 1-phenyl-1-propanol and propiophenone, respectively at 95 °C for 20 h. Nafion® PEMs cannot operate beyond this temperature as liquid H_2O is required to effectively facilitate H^+ transfer within the

membrane. At 95 °C, the equilibrium of the working fluid at the cathode is 96 wt% 1-phenyl-1-propanol and 4 wt% propiophenone.[11] Another test was conducted at 140 °C, where the equilibrium at the cathode would be 85 wt% 1-phenyl-1-propanol and 15 wt% propiophenone.[11] The results are shown in Table 3.3.

Table 3.3: Nafion® exposure to the working fluid at fuel cell operating conditions.

Trial	Temperature (°C)	Ratio of 1-Phenyl-1-Propanol to Propiophenone (w/w)	Exposure (h)
A	95	96/4	20
B	95	96/4	31
C	140	85/15	20

Membranes from Trials **A** and **C** turned white after exposure to the working fluid. For trial **B**, the membrane also turned white, but parts of the membrane had begun to separate into what appeared to be a white fluid. There was also a fine suspension of polymer within the working fluid, indicating that it permeated the membrane and had separated the polymeric chains so they could float freely in the solvent. Figure 3.2 shows the mixture of **B** and the membrane that was taken out of the mixture after exposure.

A)  B) 

Figure 3.2: A) Nafion® membrane that partially disintegrated inside a mixture of 96 wt% 1-phenyl-1-propanol and 4 wt% propiophenone (working fluid) after the mixture was heated and magnetically stirred at 95 °C for 31 h (trial **B** from Table 3.3). B) The corresponding Nafion® membrane to the mixture shown in Figure 3.2A. The Nafion® membrane was transparent before it was exposed to the mixture.

The mixture of trial **B** was filtered through Celite® 545 and glass wool to capture the suspended polymer. The filtrate was colourless, with a small amount another colourless liquid present in a separate phase at the bottom of the vial. This liquid was dissolved in D_2O and a ^1H NMR spectrum was collected. Figure A1 (appendix) shows the ^1H NMR spectrum. A very strong singlet peak was found at 4.7 ppm, suggesting that the small phase at the bottom of the vial was H_2O. The presence of liquid H_2O would also indicate that the working fluid dehydrated Nafion®.

The Celite® 545 and glass wool were isolated and mixed with 2 mL of deuterated MeOH in a 20 mL glass vial. This mixture was boiled for 1 min and manually agitated before filtering through a

disposable plastic chromatography column containing a bed of dry Celite® 545 at the bottom of the column. The filtrate was still cloudy with white particulates, so this mixture was filtered through a Chromspec 0.45 µm NYL micropore filter. The filtrate from the Chromspec filter was homogeneous, so a ^{19}F NMR spectrum was collected from this sample to prove whether Nafion® was present or had decomposed. In deuterated MeOH, the ^{19}F NMR spectrum did not register any fluorinated compounds, even after 100 scans. This may be due to a lack of solubility of the commercial Nafion® membrane over the precipitated film from the Nafion® in aliphatic alcohols solution. Therefore, it could not be proven that Nafion® had dissolved in the working fluid.

To illustrate the solubility of Nafion® in the working fluids, a Kamlet-Taft plot containing the solvatochromic parameters of various solvents was created (Figure 3.3). Included in the plot were some solvents that can dissolve Nafion® (blue circles) and some that cannot dissolve Nafion® (red circles). The green circles represent solvents that would have similar solvatochromic parameters to the working fluids of 1-phenyl-1-propanol and propiophenone. The diameter of the circles represents the value of π^* (measure of the solvent's ability to stabilize a charge or dipole), where a large circle denotes a more positive π^* value than a smaller circle. According to Figure 3.3, solvents that can dissolve Nafion® have either significant α (H^+ donating ability) or β (H^+ accepting ability) values or include both. Solvents that cannot dissolve Nafion® have either insignificant α or β values or both. The solvents that are close analogues to 1-phenyl-1-propanol are in between the non-soluble and the soluble solvents. This suggests that the partial solubility of Nafion® in the working fluid (96 wt% 1-phenyl-1-propanol) as shown in Figure 3.2A is consistent with the results of the Kamlet-Taft plot shown in Figure 3.3. Also, acetophenone (similar to propiophenone) is in the same domain as the solvents that cannot dissolve Nafion®. This suggests that propiophenone would not be able to dissolve Nafion® membrane. Figure 3.3 also suggests that water and chloroform are not able to solubilize Nafion® because they both have poor

H^+ accepting ability (small β). This is important for Nafion® solvation because these solvents cannot effectively solvate the sulfonic acid group on the pendant chain of Nafion®.

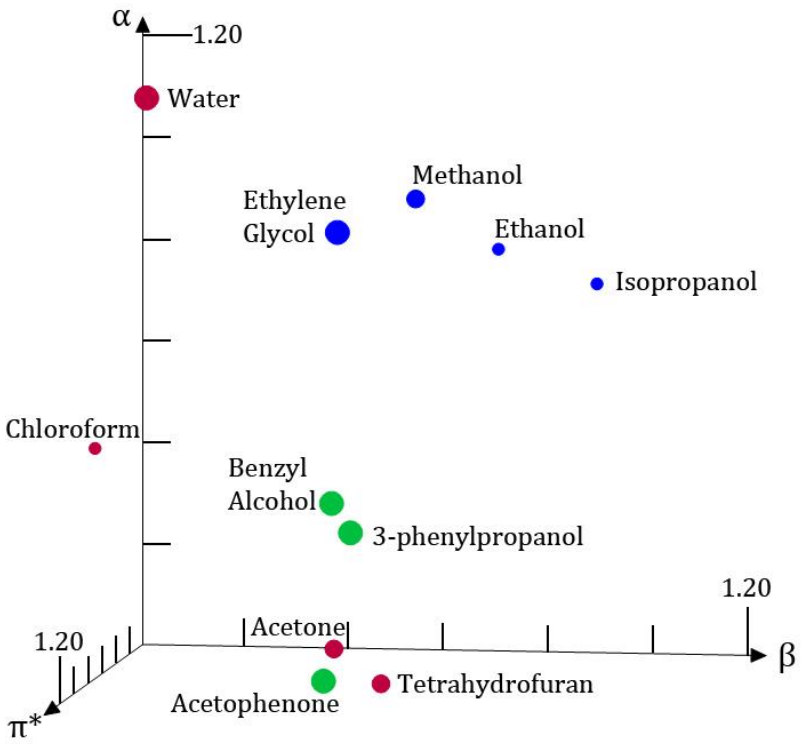

Figure 3.3: Nafion® solubility in various solvents by Kamlet-Taft parameters. Larger circles represent more positive π^* values. Nafion® is soluble in the blue solvents and not soluble in the red solvents. The green solvents represent the solvent analogues to 1-phenyl-1-propanol and propiophenone. Data for red and blue solvents was taken from Kamlet et al.[57] Data for the solvents that are represented by the green circles was taken from Hellal et al.[58]

CCGDLs from trials **A**, **C**-**D,** and **F-H** from Table 3.2 were soaked in 1-phenyl-1-propanol for 1 h at 130 °C. The CCGDLs were then dried in a vacuum oven overnight at 100 °C. All tested CCGDLs remained

close their original masses after exposure, except for **F**. Trials **A**, **C**-**D**, and **G**-**H** gained up to 1.3 mg after exposure, indicating that there was excess solvent present. The loss of mass for **F** is because the catalyst was easily removed from the surface of the CCGDL. Much of the lost catalyst came off when the CCGDL was accidently dropped onto the table. The ease of catalyst loss from **F** suggests that Nafion® was not uniformly present in the catalyst bed. This may have been caused by the increase in flow rate caused by the larger back pressure compared to **G** and **H**. Therefore, as the catalyst should not have separated in large quantities from the CCGDL when it was dropped, the experiment was not repeated.

As the concentrations of Nafion® and Pt/C in the inks were 5 wt% and 10 wt%, respectively, that would mean the ratio of these two compounds was 1:2 (Nafion®:Pt/C) by mass on the CCGDL. This assumes that the deposition of the ink is random on the CCGDL. Assuming this ratio is true, 2.5 mg/cm^2 of Nafion® would be present in the CCGDL if the Pt/C loading in the CCGDL equaled 5.0 mg/cm^2.

All of the CCGDLs lost a few granules of catalyst after exposure to 1-phenyl-1-propanol as well. This would indicate a loss of adhesion of the catalyst to the GDL, and therefore some loss of Nafion® to 1-phenyl-1-propanol. To add more evidence that some of the polymer had either been liberated or dissolved into the working fluid, the catalyst was more easily removed after exposure to 1-phenyl-1-propanol than before. Figure A2 (appendix) shows how easily the catalyst is removed after exposure to 1-phenyl-1-propanol. Unfortunately, even if all of the available Nafion® had dissolved into 1-phenyl-1-propanol, it would be difficult to use ^{19}F NMR spectroscopy to effectively analyze the sample.

As Nafion®-based CCGDLs and Nafion® membranes show excessive damage after exposure to the working fluid, the conclusion is that Nafion® is not compatible with the proposed TRFC system.

3.3 Polyvinylpyrrolidone and Nafion® blend

3.3.1 Solubility testing

A 1:1 w/w mixture of Nafion®/PVP was attempted to stabilize the Nafion® in the CCGDL. With the addition of a PVP to the mixture, a new solubility test was required to see which solvents could dissolve PVP and Nafion® together. Table 3.4 shows which solvents were tried, along with two different PVP variants.

Table 3.4: PVP8 and PVP40 solubility table.

PVP Variant	Weight Percent	Solvent	Dissolved
PVP8	5	Methanol	Yes
PVP8	5	Acetone	Yes
PVP40	5	Methanol	Yes
PVP40	5	Acetone	No

Polyvinylpyrrolidone (MW 8,000) (PVP8) all dissolved at 5 wt% in both acetone and methanol, whereas polyvinylpyrrolidone (MW 40,000) (PVP40) could only completely dissolve in methanol at 5 wt%. In acetone, PVP40 created a murky suspension. As both PVP8 and PVP40 both dissolved in

MeOH, ink solutions for both were made using MeOH and Nafion®. The concentrations of PVP8/40 and Nafion® were each selected to be 2.5 wt% in the MeOH solution.

3.3.2 Ink preparation and deposition

The PVP8/Nafion® and PVP40/ Nafion® blends were prepared as inks by adding Pt/C (10 wt% Pt loading on carbon) at 10 wt%, RTMI. Table 3.5 shows the results of each preparation. Neither ink preparation dried as quickly as the pure Nafion® inks, which indicated that the hydrogen bonding of PVP to the solvent is greater than that of Nafion®. A slower drying time of the CCGDL may negatively affect its performance in a fuel cell because larger polymer regions can form in the CCGDL and these large regions could excessively cover the catalyst and reduce the amount of three phase boundaries available in the catalyst bed.[21] Of more importance is the viscosity of the ink. The ink must be viscous enough to hold the catalyst particles in a suspension, but low enough that the ink can be sprayed onto the GDL.[59]

Table 3.5: PVP/Nafion® CCGDL Pt loadings on carbon cloth with a back pressure of 10 PSI.

Trial	PVP Variant	Pt/Loading (mg/cm^2)
A	PVP8	0.5
B	PVP40	0.4

3.3.3 Compatibility with the working fluids

The CCGDL containing the PVP8/Nafion® blend was soaked in propiophenone for 24 h at 140 °C. The result is shown in Figure 3.4. The catalyst abraded with considerable ease, which indicates that propiophenone dissolves the polymer. It was shown at this time by a colleague that propiophenone dissolves PVP8/40 on its own. PVP40 was also soluble in 1-phenyl-1-propanol above 60 °C. As it is not compatible with the working fluids, PVP was ruled out as a potential polymer for use in the proposed TRFC system.

Figure 3.4: The PVP8/Nafion® CCGDL after exposure to propiophenone for 24 h at 140 °C.

3.4 Kevlar®

3.4.1 Solubility testing

The solubility of Kevlar® was tested in many solvents as shown in Table 3.6. Many of the mixtures listed in Table 3.6 turned pale yellow, even though the presence of Kevlar® could not be detected by ^{1}H NMR spectroscopy (trials **B**, **C**, **D**, **E**, **K**, **I**). The same can be said for trial **A**, but the liquid turned red instead of yellow. However, in trial **F**, the solvent could not dissolve Kevlar® enough to change the colour of the mixture. Butadiene sulfone was chosen as a solvent because it can decompose into gaseous products when heated.[60] Scheme 3.1 shows this reaction.

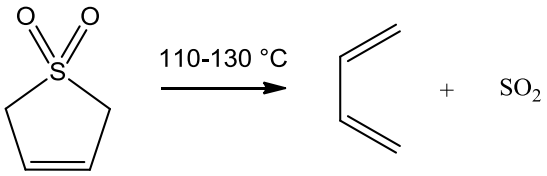

Scheme 3.1: The decomposition of liquid butadiene sulfone into gaseous butadiene and sulfur dioxide.

Table 3.6: Attempts at dissolving Kevlar® into selected solvents.

Trial	Wt% Kevlar®	Solvent	Temperature (°C)	Time (h)	Sonication (min)	Solubility (mg/mL)
A	0.10	NMP	175	24	N/A	Negligible
B	0.50	NMP + $CaCl_2$*	175	24	10	Negligible
C	0.50	DMF	150	24	N/A	Negligible
D	0.50	HMPA	200	2	N/A	Negligible
E	0.50	HMPA + $CaCl_2$*	200	2	N/A	Negligible
F	0.50	Aqua Regia + PPA (1:4 v/v)	175	24	N/A	Negligible
G	0.50	H_2SO_4	25	2	N/A	Decomposed
H	0.14	PPA + DMSO (1:1 w/w)	150	24	N/A	Decomposed
I	0.14	PPA	160	2	N/A	Negligible
J	0.10	Butadiene sulfone	95	1	N/A	N/A
K	0.10	Butadiene sulfone + TBAF (9:1 w/w)	80	<1	0.5	Negligible
L	0.47	DMSO + TBAF (9:1 w/w)	25	24	20	2.5

*$CaCl_2$ concentration was ~0.1 wt%. Polyphosphoric acid (PPA) is 115% polyphosphoric acid.

As butadiene sulfone decomposes between 110-130 °C to gaseous products, this would be helpful for making CCGDLs and membranes. Unfortunately, butadiene sulfone is a solid until 65 °C. Therefore, ink deposition would be more difficult as the ink must be kept as a liquid at all times, even when it is an aerosol during flight. However, this was solved by the addition of tetrabutylammonium fluoride (TBAF) (10 wt% in butadiene sulfone), which ensured that the mixture remained as a liquid even at room temperature. However, it was unable to dissolve the polymer in a sufficient wt%.

A mixture of DMSO and TBAF (10 wt% in DMSO) was also tried with Kevlar®. There is evidence in the literature that F^- does not harm Pt/C,[61] which should render TBAF harmless to Pt/C under operating

conditions in a fuel cell. This mixture was successful because it managed to dissolve the polymer to a limit of 0.26 wt%, which was far greater than all of the other mixtures. The mixture was at first a yellow colour but as the mixture got more concentrated with sonication, it became a deep orange. After approximately 1 year, the mixture was re-examined by chance. It had become unstable and had phase-separated into a gel and excess solvent. There is precedent for this behaviour, but with cellulose rather than Kevlar®.[62] Cellulose was reported to produce a gel between 0.75 and 1.0 wt%,[62] which is 3-4 times the concentration of the Kevlar® solution.[62] They did not, however, evaporate the gel to produce a membrane.[62]

Some of the Kevlar®-based gel was removed from the solution and placed onto a microscope slide, where the solvent was evaporated at 75 °C using a hot plate. It was then dried in a vacuum oven at 110 °C overnight. Figure 3.5 shows the surface of the Kevlar®-based dried gel. Figure 3.5 shows that a membrane can be made from evaporating excess solvent from a gel containing Kevlar®.

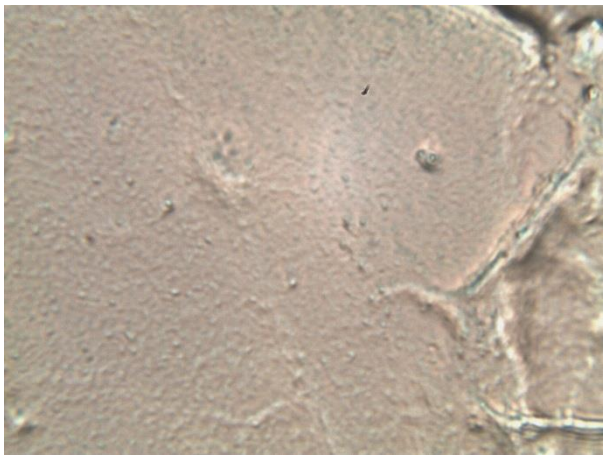

Figure 3.5: The surface of the Kevlar®-DMSO/TBAF dried gel (membrane) at 100x magnification.

The Kevlar® in trial **G** appeared to decompose in H_2SO_4 to form a dark brown viscous liquid at room temperature. There is precedent in the literature for both the dissolution and partial degradation via amide linkage hydrolysis of Kevlar® in H_2SO_4.[63] However, there is also precedent that H_2SO_4 should dissolve Kevlar® without any decomposition problems at 70 °C in a ratio of 10:1, respectively.[64] Unfortunately, the precipitated product is fibrous in nature.[64] Therefore, a membrane of Kevlar® cannot be made using simple evaporation techniques with H_2SO_4 as the solvent. For trial **H**, the mixture of Kevlar® in PPA/DMSO also produced a dark brown viscous liquid but at 150 °C. PPA may have also been acidic enough to break some of the amide linkages of Kevlar® to decompose the polymer.

3.4.2 Compatibility with the working fluids

A small piece (0.8 mg) of Kevlar®-DMSO/TBAF dried gel (membrane) was placed in a 10 g solution containing 85 wt% 1-phenyl-1-propanol and 15 wt% propiophenone (working fluid). This mixture was heated to 140 °C for 21 h using an oil bath and stirred using a magnetic stir bar. The mass loss was calculated to be 63%. It is likely that the working fluid dissolved a lot of the remaining DMSO and TBAF in the membrane, leaving mostly Kevlar® behind. However, the remaining product was still a film but it could be pulled apart by tweezers. This is to be expected as the membrane was small and very thin. Figure 3.6 shows a micrograph of this membrane after it was removed from the working fluid and patted dry using a lint-free tissue. The membrane appears to be more pitted after exposure to the working fluid than before (Figure 3.5). This would support the hypothesis that excess DMSO and TBAF was removed from the membrane.

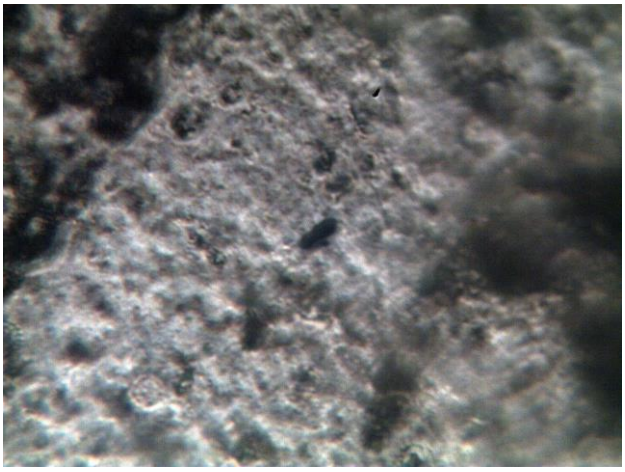

Figure 3.6: Kevlar®-DMSO/TBAF dried gel (membrane) after it was removed from the working fluid (85 wt% 1-phenyl-1-propanol and 15 wt% propiophenone) and patted dry with a lint-free tissue. Magnification is at 100x.

The solubility concerns with the Kevlar®-TBAF/DMSO dried gel (membrane) when exposed to the working fluid means that this membrane is not suitable for use in the proposed TRFC system. In addition, as DMSO and TBAF were removed very easily when the membrane was exposed to the working fluid, an H_3PO_4-doped version of this Kevlar® membrane would most likely leach as well, which would significantly reduce H^+ conductivity in the membrane. Therefore, the Kevlar®-DMSO/TBAF membrane or the Kevlar® membrane that has had the DMSO and TBAF removed would not be suitable for the proposed TRFC system.

3.5 Poly(allylamine) dihydrogen phosphate (PAADP)

3.5.1 Polymer preparation

The starting material for this product was 20 wt% poly(allylamine) (PAA) in H_2O. With the addition of 85% w/w $H_3PO_{4(aq)}$ to this solution, the poly(allylamine) dihydrogen phosphate salt was created. The reaction scheme is shown in Scheme 3.2 and the IR spectra detailing the reaction is shown below in Figure 3.7.

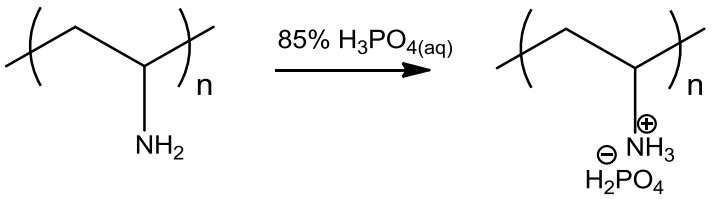

Scheme 3.2: Reaction of poly(allylamine) with 85% w/w $H_3PO_{4(aq)}$ to make poly(allylamine) dihydrogen phosphate.

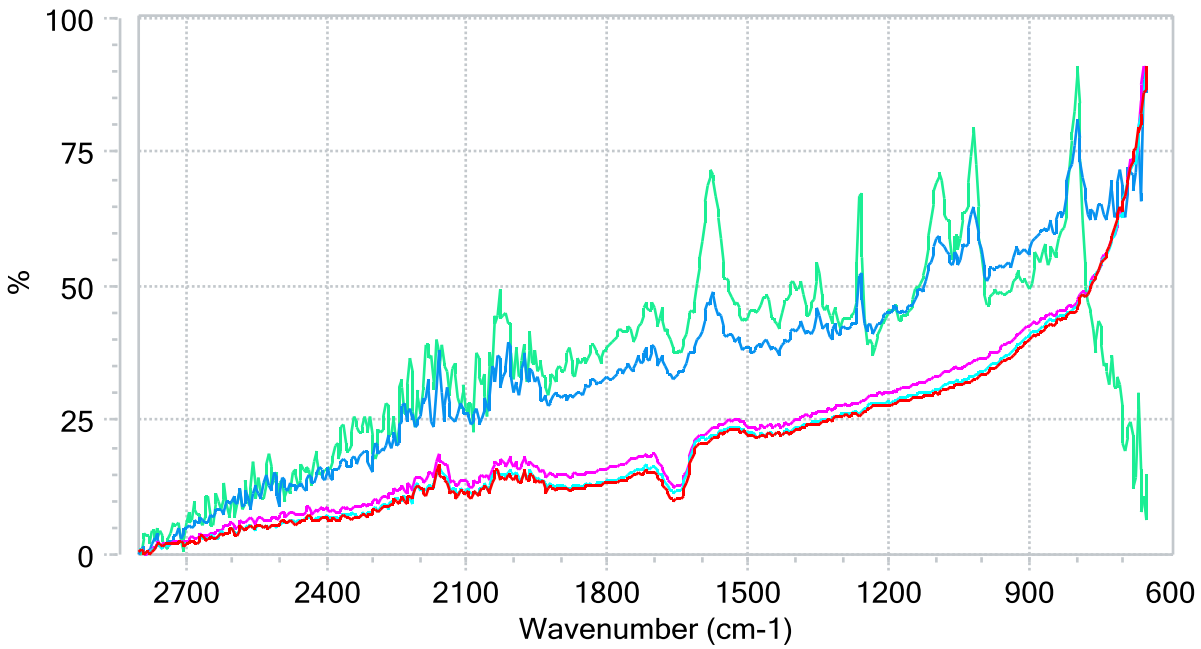

Time (min:sec)	15:08	21:08	27:08	33:08	41:08
Eq of H_3PO_4 added PRU* of PAA**	0	1	2	3	4

Figure 3.7: IR spectra showing the evolution of the reaction between poly(allylamine) and 85% w/w $H_3PO_{4(aq)}$ to make poly(allylamine) dihydrogen phosphate over 41 min. * PRU = per repeating unit. ** PAA = poly(allylamine).

Figure 3.7 details the evolution of peaks over time when 85% w/w $H_3PO_{4(aq)}$ was added to a 0.96 wt% solution of PAA in H_2O. Peak growth was seen after the addition of 3 eq of H_3PO_4 per repeating unit of PAA. According to Kuo et al, P=O and P-O stretches should appear at 1150 cm^{-1} and 990 cm^{-1}, respectively.[46] However, they only mention that these bands are associated with H_3PO_4 and not with $H_2PO_4^-$, which would have been present in their H_3PO_4-doped polymer. As the PAA was acidified with

excess equivalents of H_3PO_4 per repeating unit of PAA, some of the bands seen in Figure 3.7 will most likely be attributed to the P-O/P=O stretches of H_3PO_4. Kuo et al. also mention the N-H stretch appears at 1522 cm^{-1}.[46] The values seen in the spectrum shown in Figure 3.7 are approximately 45 cm^{-1} more per stretch than the values described by Kuo et al.[46] However, as the FT-IR spectrum is not shown by Kuo et al, it cannot be assumed that their peak assignments came from sharp peaks. Bozkurt reported the P-O and P=O stretches for poly(diallyldimethylammonium) dihydrogen phosphate (PAMADP) as a range spanning 100 cm^{-1}, as they found that their FT-IR spectrum peaks were too broad to make an accurate assignment.[40] When this is taken into account, the peak growth at 1021 cm^{-1} and 1096 cm^{-1} shown in Figure 3.7 could be the P-O and P=O stretches of $H_2PO_4^-$. The peak at 1583 cm^{-1} should be the N-H stretch associated with the amine group on PAA. The peak at 1583 cm^{-1} evolved from zero because the original PAA spectrum was subtracted from the baseline. This means that the N-H stretch became more pronounced as more of the amine groups were protonated on the polymer. This would increase the number of N-H bonds in the tested sample and therefore, increase the N-H stretch intensity seen in the IR spectrum.

3.5.2 Compatibility with the working fluids

Water is volatile enough to be used as the solvent for casting a membrane. By adding 85% $H_3PO_{4(aq)}$ to the 20 wt% solution of PAA in H_2O, a solution of poly(allylamine) dihydrogen phosphate (PAADP) in H_2O could be made. PAADP is initially insoluble in H_2O, but can be quickly re-dissolved with minimal agitation. Three equivalents of H_3PO_4 per repeating unit of PAA was mixed and agitated to re-dissolve the polymer. A membrane was cast onto a Teflon® liner to aid in removal, as it glues heavily to

glass. PAADP was also collected with 1 eq of H_3PO_4 per repeating unit of PAADP by not agitating the solution after adding the acid and then collecting the polymer by centrifuge and evaporation at 100 °C using a hot plate. Table 3.7 shows the solubility of PAADP-xH_3PO_4 in the working fluids.

Table 3.7: Solubility of PAADP-xH_3PO_4 membranes in the working fluids.

PAADP-xH_3PO_4	**Solvent**	**Dissolved**
PAADP-0H_3PO_4	Propiophenone	No
PAADP-0H_3PO_4	1-phenyl-1-propanol	No
PAADP-2H_3PO_4	Propiophenone	No
PAADP-2H_3PO_4	1-phenyl-1-propanol	No

PAADP-0H_3PO_4 (PAADP with zero equivalents of H_3PO_4 per repeating unit of PAADP) is very brittle, and it stuck to the glass petri dish when it was cast by evaporation. PAADP-2H_3PO_4 is very malleable and sticky, indicating that the doping level of H_3PO_4 is approaching a maximum before the acid dissolves the membrane. The membrane rapidly absorbs H_2O when exposed to air creating an even stickier membrane.

Although the polymer did not dissolve in the working fluids, its gel-like nature makes it difficult to work with as a PEM. Also, as the membrane is readily hygroscopic, keeping it in an anhydrous environment would be essential to ensure that the membrane remains as stable as possible. These difficulties would make working with this polymer difficult. As such, focus was diverted towards other polymers instead.

3.6 PAMADP and PAMAC copolymer

3.6.1 Polymer preparation

This polymer was synthesized by first using an ion exchange resin (Amberlite MB-20) on an aqueous solution of poly(diallyldimethylammonium) chloride (PAMAC) to make poly(diallyldimethylammonium) hydroxide (PAMAOH). PAMAOH was then acidified to poly(diallyldimethylammonium) dihydrogen phosphate (PAMADP) via the addition of 85% $H_3PO_{4(aq)}$. The reaction scheme for the synthesis of PAMADP is shown in Scheme 3.3. There were a few problems associated with the ion exchange procedure. With the original 20 wt% solution of PAMAC, the viscosity was too high to push the solution through the ion exchange resin in an efficient manner. An overpressure of argon was therefore required for the entire length of the column. However, this introduced some difficulty with regards to recovering the ion exchange product. Therefore, the PAMAC solution was diluted to 2 wt%, which flowed much better through the column and didn't require a constant positive argon pressure to allow the solution to percolate through the ion exchange matrix.

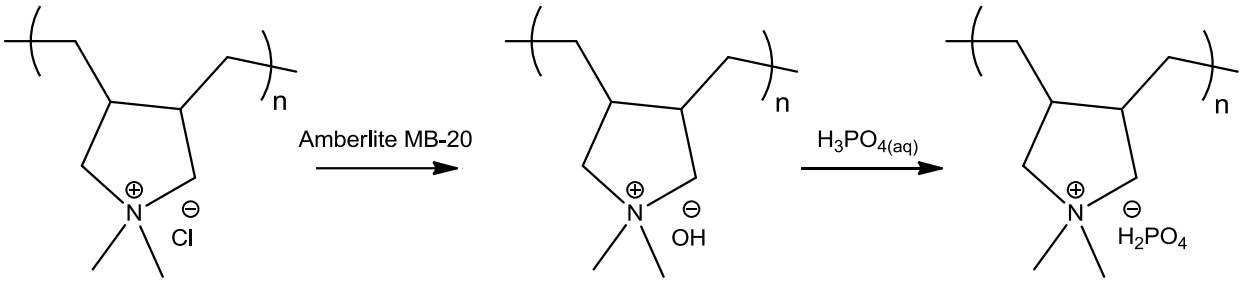

Scheme 3.3: The synthesis of poly(diallyldimethylammonium) dihydrogen phosphate.

The solution that was eluted from the column was slight yellow/green in colour. A sample was treated with $AgNO_3$ to determine if Ag_2O or AgCl would precipitate. For PAMAC, a beige solid precipitated, indicating AgCl. When the solution that was reacted with Amberlite MB-20 was tested with $AgNO_3$, a brown solid was recovered. This indicates both the black Ag_2O and beige AgCl co-precipitated and that there was a significant amount of PAMAC still left in solution. Although the presence of Cl^- will pose a problem for cathodic Pt poisoning,[65] the catalyst of choice for the proposed TRFC is Pd, which does not react with Cl^- under the operating conditions of the proposed fuel cell.[66] The anode catalyst for the proposed fuel cell is Pt, but it will not poison in the presence of Cl^-.[65] However, the chlorine may have adsorbed onto the surface of each electrode during its preparation. Therefore, it was cautiously decided to further investigate how this copolymer behaved in the presence of the working fluids. Equations 3.1-3 show the $AgNO_3$ reaction with both PAMAC and PAMAOH.

$$PAMA^+Cl^-_{(aq)} + AgNO_{3_{(aq)}} \rightarrow PAMA^+NO_3{}^-_{(aq)} + AgCl_{(s)} \quad 3.1$$

$$PAMA^+OH^-_{(aq)} + AgNO_{3_{(aq)}} \rightarrow PAMA^+NO_3{}^-_{(aq)} + AgOH_{(aq)} \quad 3.2$$

$$2AgOH_{(aq)} \rightarrow Ag_2O + H_2O_{(l)} \quad 3.3$$

Equation 3.1 represents the reaction that would occur if PAMAC was present. Equation 3.2 occurs in the presence of PAMAOH. AgOH immediately proceeds to Ag_2O and H_2O due to the favourable energetics of Equation 3.3.[67]

For the acidification of PAMAOH to PAMADP, in-situ FT-IR spectroscopy was completed to see the peak growth of over time of the new P-O and P=O stretches associated with $H_2PO_4^-$. Figure 3.8 shows the FT-IR spectra. The peak growths at 2347 cm^{-1}, 997 cm^{-1} and 954 cm^{-1} are in the correct range for the P-O stretch of the $H_2PO_4^-$ as described by Bozkurt.[40] However, the peak at 954 cm^{-1} could also be due to the quaternary ammonium group.[40] The peak growths at 1181 cm^{-1} and 1076 cm^{-1} also match the range attributed by Bozkurt to the P=O stretch in the PO_2^- group of $H_2PO_4^-$.[40] As the presence of free H_3PO_4 was possible during the FT-IR analysis, it is possible that some of the bands seen in Figure 4.7 are attributed to H_3PO_4. Bozkurt noted that P-O stretches should appear at 990 cm^{-1}, which is shown in Figure 3.8 after 4 eq of H_3PO_4 was added to the aqueous PAMAOH solution.[40] They note that the P-O stretch for $H_2PO_4^-$ is at 930 cm^{-1}, which is also shown in Figure 3.8 after 3 eq of H_3PO_4 was added.[40] The fact that the peak at 930 cm^{-1} did not show until after 3 eq of H_3PO_4 was added would suggest that the ion exchange between ^-OH and $H_2PO_4^-$ was slow. A titration was performed on PAMAOH with $HCl_{(aq)}$ to see how many Cl^- ions had exchanged with ^-OH ions during the ion exchange process in the ion exchange resin (Figure 3.9). Assuming the conversion of PAMAOH to PAMADP is 100%, the degree of $H_2PO_4^-$ ion pairing to the polymer could be established. It was discovered that the pH steadily increased for many hours after the addition of 107 µL of 12 mM $HCl_{(aq)}$ to 1 wt% PAMAOH solution in H_2O until equilibrium was established. This indicated that the ion exchange of PAMAOH to PAMAC was slow. The procedure was altered to titrate many individual PAMAOH solutions in H_2O at the same time with increasing increments of 12 mM $HCl_{(aq)}$ per solution. The solutions were left to stir on a shake table for 42 h. However, the initial concentration of PAMAOH per vial had to be lowered to 0.25 wt% in H_2O due to restrictions in the amount of available material. As $HCl_{(aq)}$ was added to PAMAOH, PAMAC and H_2O should be the products

of this titration. The calculated pH for the PAMAC starting material was 7.68. Therefore, the end point for this titration is pH 7.68. The conversion of PAMAC to PAMAOH was calculated to be 10%. Therefore, the polymer in solution was really a copolymer of PAMAC/PAMAOH. When H_3PO_4 was added to the PAMAC/PAMAOH solution, the copolymer was assumed to become PAMAC/PAMADP with the same 9:1 ratio.

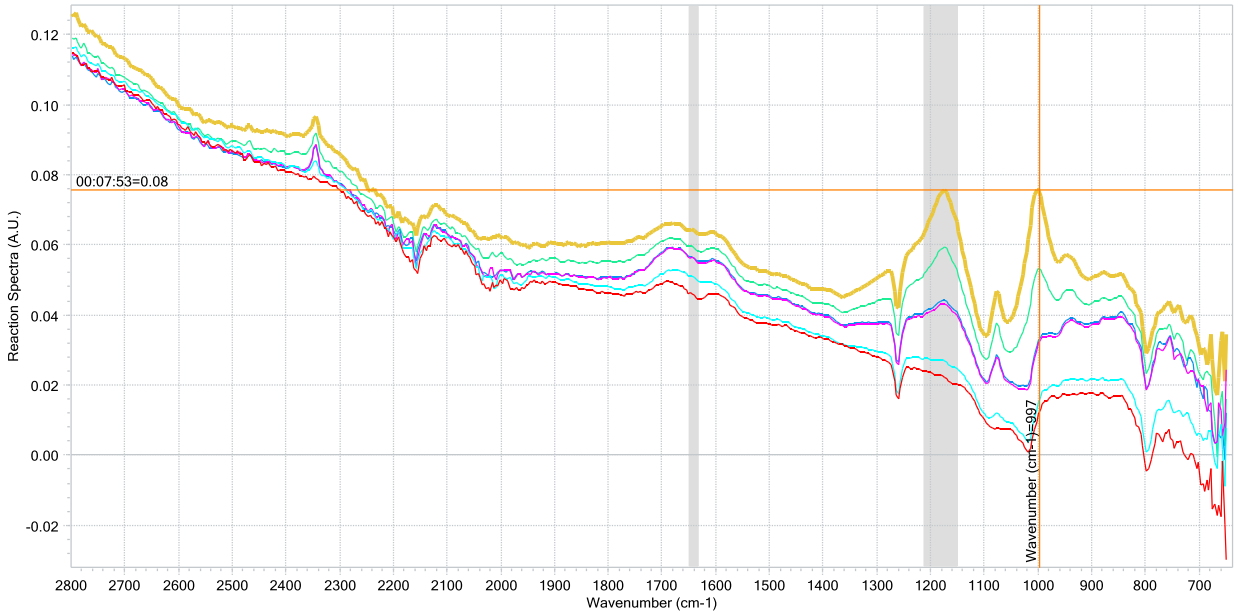

Time (min:sec)	00:53	01:53	02:53	03:53	04:53	07:53
Eq of H_3PO_4 added PRU of PAMAOH	0	1	2	3	4	5

Figure 3.8: In-situ FT-IR spectra showing the evolution of the reaction between $PAMAOH_{(aq)}$ and 85% w/w $H_3PO_{4(aq)}$ to make PAMADP over approximately 8 min.

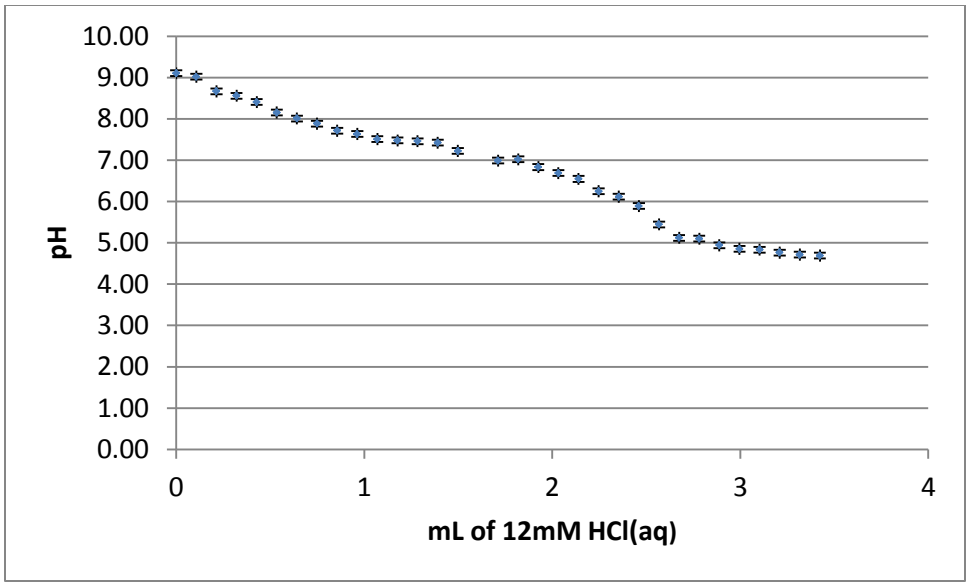

Figure 3.9: Titration curve of 12 mg of PAMAOH with x mL of 12 mM $HCl_{(aq)}$. The y-axis error is 0.07 pH points. The x-axis error is too small to print.

3.6.2 Solubility testing

A solution of PAMAC/PAMADP (9:1 by mol ratio) in H_2O was diluted with a number of different solvents to determine if the copolymer was soluble in a more volatile mixture for easier ink deposition. Table 3.8 shows the solubility of PAMAC/PAMADP in various solvents.

Table 3.8: Solubility limit of PAMAC/PAMADP (9:1 by mol ratio) in selected solvent mixtures with H_2O.

Co-solvent	Water Content (wt%)[a]	H_3PO_4 Molar Eq	Co-solvent[b] (wt%)
Acetone	90	1	10
Acetonitrile	82	1	18
Methanol	70	1	30
Tetrahydrofuran	78	1	22

[a] PAMADP is soluble in 100% H_2O. [b] Co-solvent concentration limit before precipitation of PAMADP.

The solvents shown in Table 3.8 either could not be used in sufficient quantities to effectively aid in lowering evaporation time versus H_2O or produced solutions that were too viscous for use in the airbrush. Therefore, the solvent that was chosen for the ink was H_2O.

3.6.3 Ink preparation and deposition

At this point 1 eq of H_3PO_4 per repeating unit of the poly(diallyldimethylammonium) backbone containing both the ^{-}OH and Cl^{-} ion pairs (molar ratio of 1:9, respectively) was used in the initial ink mixtures (trials **A** and **B** of Table 3.9). Also present in these mixtures was 10 wt% Pt/C, RTMI (10 wt% Pt loading on carbon). These inks were difficult to spray and frequently clogged the airbrush. However, once the ink used to deposit the catalyst bed dried on the surface of the CCGDL, it was resistant to abrasion.

An additive could help stabilize the catalyst particles by increasing viscosity and preventing agglomeration.[21] However, adding too much additive could cause the viscosity to be too high for the

airbrush. It may also reduce the contact area between the catalyst and ionomer, which would reduce the availability of the catalyst.[21] Glycerol has been used as an additive to aid in creating better catalyst ink suspensions.[21] The addition of glycerol (5 wt%, RTMM) to a mixture of 2 wt% PAMAC/PAMADP copolymer in H_2O, did not affect the solubility of the PAMAC/PAMADP copolymer in this solution. Table 3.9 shows ink compositions with varying glycerol concentrations. The inks were all deposited on carbon cloth with a back pressure of 1-5 PSI, and H_2O as the solvent.

Table 3.9: Ink compositions and preparation conditions of the PAMAC/PAMADP copolymer containing glycerol and final Pt loading on the CCGDL.

Trial	[Glycerol] (wt%)	[PAMADP/PAMAC] (wt%)[b]	[Pt/C] (wt% in Solution)	H_3PO_4 PRU[c] (eq)	Sonication		Pt Loading (mg/cm^2)[d]
					Power (W)	Time (min)	
A[a]	0	1.8	10	21	0.20	1	1.0
B	0	2.0	10	1	0.20	1	1.3
C	2	1.8	5	26	0.20	1	0.9
D	2	1.8	10	21	0.20	1	0.4
E	2	2.6	10	4.3	0.20	1	0.5
F	2	2.7	5	4.3	0.20	1	0.4
G	5	1.8	5	26	0.20	1	0.3
H	5	1.8	10	21	0.11	1	0.8
I	5	2.4	10	4.3	0.20	1	0.3
J	5	2.6	5	4.3	0.20	1	0.5
K	5	6.3	10	3.0	0.20	1.5	0.5
L	5	8.7	10	3.2	0.20	1.5	0.1

[a] THF was used in H_2O at 12 wt%, RTMI. [b] PAMAC and PAMDP coexist at a ratio of 9:1 in the mixture. [c] PRU = per repeating unit of PAMAC/PAMADP. [d] The Pt loading depended on how much ink was sprayed onto the CCGDL. The remainder of the ink composition (wt%) is solvent.

Glycerol did have an effect on ink homogeneity. The ink in trial **B** was difficult to spray without glycerol as an additive, and trial **A** was an attempt at lowering the evaporation time by adding a lower boiling point solvent (THF) to H_2O. Adding THF had the desired effect but just like **B**, the spray clogged the nozzle of the airbrush at every opportunity. However, the THF/H_2O ink was not tried with glycerol because some of the glycerol/H_2O mixtures deposited evenly and evaporated sufficiently well. For trials **C** and **D**, the end result was a complete lack of adhesion due to low PAMAC/PAMADP loading and low glycerol concentration. The absence of glycerol may have allowed agglomeration to occur, which could have yielded larger particles that could not be held in place on the CCGDL with its low polymer loading. Trials **E** and **F** performed better as the polymer loading on the surface of the CCGDLs was higher in trials **C** and **D**. All inks with glycerol at 2 wt%, RTMI, were excessively runny due to undesirably low viscosity. Trials **G** and **H** were better than **A-F** but were still not quite good enough. Trial **G** was easier to spray and did not clog the airbrush as much compared to trials **A**-**F.** Trial **H** suffered clogging issues due to a lack of adequate sonication, especially as it had more catalyst in solution than **G**. Trial **I** was one of the better performing trials as it produced a fine spray with no running liquid on the surface of the wet CCGDL. The ink from trial **I** did not clog the airbrush at all and the final result provided a very tough surface that could not be abraded. Trial **J** was too runny due to the low catalyst concentration. Trial **K** was also sufficient in spray and deposition quality, with a spray and final result comparable to **I**. The only issue with Pt loadings around 0.5 mg/cm^2 using 10 wt% Pt/C, RTMI, is that the catalyst bed became too thick. A solution to this problem would be to use 20-40 wt% Pt loading on carbon in order to reduce the thickness of the catalyst bed. Trial **L** was unsuccessful because the polymer concentration was too high to produce a fine spray. The ink for trial **L** also created a blotchy spray pattern that made achieving uniform coverage of the catalyst difficult. However, the benefit to using a high [PAMAC/PAMADP] is that the catalyst bed was very stable and could not be removed, even by using excessive force.

3.6.4 Compatibility of the CCGDL with the working fluid

CCGDLs from trials **I**, **K**, and **L** from Table 3.9 were subjected to an 85/15 w/w mixture of 1-phenyl-1-propanol/propiophenone at 140 °C for periods of 21, 22 and 24 h, respectively. The results suggest that the catalyst is more easily removed after exposure. The catalyst bed on **L** was very stable before exposure, but became unstable after exposure to the working fluid. The removal of catalyst was even easier than the untreated **A-F** trials, suggesting that the PAMAC/PAMADP copolymer had been removed from the CCGDL. Trial **K** was more stable than **L**, which could be because the finer spray allowed for deeper integration of the polymer within the catalyst bed. A blotchy application of the ink for trial **L** may have delayed settling of the catalyst onto the CCGDL enough that the catalyst particles could have agglomerated. This could have reduced the polymeric coverage leading to easier removal of the catalyst. Trial **I** provided similar results to **K** but the CCGDL lost less catalyst after exposure to the working fluid. A finer spray for trial **I** compared to the other trials may have provided the necessary integration of the polymer to keep it inside the catalyst bed, even after 21 h of exposure to the working fluid. Therefore, trial **I** provided the best conditions out of trials **A**-**L**.

3.6.5 Compatibility of the PAMAC/PAMADP copolymer membrane in the working fluids

A membrane of the PAMAC/PAMADP copolymer with 1 eq of H_3PO_4 per repeating unit of PAMAC/PAMADP (9:1 by mol ratio, respectively) (PAMAC/PAMADP-0H_3PO_4 = no free H_3PO_4) was

prepared and tested in pure propiophenone and pure 1-phenyl-1-propanol at 140 °C for 20 h. Figure 3.10 shows the result of the tests.

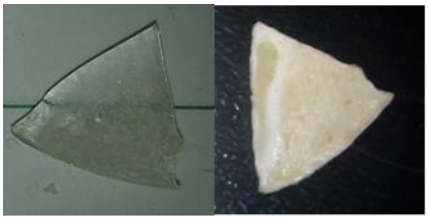

1-phenyl-1-propanol

Propiophenone

Figure 3.10: PAMAC/PAMADP-0H_3PO_4 membrane before (left) and after (right) soaking in 1-phenyl-1-propanol and propiophenone for 20 h at 140 °C.

Exposure to 1-phenyl-1-propanol turned the PAMAC/PAMADP-0H_3PO_4 copolymer membrane white. Propiophenone did not have the same effect on PAMAC/PAMADP membrane, but it did appear to embed itself inside the membrane as deduced by its slight yellow colour. The loss of mass for both membranes was approximately 4%. Figure 3.11 shows the optical micrographs of the two exposed membranes.

A)  B) 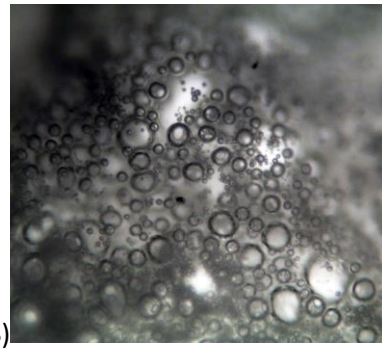 C) 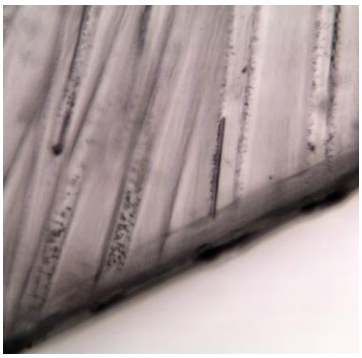

Figure 3.11: A) PAMAC/PAMADP membrane before exposure to propiophenone or 1-phenyl-1-propanol. B) PAMAC/PAMADP-$0H_3PO_4$ membrane after exposure to 1-phenyl-1-propanol at 140 °C for 20 h. C) PAMAC/PAMADP-$0H_3PO_4$ membrane after exposure to propiophenone under the same conditions. Magnification is 20x for all images.

Striations are seen on both the propiophenone treated and non-treated PAMAC/PAMADP membranes. However, striations are not seen on the membrane exposed to 1-phenyl-1-propanol. Striations are seen on membranes when polymeric sections are pulled together due to evaporation of solvent.[68] Evaporation of higher boiling point solvents like propiophenone are supposed to suppress the formation of striations, but this is only noted for spin coated membranes.[68] It is possible that the striations were caused by organized dehydration, which is most likely true for the non-exposed PAMAC/PAMADP membrane. This is because the striations were formed from the evaporation of water during the casting of the PAMAC/PAMADP membrane. The troughs are areas where the polymer has pulled away from itself. The striations for the PAMAC/PAMADP membrane appeared to be larger after the membrane was taken out of the hot propiophenone and padded dry with a lint-free tissue. This would suggest that the evaporation process of absorbed propiophenone produces more organization of the polymeric chains versus water evaporation.

The PAMAC/PAMADP membrane in Figure 3.10 (top) and Figure 3.11A changed from transparent to opaque after exposure to the hot working fluid. This may have been due to the polymeric chains becoming amorphous due to excessive 1-phenyl-1-propanol penetration causing a lack of polymeric chain organization. With long term exposure to air, this membrane recovered its clear, transparent state. The hygroscopic nature of PAMAC/PAMADP would mean that the polar H_2O molecules could favourably re-associate themselves with the ionic polymer and isolate the non-polar 1-phenyl-1-propanol away from the PAMAC/PAMADP polymeric chains. Unless the working fluid is kept saturated with H_2O at all times, this dehydration/rehydration cycle may ultimately damage the membrane. It is also expected that excess H_3PO_4 will leach out over time, especially if 1-phenyl-1-propanol (the main component of the working fluid at the cathode of the fuel cell) is permeating so deeply into the membrane. This would reduce ion conductivity of the PAMAC/PAMADP-xH_3PO_4 membrane considerably.

When the CCGDL was exposed to the working fluid at 140 °C, catalyst adhesion to the CCGDL was weakened substantially when using PAMAC/PAMADP-xH_3PO_4 as the binder. When the working fluid is in contact with a PAMAC/PAMADP-xH_3PO_4 membrane under the same conditions, the dehydration would cause problems for membrane stability over the long term. The dehydration would also suggest that the working fluid is also capable of leaching imbibed free H_3PO_4 from the PAMAC/PAMADP membrane, which is seen with PBI-based membranes in chapter 3.7.3.4. This would significantly reduce the H^+ conductivity of the membrane. Therefore, PAMAC/PAMADP-xH_3PO_4 would be a poor choice for use as an ionomer or membrane in the proposed TRFC system.

3.7 m-Phenylene polybenzimidazole (mPBI) (PBI 0.8IV, PBI S26, DPS PBI, CDPS PBI)

3.7.1 Solubility testing

The mPBI in PBI S26 was received as a 26 wt% solution in dimethylacetamide (DMAc). For PBI-based MEAs, DMAc has been shown in the literature to work well as the solvent for catalyst ink deposition or a casting solution for PBI membranes.[34,69] The PBI S26 solution in DMAc was diluted to either 5 wt% or 2 wt% for easier handling. The cross linked mPBI (CDPS PBI) starting material was a membrane provided by Danish Power Systems. A solubility trial of this membrane was attempted to see if CDPS PBI could dissolve into a solvent. The result was that CDPS PBI was not soluble in DMAc, DMSO or any common solvent and therefore, could not be used as part of an ink preparation. m-Phenylene polybenzimidazole from PBI Performance Products (PBI 0.8IV) was provided as a powder and solubility tests were also carried out to determine if it could be cast into a membrane or used as part of an ink preparation. PBI 0.8IV was not soluble in DMAc, but was soluble in DMSO up to 1.5 wt% at 180 °C. However, there were insoluble particles in the PBI 0.8IV/DMSO mixture that had to be filtered off.

3.7.2 DPS PBI

3.7.2.1 Ink preparation and deposition

The first ink composition attempted for a PBI-based system contained DPS PBI as the binder for the CCGDL. Seland et al. provided the method that was to be used for this initial test.[34] However, some of this procedure was modified to improve the results. The procedure was changed to exclude the deposition of a layer of Vulcan XC-72 and PTFE onto the carbon paper to make a MPL. Seland et al. added this layer to prevent the GDL from soaking during operation of the fuel cell.[34] However, this process was skipped as it was estimated that the working fluid would soak this surface anyway under operating conditions of the TRFC.

The modified preparation included depositing three major layers. The first major layer was a pure Vulcan XC-72 layer that was deposited by an ink containing Vulcan XC-72 (10 wt%, RTMI) and isopropanol.[34] The Vulcan XC-72 in this layer would fill as many of the gaps in the carbon paper as possible. A second layer of Vulcan XC-72 was deposited by an ink containing Vulcan XC-72 (10 wt%, RTMI), isopropanol (42.5 wt%, RTMI), and H_2O (42.5 wt%, RTMI).[34] Glycerol was added to this ink mixture (5 wt%, RTMI) to facilitate improved ink flow. This would provide a "mud-cracked" surface that would aid in producing a smooth surface for the catalyst layer to be deposited onto (third layer).[34] The third layer was deposited using an ink that contained Pt/C (10 wt%, RTMI), DPS PBI (1.5 wt%, RTMI), glycerol (5 wt%, RTMI) and DMAc (83.5 wt%, RTMI). Table 3.10 shows the different conditions used for CCGDLs made with the Seland et al. method.

Table 3.10: Airbrush trials using the Seland et al. method for DPS PBI-based CCGDLs.

Layer 1				
Trial	**Mixture**	**Sonication**		**Carbon Loading (mg/cm^2)**
		Power (W)	**Time (Min)**	
A	IPA, 10 wt% glycerol, 10 wt% Vulcan XC-72	0.20	1	3.8
B	IPA, 10 wt% glycerol, 10 wt% Vulcan XC-72	0.20	1	1.9
C	IPA, 10 wt% Vulcan XC-72	0.20	1	2.0
D	IPA, 10 wt% Vulcan XC-72	0.12-0.20	1	1.0
Layer 2				
Trial	**Mixture**	**Sonication**		**Carbon Loading (mg/cm^2)**
		Power (W)	**Time (min)**	
A	H_2O, 10 wt% Vulcan XC-72	0.20	1	CND
B	N/A	N/A	N/A	N/A
C	1:1 H_2O/IPA, 5 wt% glycerol, 10 wt% Vulcan XC-72	0.20	1	2.5
D	1:1 H_2O/IPA, 5 wt% glycerol, 10 wt% Vulcan XC-72	0.12-0.20	1	1.0
Layer 3				
Trial	**Mixture**	**Sonication**		**Pt Loading (mg/cm^2)**
		Power (W)	**Time (min)**	
C	DMAc, 1.5 wt% DPS PBI, 5 wt% glycerol, 10 wt% Pt/C	0.20	1.5	0.3
D	DMAc, 2.2 wt% DPS PBI, 5 wt% glycerol, 10 wt% Pt/C	0.12-0.20	1.5	0.3

*Trials **A**-**C** had an active area of 1 cm^2 and had carbon cloth GDLs. Trial **D** had an active area of 5 cm^2 and had a carbon paper GDL. CND means could not determine, due to physical loss of carbon. IPA = isopropanol.

Initially, a carbon layer was deposited onto carbon paper using isopropanol and glycerol as the solvent mixture (trial **A**), following previous experience with the flow patterns of the airbrush. A fibrous network of carbon particles was observed, which corresponded to the literature.[34] This network is shown in Figure 3.12. In addition, the "mud cracked" surface that was applied on top of the first layer was also verified by the image shown in Figure 3.12B. Figure 3.12B shows trial **B**, which was unfortunately unstable as the mud-cracked layer was easily removed from the surface. Therefore, a 1:1 w/w mixture of isopropanol and H_2O was used as well as Vulcan XC-72 (10 wt%, RTMI) for the second layer of **C** and **D** instead of just H_2O (90 wt%, RTMI) and Vulcan XC-72 (10 wt%, RTMI). This would reduce agglomeration of the carbon particles, which would prevent them from falling off the surface of the GDL. As the carbon particles of the second layer of CCGDLs **C** and **D** did not fall off the surface of the CCGDL that would suggest the agglomerations were reduced in size.

A) 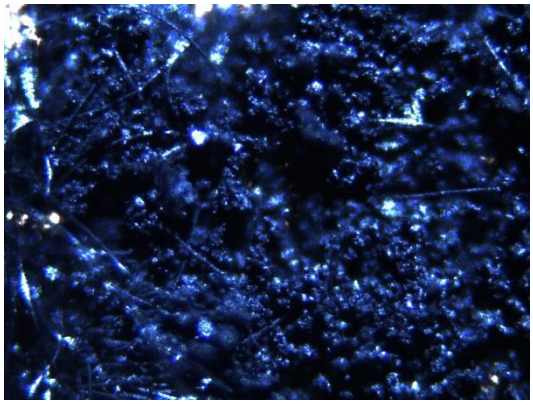 B) 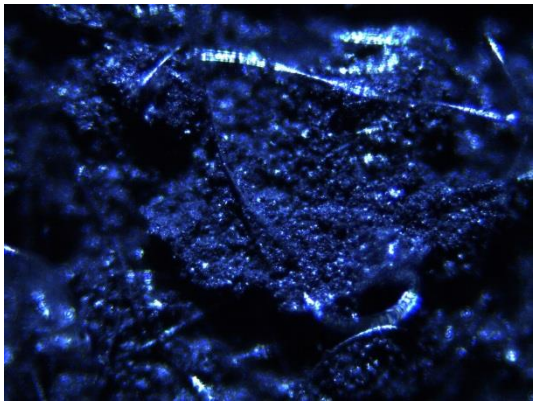

Figure 3.12: Micrographs of the individual layers of the DPS PBI-based CCGDL using the Seland et al. method.[34] A) First layer of the CCGDL containing Vulcan XC-72 carbon using an isopropanol mixture (85 wt%, RTMI) containing glycerol (5 wt%, RTMI) and Vulcan XC-72 (10 wt%, RTMI). B) Second layer of the CCGDL containing Vulcan XC-72 carbon using a 1:1 w/w mixture of isopropanol and H_2O and Vulcan XC-72 (10 wt%, RTMI). Magnification is 10x for **A** and 20x for **B**.

The deposition of the first layer of Vulcan XC-72 was also tried without using glycerol as an additive to see whether that would change the morphology of the carbon in the first layer. The results suggest it did not. Both structures appeared to be the same, as shown in Figure A3 (appendix). Therefore, trials **C** and **D** would not use glycerol as part of the ink during the first layer of Vulcan XC-72 deposition.

The third layer that was applied was the catalyst layer. Unlike the procedure described by Seland et al.,[34] glycerol was added to the ink to aid in homogeneity and ink flow through the airbrush. The solution was not able to maintain a smooth flow without it. The excess solvent on the CCGDL was evaporated at 80 °C using a hot plate. Figure 3.13 shows an optical micrograph of the final layer from trial **C**. The coverage was uneven for this layer, as shown by the large agglomerations on the surface of the CCGDL. This was caused by waiting too long when heating the CCGDL to evaporate the solvent. As a consequence, the time spent spraying the catalyst increased. Therefore, the catalyst agglomerated over time inside the airbrush reservoir, which made it difficult to spray onto the CCGDL. These larger particles were also not well adhered to the CCGDL surface. Therefore, the particles could easily be removed by slight abrasion with a finger or tissue. At this point, ink deposition was tried on a larger scale (trial **D**), which would use the ink more quickly and keep it from agglomerating inside the airbrush.

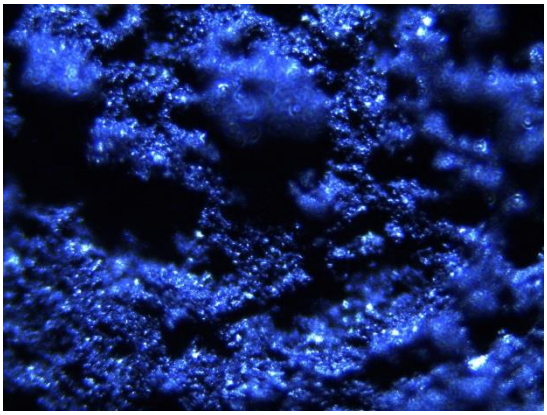

Figure 3.13: Final layer of the DPS PBI-based CCGDL from trial **C** using the Seland et al. method.[34] This layer contains Pt/C and DPS PBI in a ratio of 3:20 w/w, respectively. Magnification is 10x.

For trial **D**, the application procedure of all layers was easier to control due to the greater active area of the CCGDL. Seland et al. originally called for a Vulcan XC-72 deposition of 1 mg/cm^2 of layers one and two, which could not accurately controlled in trials **A**-**C**. Figure A4 (appendix) shows the first two layers of Vulcan XC-72 deposited onto the GDL of trial **D**. According to Seland et al., the deposition of catalyst should appear dendritic in nature.[34] Figure 3.14B did appear to show this phenomenon, suggesting that the structure of the third layer was appropriate to get good results inside a H_2/air-based fuel cell.[34] However, the drying time of the CCGDL was long enough at 100 °C for cracks to appear on the surface of the CCGDL that went right down to the carbon paper. Figure 3.14A shows this result. The high drying temperature of the CCGDL caused the solvent of the ink (DMAc) to evaporate too quickly. The vapour pressure of DMAc evaporating from the catalyst bed was enough to exceed its strength of cohesion, causing it to break. Therefore, all future PBI-based CCGDLs were dried at 50 °C to prevent the cracking of the catalyst bed from reoccurring. It was also determined that the connection of the first layer to the GDL was poor as the catalyst bed separated at this interface. A binding polymer should be added to every layer to improve the connection between each interface. Therefore, it was decided that

this method was not appropriate for the production of an mPBI-based CCGDL. However, the CCGDL shown in Figure 3.14A was tested in the working fluid of the proposed TRFC system to gain some valuable knowledge on how mPBI would behave under the operating conditions of the proposed TRFC.

A) 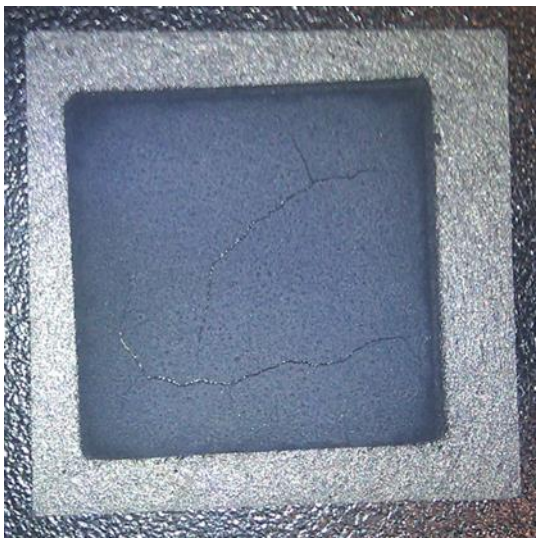 B) 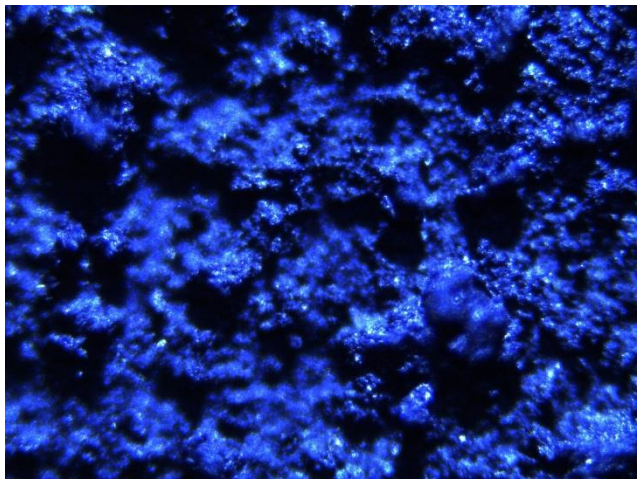

Figure 3.14: A) An image of a DPS PBI-based CCGDL (**D** from Table 3.10). This shows the cracks that developed on the surface of the CCGDL as the third layer was evaporated to dryness once the catalyst ink was applied. B) The third layer of **D** at a magnification of 10x.

3.7.2.2 Compatibility of the DPS PBI CCGDL in the working fluids

The final product of trial **D** from Table 3.10 was exposed to a mixture of 85 wt% 1-phenyl-1-propanol and 15 wt% propiophenone at 140 °C for 20 h. The initial exposure did exaggerate the cracks by curling the exposed edges upwards. The curling of the bed also allowed the magnetic stir

bar to take a large portion of the bed off the surface of the GDL. The extra cracks that appeared could have been prevented if the first layer of the catalyst bed had a better connection to the carbon paper, thus reducing any occurrence of vertical shear stress. Other than that, the integrity of the unbroken surface remained unchanged, which is a positive sign for PBI-based CCGDLs. Figure 3.15 shows this result.

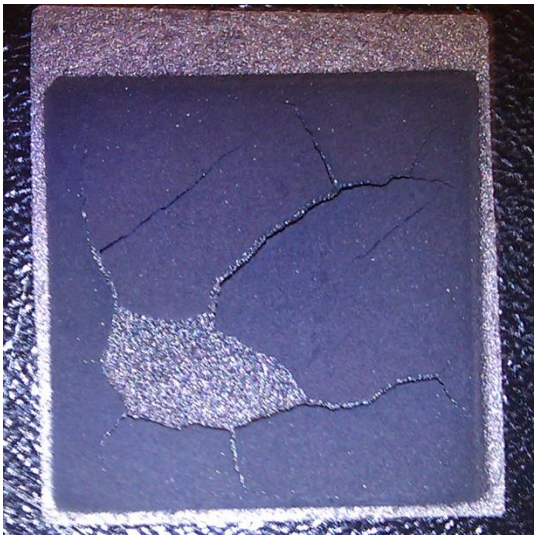

Figure 3.15: An image depicting the DPS PBI-based CCGDL from Figure 3.14A after it was exposed to a mixture of the working fluid (85 wt% 1-phenyl-1-propanol, 15 wt% propiophenone) at 140 °C for 20 h.

3.7.3 m-Phenylene polybenzimidazole from PBI Performance Products (PBI 0.8IV)

3.7.3.1 Polymer preparation

This polymer was provided as a powder, which varied in colours from light to dark brown. PBI 0.8IV is mPBI in powder form. Two trials had been conducted in the preparation of PBI 0.8IV. The first trial was to merely dissolve the PBI 0.8IV in hot DMSO. The second was to purify a solution of 2 wt% PBI 0.8IV in DMSO by heating the mixture to 180 °C and using a condenser to capture the lower boiling point compounds that were inside this mixture. After 27 h at 180 °C, a 0.5 g white powder had condensed onto the condenser. As the precipitate had a different ^{1}H NMR spectrum to mPBI,[70] it was deduced that the substance was not a low molecular weight oligomer of mPBI. The compound is thought to be a plasticizer as the polymer without it became brittle when cast as a membrane. The ^{1}H NMR spectrum indicates that it is not an aromatic compound as there are no peaks in the 6-8 ppm region, ruling out starting materials for PBI 0.8IV. There is a large singlet at 9.6 ppm, which could indicate an aldehyde group is present in this unknown compound. There are a few peaks in the 4-5 ppm region, indicating possible alkenes and methines. The data from the ^{1}H NMR spectrum is in chapter 2.4.3, while the spectrum is shown in Figure A7 (appendix). Electrospray ionization mass spectrometry (ESI-MS) was also performed on this unknown solid. The ESI-MS spectrum shows that there are a multitude of small molecules in the sample, with the largest peak, by far, at 404.041 m/z. This data is also given in chapter 2.4.3. It appears as though there is one major compound in the white solid as seen in the ^{1}H NMR

spectrum and the ESI-MS spectrum, although both spectra indicate that there are many minor compounds present in the white solid as well. None of these compounds were identified.

3.7.3.2 Ink preparation

An ink preparation was attempted with PBI 0.8IV as the binder, but it gelled in the sonicator after 15 seconds at 0.02 W. The ink composition contained 5 wt% glycerol (RTMI), 10 wt% Pd/XC-72 (RTMI) (20 wt% Pd loading on XC-72 carbon), 1.5 wt% mPBI (RTMI), and all of the plasticizers present in PBI 0.8IV. After this test, PBI S26 replaced PBI 0.8IV for PBI ink preparations as both contain the same mPBI polymer. PBI S26-based inks did not gel as easily after sonication.

3.7.3.3 Membrane casting

A 1 wt% solution of PBI 0.8IV was made in DMSO. This was cast at 80 °C for 5 h. The result is shown in Figure 3.16A. Another preparation involved casting the polymer without the plasticizers that were present in the starting material. The final solution for this preparation was 1.5 wt% PBI 0.8IV in DMSO and was cast with the same procedure as described for the 1 wt% solution. Figure 3.16B/C shows the result of this cast.

A)  B) 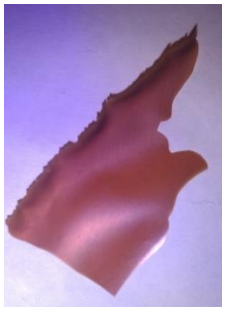 C) 

Figure 3.16: Attempts at casting PBI 0.8IV. A) The membrane cast with plasticizers included. B/C) The membrane obtained by casting purified PBI 0.8IV membrane, showing how brittle it is.

The plasticizers assisted in creating a stable, flexible membrane that will resist physical stress. For use in a fuel cell, it is important for the membrane to have good physical strength, as the membrane will undergo heat and swelling stress that will reduce the life expectancy of the membrane. The plasticized membrane cracked a little during casting. These cracks occur because the solvent evaporated too quickly and therefore, the polymer chains did not have enough time to relax back into position in the membrane.[71] A non-cracked membrane could be prepared by lowering the temperature of evaporation and by introducing a slow, steady flow of inert gas across the surface of the casting solution as shown in chapter 3.7.4.2. This would allow a slow and steady rate of solvent evaporation, which should prevent cracks developing in the membrane. However, these changes were not attempted for PBI 0.8IV.

3.7.3.4 Membrane doping and compatibility with the working fluid

The plasticized version of the membrane was doped and tested in the working fluid. It was decided by the author that a doping level of 6 eq of H_3PO_4 per repeating unit of mPBI would yield sufficient H^+ conductivity and yet still keep the stability of the membrane intact.[33,72] The doping level is directly related to the concentration of H_3PO_4 the membrane is soaked in.[72] The doping level of the membrane will eventually reach a specific equilibrium when immersed in the appropriate concentration of $H_3PO_{4(aq)}$.[72] Optical micrographs were being taken of the non-doped and doped membranes, as seen in Figure 3.17A/B. In the doped membrane, little bubbles can be seen in the larger craters. These bubbles could suggest the presence of H_3PO_4 in the membrane. While the micrographs were taken, the bubbles grew in size. This could indicate that the H_2O from the atmosphere was being absorbed into the membrane and therefore, the combined H_2O and H_3PO_4 solution would seep out of the membrane due to the extra volume of the H_3PO_4 and H_2O doped into the membrane. The mass of the H_3PO_4-doped and non-doped PBI 0.8IV membranes increased after they were taken out of the oven suggesting that the PBI 0.8IV membrane is hygroscopic. The same bubbling effect was not seen with the non-doped PBI 0.8IV membrane.

Both membranes were exposed to a mixture of 85 wt% 1-phenyl-1-propanol and 15 wt% propiophenone at 140 °C for 16 h. The non-doped membrane gained 2.3% by weight due to uptake of the working fluids but the doped membrane lost a staggering 45% by weight. If the loss is assumed to be of H_3PO_4 alone, the mass loss is 69% of the H_3PO_4 content in the membrane. This would have devastating effects on the H^+ conductivity of this membrane. Figure 3.17C shows the lack of small bubbles on the surface, suggesting that H_3PO_4 has been removed from the membrane by the working fluid. These small bubbles never returned when the membrane was left open to the atmosphere after

the membrane was taken out of the working fluid (85 wt% 1-phenyl-1-propanol, 15 wt% propiophenone). The pitted surface of the membrane was also of concern. Uniformity in surface topography would increase the contact of the membrane with the CCGDL inside the fuel cell. This increased contact would allow more H^+ transfer between the catalyst and the membrane and therefore, better performance of the fuel cell. The surface of the PBI 0.8IV membrane shown in Figure 3.17A-C was much rougher than the PBI S26 membranes shown later.

A) 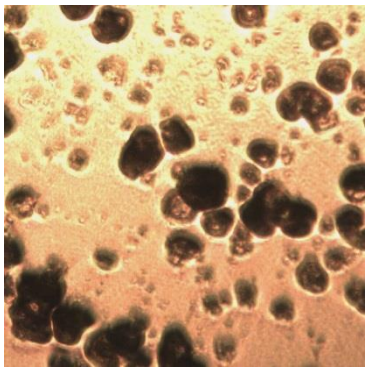 B) 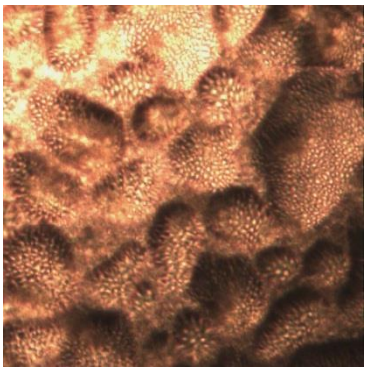 C) 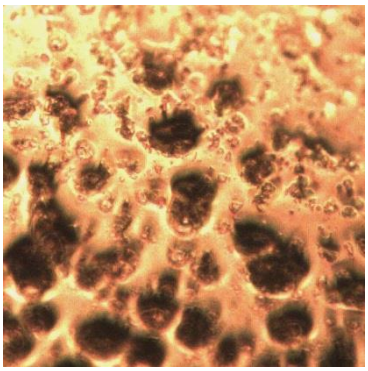

Figure 3.17: A) The non-doped PBI 0.8IV membrane. B) PBI 0.8IV doped to 4x H_3PO_4. C) The H_3PO_4-doped PBI 0.8IV membrane after exposure to the working fluid (85 wt% 1-phenyl-1-propanol, 15 wt% propiophenone) for 16 h at 140 °C. Magnification is 10x for all images.

As it was not possible to prepare a usable catalyst ink containing PBI 0.8IV or a PBI 0.8IV membrane smooth enough to use in a MEA, it was decided that other variants of mPBI would be used instead of PBI 0.8IV. Even though PBI 0.8IV is stable in the working fluid, the H_3PO_4-doped PBI 0.8IV is not, as the H_3PO_4 is leached in large amounts to the working fluid. As mPBI is the polymer that is contained in PBI 0.8IV, other mPBI materials (DPS PBI, PBI S26) would suffer the same leaching problems as PBI 0.8IV. The H_3PO_4 loss from the PBI 0.8IV membrane was noted but the aim of this project was to prove that the TRFC is at least plausible in practice. Therefore, membrane and ink preparation research was continued with other PBI ink and membrane preparations, namely PBI S26, so that a fuel cell could be built and tested.

3.7.4 PBI S26

3.7.4.1 Ink preparation and deposition

PBI S26 replaced the other mPBI materials because they were either hard to work with (PBI 0.8IV), or they were not available for use due to short supply (DPS PBI). It was also at this point that the catalyst was changed to either 20 wt% Pt/XC-72 or 20 wt% Pd/XC-72 for each CCGDL. This is because the amount of mass in the catalyst bed had to be reduced to allow for better utilization of the catalyst in a fuel cell. In addition, the appropriate catalysts for the anode and cathode of the proposed TRFC needed to be represented. The anode would now be represented by Pt/XC-72 and the cathode would be represented by Pd/XC-72. Pd/XC-72 is the preferred catalyst for use in the hydrogenation reaction, which would occur at the cathode.[11] The data that was collected from the fabrication of each

PBI S26-based CCGDL is shown in Table 3.11 (next page). All Pt/XC-72 inks containing PBI S26 (2 wt%, RTMI) that are detailed in Table 3.11 were homogeneous and flowed very well through the airbrush. They also always produced a smooth surface upon deposition. Pd/XC-72 inks containing PBI S26 did clog the airbrush after approximately 15 minutes in the reservoir, and the deposition was not as uniform as the Pt/XC-72 inks. The surface of the Pd/XC-72 electrode often had patchy white and black areas, indicating that the polymer may have precipitated in large regions. This could affect fuel cell performance because the mPBI may not have been sufficiently bound to the available catalyst, leaving large amounts of catalyst either completely covered, or isolated from H_3PO_4-doped mPBI.

It was also discovered that the ink would need to be fresh to reduce the possibility of the PBI ink coagulating under sonication. Sonicating the PBI S26-based catalyst ink for 90 s has the same effect on a fresh ink mixture. It was determined that 60 s was the correct amount of time required to make a stable, homogeneous mixture that would not agglomerate over the ink deposition time frame.

Table 3.11: PBI S26-based electrode data for CCGDLs showing Pd or Pt catalyst loading on the electrode surface and sonication time for the ink that was used to spray the catalyst onto the surface of each carbon paper GDL.

20 wt% Pd/XC-72			20 wt% Pt/XC-72		
Trial	**Sonication Time (s)**	**Pd Loading (mg/cm^2)**	**Trial**	**Sonication Time (s)**	**Pt Loading (mg/cm^2)**
A1	15, 3 s pause, 10	0.4	**B1**	15, 3 s pause, 10	0.4
A2	15, 3 s pause, 10	0.5	**B2**	15, 3 s pause, 10	0.4
A3	15, 3 s pause, 10	0.4	**B3**	15, 3 s pause, 10	0.5
A4	15, 3 s pause, 10	0.5	**B4**	60	0.5
A5	15, 3 s pause, 10	0.4	**B5**	60	0.5
A6	60	0.5	**B6**	60	0.5
A7	60	0.5	**B7**	60	0.5
A8	60	0.5	**B8**	60	0.5
A9	60	0.5	**B9**	60	0.5
A10	60	0.5	**B10**	60	0.5
A11	60	0.4	**B11**	60	0.5
A12	60	0.4	**B12**	60	0.5
A13	60	0.4			
A14	60	0.4			

3.7.4.2 Membrane casting

PBI S26 membranes were first cast onto petri dishes at 80 °C on a hot plate. Unfortunately, the casting of PBI S26 was uneven, creating regions of high and low thickness. This was largely due to an uneven evaporation rate of DMAc caused by excessive temperature and fluctuating air patterns inside the fume hood. Figure 3.18A shows the result. All of the other casting methods of PBI S26 using a petri dish and a 5 wt% PBI S26 solution in DMAc ended in the same manner as seen in Figure 3.18A. The casting method of PBI S26 that used the template shown in Figure A4 (appendix) also produced the same product as the petri dish casts of PBI S26. This suggests that the flatness of the casting surface was not the problem in trying to make a membrane with a uniform topography and thickness.

A 5 wt% PBI S26 solution was cast in HCO_2H at room temperature. Unfortunately, the polymer could not form a successful membrane as it cracked severely when it dried. Formic acid molecules may have solvated the chains well enough that the mPBI chains could not form extended intermolecular interactions with each other before the formic acid had completely evaporated. This lack of mPBI interaction created a crack when the solvent had evaporated. Therefore, the cracks that resulted in the membrane prevented a complete film from being cast. This membrane is shown in Figure 3.18B.

A)  B)  C) 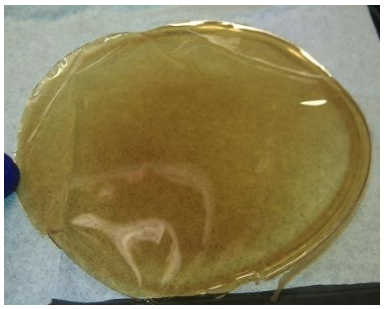

Figure 3.18: Different attempts at casting PBI S26 membranes. A) A membrane casted from a 5 wt% PBI S26 solution in DMAc at 80 °C. B) A membrane casted from a 5 wt% PBI S26 solution in HCO_2H at room temperature. C) A membrane casted from a 5 wt% PBI S26 solution in DMAc at 50 °C with a steady Ar flow in an atmosphere bag.

A successful PBI S26 membrane was created when a 5 wt% PBI S26 solution in DMAc was cast inside the template shown in Figure A6 (appendix), at 50 °C for 4-5 h with a steady, slow argon flow in an atmosphere bag. The result can be seen in Figure 3.18C. The thickness of this successful membrane was measured to be approximately 40 µm, and was fairly uniform. The membrane was also fairly robust to stress when it was applied to the horizontal plane of the membrane. It could not be pulled apart as easily as PBI 0.8IV, indicating that the PBI S26 membrane is superior in strength to the PBI 0.8IV membrane. This increase in strength would also be better for use in the proposed TRFC system to increase the operating life of the MEA.

3.7.4.3 Membrane and CCGDL doping and compatibility with the working fluids

PBI S26-based membranes and CCGDLs were doped in the same fashion as PBI 0.8IV membranes. Figure 3.19 shows the difference between the doped and non-doped membranes. These images are a little different from those seen for PBI 0.8IV in Figure 3.17A-C. There are areas where H_3PO_4 has beaded on the surface, but not as much as on the PBI 0.8IV membrane shown in Figure 3.17B. The surface is also much smoother. The images shown in Figure 3.19 are at 20x magnification and these images show much smaller troughs than the troughs seen on the surface of the PBI 0.8IV membrane (Figure 3.17A-C). It is clear that these membranes are much better prepared than the PBI 0.8IV attempt. The uniform topography will increase fuel cell performance compared to the uneven surface presented by the PBI 0.8IV membrane.

A) 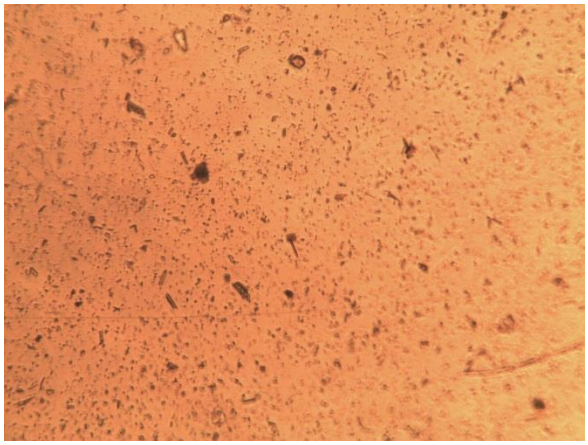 B) 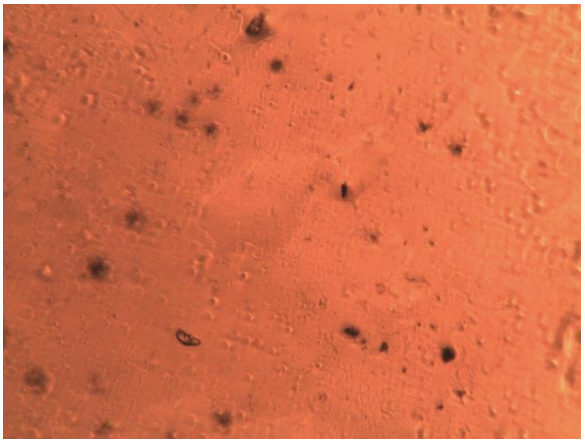

Figure 3.19: A) Non-doped PBI S26 membrane. B) H_3PO_4-doped PBI S26 membrane (4 eq). Magnification is 20x for both and the images are depicted in true colour.

The doping data for each PBI S26 membrane is shown in Table 3.12. The doping level refers to the number of equivalents of H_3PO_4 per repeating unit of mPBI. There is a standard deviation of 2.2 eq between all of the samples. Although most of the deviation was caused by using a larger size template for batch 4, it is unclear why these membranes could not uptake as much H_3PO_4 as the others. The standard deviation with batch 4 excluded is 1.7 eq, and 0.8 eq if the outlier of trial **E** is removed. It is also unclear as to why trial **E** has absorbed far more H_3PO_4 than the others as it was part of the same batch of membranes as trials **D** and **F**. When **E** is removed, it is shown that the doping levels are similar when compared to membranes of the same batch.

Table 3.12: H_3PO_4 doping levels in PBI S26 membranes.

Batch[a]	Trial	Doping Level (eq)
1	A	7.0
1	B	6.1
1	C	6.8
2	D	6.3
2	E	11.4
2	F	8.2
3	G	5.5
3	H	6.2
3	I	5.6
4	J	3.6
4	K	3.7
4	L	3.7
4	M	3.6
4	N	3.7
4	O	3.0

[a] Each individual membrane was cut from a larger membrane. The membranes that were cut from the same larger membrane belong to the same batch. Batches 1-3 were made by casting a 5 wt% solution of PBI S26 in DMAc at 50 °C for 4-5 h using the setup shown in Figure A6 (appendix). The rest of the procedure is described in the first paragraph of chapter 2.4.2. Batch 4 was made using the same PBI S26 solution but using a larger (glass cylinder) template, measuring 12 cm in diameter, which required 6-7 h casting time at 50 °C.

Both non-doped and doped membranes of PBI S26 were placed inside a 20 mL glass vial containing 10 mL of propiophenone. The contents of this vial were heated for 18 h at 120 °C. Table 3.13 shows the initial and final masses of the sample membranes, before and after exposure. These results

shown in Table 3.13 are consistent with the results seen for PBI 0.8IV as seen in chapter 3.7.3.4. The total loss of mass of H_3PO_4 in the PBI S26 membrane is far too high for the long-term use of a PBI S26-based MEA in the proposed TRFC system. The total H_3PO_4 mass lost from the PBI S26 membrane is 50%, which is comparable to the 69% seen for PBI 0.8IV under warmer conditions. The non-doped working fluid compatibility test is also in line with PBI 0.8IV and further proves the stability of non-doped mPBI under the operating conditions in the TRFC.

Table 3.13: Percent mass loss of H_3PO_4-doped and non-doped PBI S26 membranes before and after exposure to propiophenone at 120 °C for 20 h.

PBI S26 Membrane	Mass Before Exposure (mg)	Mass After Exposure (mg)	Total Mass Loss (%)
Doped to 6x H_3PO_4	38.5*	25.8	33
Non-doped	13.5	12.9	4

*13.1 mg before doping with 12M $H_3PO_{4(aq)}$ for 2 d.

PBI S26 still leaches too much H_3PO_4 to be considered as the membrane and catalyst binder for the proposed TRFC system over the long term. However, PBI S26 MEAs could still provide invaluable data on the validity and performance of the envisioned TRFC.

3.7.5 Cross-linked Danish Power Systems m-phenylene polybenzimidazole (CDPS PBI)

3.7.5.1 Membrane doping

The doping procedure was changed on the recommendation of the supplier compared to PBI S26 membranes. The doping levels of H_3PO_4 in each membrane are shown below in Table 3.14. However, the doping level calculation assumes that the mass of the non-doped membranes is due to mPBI. The amount of repeating units of mPBI is calculated from this mass. If a cross-linker is present, its mass will subtract from the total and therefore reduce the calculated amount of repeating units of mPBI. Unfortunately, the H_3PO_4 doping levels inside the CDPS PBI membranes are approximations because the cross-linker is unknown. As a result, its mass cannot be taken into account in the doping level calculation, causing the actual doping level to be higher than calculated. The doping method (detailed in chapter 2.5.4) was repeated in the exact same manner for all three trials, and yet, the variability is shown to be high (Table 3.14). Differences in the batch were not a problem here as each membrane was cut from the same batch. The doping level variability could be due to differences in the local morphology of each membrane and how well H_3PO_4 penetrates into the membrane. Due to this conclusion, it was determined that the time of 2 h recommended by the supplier was not enough to dope the membrane to the specified 6 eq of H_3PO_4 per polymeric repeating unit of mPBI. It can also be noted that 2 eq of H_3PO_4 per repeating unit of polymer is required for good conductivity in mPBI-based membranes.[72] Therefore, it is likely that the membrane from trial **A** would probably not perform as well

as the membrane from trial **B** in a fuel cell because membrane **B** likely has a doping level of at least 2 eq when the cross-linker is taken into account as part of the doping level calculation.

Table 3.14: Doping levels of H_3PO_4 in CDPS PBI membranes.

Trial	H_3PO_4 Doping Level (eq)
A	0.8
B	1.7
C	3.2

3.7.5.2 Compatibility with the working fluids

One piece of CDPS PBI was doped with 85 wt% $H_3PO_{4(sq)}$ for 2 h at 80 °C. The membrane was then placed inside a 10 g solution of 85 wt% 1-phenyl-1-propanol and 15 wt% propiophenone (working fluid) along with a magnetic stir bar and heated to 120 °C using an oil bath for 20 h. The membrane was then removed from the mixture and patted dry with a lint-free tissue and weighed on a mass balance. A non-doped CDPS PBI membrane was placed inside another mixture of the working fluid under the same conditions. This membrane was removed from the working fluid and patted dry with a lint-free tissue as well. The masses of the membranes before and after exposure to the working fluid are recorded in Table 3.15. The mass loss of the H_3PO_4-doped CDPS PBI membrane is 12%. This is considerably lower than the PBI S26 or PBI 0.8IV H_3PO_4-doped membranes. This suggests that the crosslinking agent in

CDPS PBI allows the membrane to retain the free H_3PO_4 better than the other PBI membranes that were tested.

Table 3.15: The masses of a doped and non-doped CDPS PBI membrane before and after exposure to a 10 g mixture of 85 wt% 1-phenyl-1-propanol and 15 wt% propiophenone at 120 °C for 20 h.

CDPS PBI Membrane	Mass Before Exposure (mg)	Mass After Exposure (mg)	Total Mass Loss (%)
Doped to 2.1x H_3PO_4	29.7*	26.2	12
Non-doped	15.0	15.1	-1

*17.7 mg before doping with 85 wt% $H_3PO_{4(aq)}$ for 2 h.

As the CDPS PBI membrane still leaches H_3PO_4 into the working fluid it is not a successful candidate for use in the proposed TRFC system in the long term. However, its use inside an MEA can provide useful information into how the proposed TRFC system could work over the short term until a more suitable membrane is found.

3.7.6 Attempt at making sulfonated m-phenylene polybenzimidazole (SS26)

3.7.6.1 Polymer preparation

SS26 was synthesized by reacting mPBI from PBI S26 in fuming sulfuric acid using the procedure explained in chapter 2.2.3. The reaction is shown below in Scheme 3.4. The FT-IR spectrum for SS26 is shown in Figure 3.20, with Figure 3.21 being the FT-IR spectrum of the starting material (PBI S26).

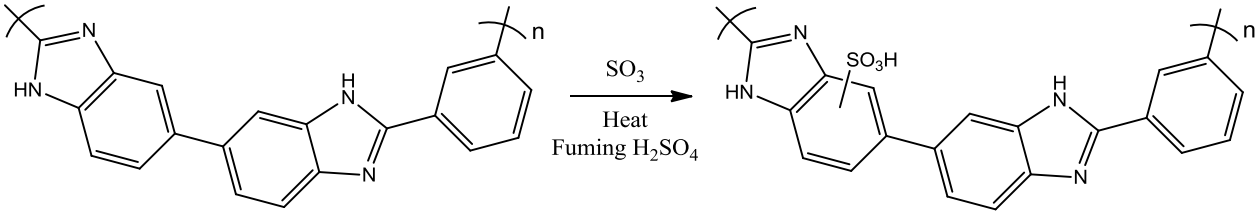

Scheme 3.4: Reaction of mPBI with SO_3 (from fuming H_2SO_4) to form sulfonated mPBI.

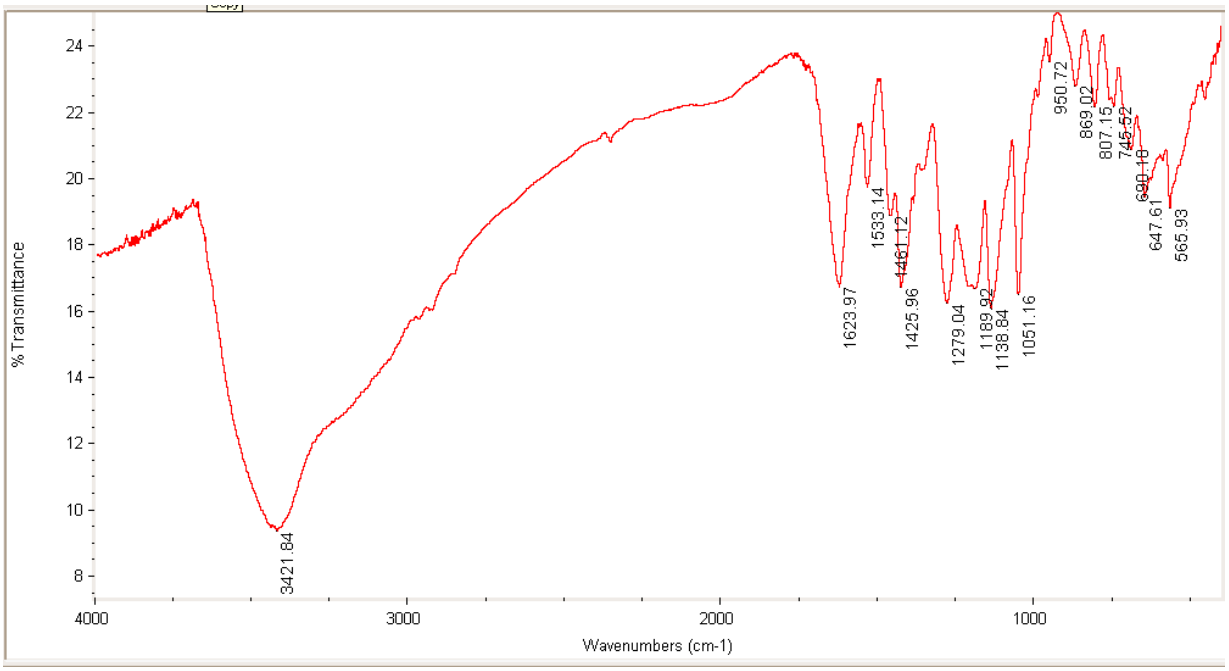

Figure 3.20: FT-IR spectrum of SS26 prepared as described in chapter 2.2.3 (KBr pellet).

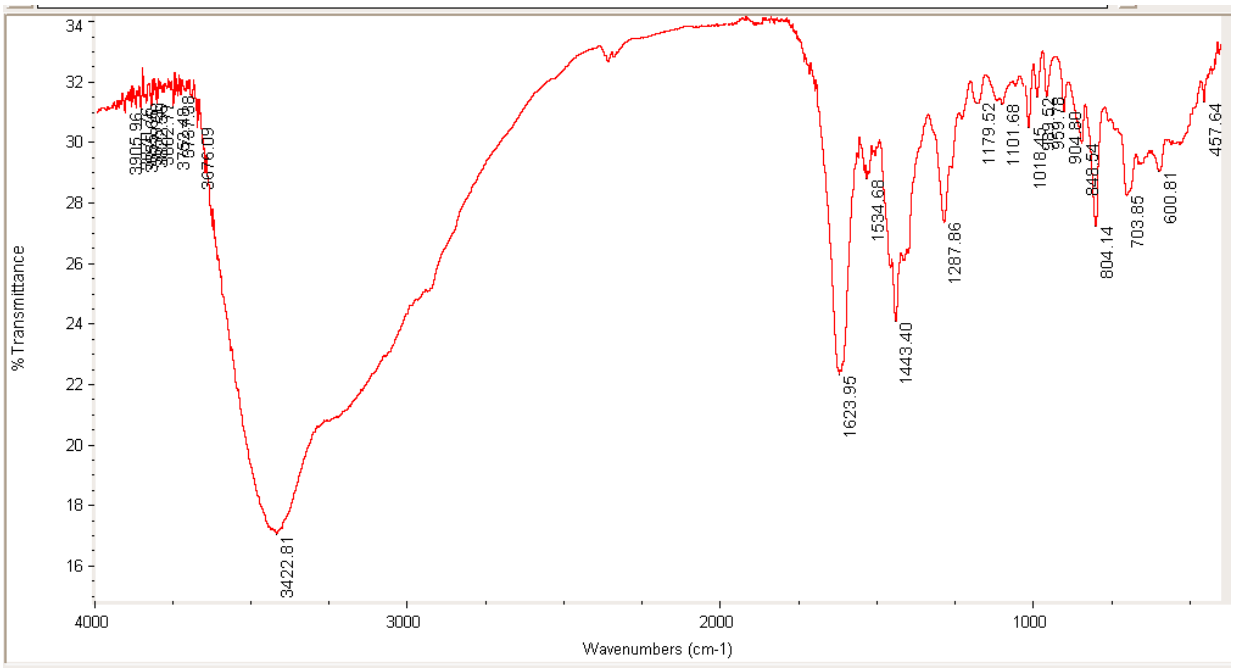

Figure 3.21: FT-IR spectrum of PBI S26 starting material in a KBr pellet.

Ariza et al. report the asymmetric and symmetric bands of the sulfonated group for sulfonated mPBI at 1170 cm^{-1} and 1050 cm^{-1}, respectively.[18] However, the spectrum they report is not well defined between 1200 and 900 cm^{-1}. The peak at 1047 cm^{-1} is associated with HSO_4^- according to Lund Myhre et al.,[73] where the HSO_4^- is most likely ion paired to the positively charged imidazole nitrogen. Lund Myhre et al. also describe a band at 1192 cm^{-1}, which they also attribute to free aqueous HSO_4^-.[73] Therefore, the peak seen at 1189 cm^{-1} in Figure 3.20 is most likely attributed to HSO_4^-, which is ion paired with the positively charged nitrogen on the imidazole. The HSO_4^- peak location described by Lund Myhre is not a perfect reference for the S=O stretching band of HSO_4^- as it is ion paired to an imidazole nitrogen on SS26 rather than freely associated with H_2O. However, SS26 was exposed to H_2O when the polymer was precipitated from the H_2SO_4 and could have pockets of trapped H_2O inside the powder that could not be removed by the drying process in the vacuum oven. The band in Figure 3.20 at 3421 cm^{-1} could be an overlay of both the O-H and N-H stretches of H_2O and SS26, respectively. Ariza et al. describe new band growth in the region of 550 to 680 cm^{-1} and around 885 cm^{-1}, which they say are characteristic of H_2SO_4, SO_4^{2-}, HSO_4^- and H_2SO_3.[18] The growth seen in Figure 3.20 between 565 cm^{-1} and 690 cm^{-1} matches this growth. However, the growth Ariza et al. saw around 885 cm^{-1} is not present.[18] This peak is also attributed to HSO_4^- as well,[73] and it is unknown why it is missing. The peak at 1139 cm^{-1} in Figure 3.20 is undetermined and is not shown in the sulfonated mPBI FTIR spectra that Ariza et al. compiled.[18]

The FT-IR spectrum shown in Figure 3.20 does not prove the existence of a sulfonated mPBI. It only suggests the presence of [$mPBI^+HSO_4^-$]. Also, the difference between the FT-IR spectra of sulfonated mPBI and [$mPBI^+HSO_4^-$] is small.[18] Ariza et al. mention differences in the peaks between 600 and 700 cm^{-1} to tell the difference between [$mPBI^+HSO_4^-$] and grafted sulfuric acid. As Figure 3.20 shows very little absorption between 600 and 700 cm^{-1}, it would suggest that [$mPBI^+HSO_4^-$] was the product and not sulfonated mPBI. It is unclear why this method did not produce the correct product as it was a similar method to what was used to sulfonate another PBI based derivative.[74]

Both ^{1}H and ^{13}C NMR spectroscopy were completed on SS26. However, both spectra could not be analyzed beyond approximate peak locations because the peaks were too broad and offered insufficient peak resolution to determine if in fact sulfonated mPBI was synthesized.

3.7.6.2 Membrane Casting

A 5 wt% solution of SS26 was prepared in DMSO. However, this solution could not be allowed to cool to room temperature because the SS26 solution in DMSO would form a gel. Therefore, this solution was cast at 70 °C on a hot plate to ensure that it remained a liquid at all times. The result of this cast is shown in Figure 3.22. After 2 h, the membrane was severely cracked in the middle and spread towards the periphery. The cast was stopped at this point, even though the evaporation was not complete, as it was clear the experiment had failed. Another solvent was needed to facilitate the casting of a smooth, uniform membrane.

Figure 3.22: Cast of 5 wt% SS26 in DMSO at 70 °C for 2 h.

SS26 was not soluble in DMAc, NMP or DMI but SS26 was soluble in H_2SO_4. A solution containing H_2SO_4 and SS26 (5 wt%, RTMM) was made to cast SS26 into a membrane using the procedure described in chapter 2.4.4. The casting temperature of the SS26-H_2SO_4 solution was chosen 170 °C. This temperature was used as a starting point to see how quickly the solvent evaporated. The vapour pressure of H_2SO_4 at 170 °C is 0.1 kPa.[75] This is much lower than the vapour pressure of DMAc at 50 °C (10 kPa),[76] which was used in the successful casting of the PBI S26 membrane. However, the H_2SO_4 did not completely evaporate after heating the casting solution for 3 d at 170 °C. As a result, the temperature was increased to 220 °C for 2 more days. At this time, the temperature was high enough to evaporate the solvent in a timely manner. Unfortunately, the polymer had precipitated out as a powder rather than a film. It was an opaque, brown solid that appeared to be glued together by excess H_2SO_4. Therefore, H_2SO_4 was not a viable choice of solvent to cast SS26.

It was at this point that the experimentation of SS26 ceased. As a membrane could not be made from the SS26 casting solution, the focus was placed on making MEAs out of CDPS PBI and S26 membranes.

3.8 Conclusion

Many polymers were tested to see if they could be used inside the proposed TRFC as either a membrane or an ionomer/binding agent in the electrodes. Solubility in the working fluids of 1-phenyl-1-propanol and propiophenone was studied along with catalyst ink formulations using these polymers to see how electrodes could be made for the fuel cell. These electrodes were also tested in the working fluids. Membranes were also cast from these polymers so a complete MEA could be assembled.

Nafion® partially disintegrated in the presence of the working fluid (96 wt% 1-phenyl-1-propanol, 4 wt% propiophenone) at 95 °C. This is because the proticity and basicity of 1-phenyl-1-propanol are high enough to allow for some solvation of the Nafion® polymeric chains. However, the proticity and basicity of 1-phenyl-1-propanol are not strong enough to completely solvate and dissolve Nafion®. It was also found that propiophenone is unlikely to contribute to the solvation of Nafion®. Also, Nafion®-based CCGDLs were exposed to 1-phenyl-1-propanol at 130 °C for 1 h. The catalyst layer on these CCGDLs was easily removed following the abrasion of a lint-free tissue onto the surface of the CCGDL after the CCGDL was removed from the working fluid. The disintegration of the Nafion® polymeric chains in the catalyst layer is a possible explanation for its removal. PVP could not be used in a 1:1 w/w blend with Nafion® to stabilize it in the presence of the working fluids as PVP was soluble in both 1-phenyl-1-propanol and propiophenone.

Kevlar® was found to be best soluble in a DMSO/TBAF mixture (9:1 w/w) at room temperature at a concentration of 2.5 mg/mL. However, this concentration is too small for use in a catalyst ink as the catalyst particles could not be held in place by this small amount of Kevlar®. A small membrane was made from the Kevlar®-DMSO/TBAF solution by collecting a gel that had phase-separated from this solution. The gel was then dried to create a membrane. When the membrane was exposed to the working fluid (85 wt% 1-phenyl-1-propanol, 15 wt% propiophenone) at 140 °C for 21 h, the membrane lost 63% of its mass. The working fluid most likely dissolved the remainder of the DMSO and TBAF still present in the membrane. Although the membrane was too small to evaluate its strength, the leaching of DMSO and TBAF into the working fluid is of concern as any H_3PO_4-doped Kevlar® membrane will most likely leach as well. As H^+ transfer is conducted by the H_3PO_4 molecules in this membrane, the loss of H_3PO_4 would significantly lower H^+ conductivity in the membrane.

PAADP did not dissolve in the working fluids but this polymer's gel-like nature would make it difficult to work with as a PEM. Also, as the membrane is readily hygroscopic, keeping it in an anhydrous environment would be essential to ensure that the membrane remains as stable as possible. These difficulties would make working with this polymer difficult.

PAMADP was made as a copolymer with PAMAC by pouring an aqueous solution of PAMAC into an ion exchange resin (Amberlite MB-20) and then acidifying with 85 wt% H_3PO_4. The ratio of the copolymer was found to be 9:1 PAMAC/PAMADP by titration. The ion exchange of ^-OH to $H_2PO_4^-$ was assumed to be 100%. The catalyst particles in the CCGDLs that were made using a PAMAC/PAMADP-based catalyst ink did not fall off easily when the CCGDL surface was abraded with a lint-free tissue. Glycerol was used as an additive in the ink mixture to help keep the catalyst particles from agglomerating.[21] This made the ink easier to spray onto the CCGDL and also would have allowed the PAMAC/PAMADP copolymer to wrap itself more tightly around the catalyst particles. However, the

catalyst particles on the PAMAC/PAMADP-based CCGDL were not stable when the CCGDL was exposed to the working fluid (85 wt% 1-phenyl-1-propanol, 15 wt% propiophenone) at 140 °C for approximately 1 d. A membrane of PAMAC/PAMADP was also made by acidifying an aqueous solution of PAMAC/PAMADP with 1 eq of H_3PO_4 per repeating unit of the copolymer. Two parts of this membrane were exposed to pure 1-phenyl-1-propanol and propiophenone separately at 140 °C for 20 h. The striations found on the membrane before exposure were enlarged after the membrane was exposed to the 140 °C propiophenone. This indicates that the membrane absorbed the solvent and then, when the solvent was removed from the membrane, the polymer chains of PAMAC/PAMADP pushed apart from each other to enlarge the troughs of the striations. When another piece of the membrane was exposed to 1-phenyl-1-propanol at 140 °C for 20 h, the colourless membrane turned white. This may have been due to excessive 1-phenyl-1-propanol penetration in the membrane. This could cause a lack of polymeric chain organization, which would scatter the light penetrating the membrane and allow the membrane to appear white instead of transparent.

A PBI-based multilayer catalyst bed was made by using an airbrush to deposit two Vulcan XC-72 carbon layers onto the surface of a carbon paper GDL followed by the catalyst layer containing DPS PBI (mPBI) and Pt/C. This multilayer technique did not work as the bottom layer of the catalyst bed separated from the GDL. The bottom layer separated when excess heat was applied during the evaporation of the ink solvent after the final catalyst layer was sprayed into the CCGDL. However, after the CCGDL was exposed to the working fluid (85 wt 1-phenyl-1-propanol, 15 wt% propiophenone) at 140 °C for 20 h, the catalyst layer remained stable in the undamaged regions of the CCGDL. This suggests that mPBI is stable in the working fluids, even if the connection of the catalyst bed to the GDL was poor using this multilayer method.

PBI 0.8IV was received as a powder that contained mPBI and some unknown plasticizers. These plasticizers helped to create a more malleable membrane when PBI 0.8IV was cast using DMSO as the solvent. However, ink preparations that were made with PBI 0.8IV gelled after 15 s of sonication. Therefore, PBI 0.8IV could not be used in an ink because the catalyst particles need more than 15 s to disperse properly throughout the ink mixture. A H_3PO_4-doped PBI 0.8IV membrane with the plasticizers included was exposed to the working fluid (85 wt 1-phenyl-1-propanol, 15 wt% propiophenone) for 16 h at 140 °C. It was found that 69 wt% of the embedded H_3PO_4 was leached out of the membrane and into the working fluid. Significant losses in H_3PO_4 would reduce H^+ conductivity in the membrane and decrease fuel cell performance. Therefore, H_3PO_4-doped PBI 0.8IV could not be used in an MEA for the proposed TRFC.

Another mPBI product that was tested was PBI S26. PBI S26 was received as a 26 wt% solution in DMAc. CCGDLs containing PBI S26 were stable when abraded using a lint-free tissue. When PBI S26 was used in an ink mixture (2 wt% PBI S26, 10 wt% Pt/Vulcan XC-72, 5 wt% glycerol, all RTMI) using DMAc as the solvent, the ink did not gel until 90 s of sonication. However, 60 s of sonication was enough to create a finely dispersed catalyst ink. PBI S26 was cast using a 5 wt% solution of PBI S26 in DMAc at 50 °C for 4-6 h under a low argon flow in an atmosphere bag using the template shown in Figure A6. This casting method provided a uniform 40 µm thick membrane that was later used in MEA fabrication. The membrane was doped with x eq of H_3PO_4 per repeating unit of mPBI (as outlined in Table 3.12). A H_3PO_4-doped PBI S26 membrane was also exposed to propiophenone at 120 °C for 18 h. When the membrane was then taken out of the propiophenone and patted dry with a lint-free tissue, the mass of H_3PO_4 embedded inside the membrane was found to have decreased by 50 wt%. This is comparable to the mass loss of H_3PO_4 seen for PBI 0.8IV when it was exposed to the working fluid.

CDPS PBI is a cross-linked variant of mPBI. The recommended H_3PO_4 doping technique by the manufacturer proved to be insufficient to dope the membranes to 6 eq of H_3PO_4 per repeating unit of mPBI. However, the calculated H_3PO_4 doping level was artificially lower than it actually was due to the unknown mass and molecular weight of the cross-linking agent. After a H_3PO_4-doped CDPS PBI membrane was exposed to the working fluid (85 wt% 1-phenyl-1-propanol, 15 wt% propiophenone) it was calculated that the membrane had lost only 12 wt% of its total embedded H_3PO_4. Therefore, the cross-linking agent allowed the membrane to hold more of the H_3PO_4 in place. However, the leaching of H_3PO_4 into the working fluid is still significant and will reduce H^+ conductivity in the membrane.

An attempt was made to synthesize a sulfonated variant of mPBI (SS26). The synthesis of sulfonated mPBI could not be proven despite using a similar method to Peron et al., who managed to graft a sulfonic acid group onto the benzimidazole of a PBI derivative.[74] The evidence from my experiments suggested that an $mPBI^+HSO_4^-$ ion pair was made instead. A membrane of this polymer could not be cast correctly using either DMSO or H_2SO_4 as the casting solvent. When DMSO was used as the casting solvent, the membrane cracked after 2 h at 70 °C. A membrane could not be made at all when H_2SO_4 was used as the casting solvent. The polymer precipitated out of solution as a powder rather than a membrane after 3 d at 170 °C and a further 2 d at 220 °C. Therefore, this polymer could not be tested for use inside the proposed TRFC.

The PBI S26 and CDPS PBI membranes were used in the next chapter as part of MEAs that were tested inside a fuel cell using either H_2/air or H_2/propiophenone as the fuels for the fuel cell. Even though the H_3PO_4 leaching was significant into the working fluid, data could still be retrieved on how the proposed fuel cell could actually work before the MEA loses most of its H_3PO_4 content.

Chapter 4 Results: Fuel Cell Testing

4.1 MEA Fabrication

4.1.1 m-Phenylene polybenzimidazole (PBI S26)

MEAs were fabricated by hot-pressing two PBI S26-based CCGDLs (chapter 3.7.4.1) and one PBI S26 membrane (chapter 3.7.4.2). The temperature and pressure were changed to establish the effect on initial resistance, gas leaks and fuel cell performance. Table 4.1 details the fabrication results for all of the MEAs that were made using PBI S26 membranes.

Table 4.1: Components, initial resistance and fabrication conditions for PBI S26 MEAs.

MEA No.	MEA Components			Force (lbs)	Time (min)	Temperature (°C)	Resistance[d] (Ω) (25 °C)
	Anode[a]	Cathode[b]	Membrane[c]				
1	B1	A3	A	9,000	25	150	N/A
2	B2	A4	C	9,000	25	130	2.24
3	B3	A5	D	2,000	25	130	0.25
4	B4	A6	I	2,000, 5,000	25, 25	130	6.89
5	B5	A7	F	2,000	25	130	1.66
6	B8	A10	K	6,000	25	130	12.9
7	B9	A11	L	7,000	25	130	3.87
8	B10	A12	M	2,000	30	130	N/A
9	B11	A13	N	2,000	10	130	1.09
10	B12	A14	O	2,000	5	130	0.86

[a] Anode data from Table 3.11, trials B1-B12. [b] Cathode data from Table 3.11, trials A1-A14. [c] Membrane data from Table 3.12 (chapter 3.7.4.3), trials A-O. [d] Resistance was measured between the anode and cathode current collectors. The assumption was made that the measured resistance was entirely due to the MEA (wires and electrically conducting plates have negligible resistance).

The MEA fabrication method that was initially used to fabricate the PBI S26-based MEAs was detailed by Kongstein et al.[77] The conditions that they used when hot-pressing their PBI-based MEAs were 250 N/cm at 130 °C for 25 min. The pressure they recommended translates to 363 PSI. These conditions were also used by a colleague of mine to make his PBI-based MEAs.[39] A 30.25 sq. in. gold-plated copper plate (GPCP) assembly was used to hold the MEA in place while the Carver Hydraulic Unit (CHU) fused the MEA components together. The CHU that was used to hot-press the MEA measured the total pounds of force spread over the surface of the article being pressed. Therefore, the

pressure applied to the surface had to be calculated from the applied force divided by the area being pressed. It was at first assumed that the MEA was thin enough to not contribute to this hydraulic pressure calculation. In this case the calculation assumed that the MEA was effectively not present in the GPCP assembly. This would mean that the total pressure calculated would have to be 11,000 lbs over the 30.25 sq. in. GPCP assembly. If the thickness of the MEA was relevant, then only the 1 sq. in. MEA core would be relevant in calculating the total force applied to the MEA. Therefore, the total force applied to the GPCP assembly using the CHU would be 363 lbs.

However, I made two changes to the method described by Kongstein et al.[77] The first involved lowering the pressure applied to the GPCP assembly to 9,000 lbs. The second alteration made was that the temperature of the CHU was increased to 150 °C. The pressure was lowered because the author of this work was not confident that the pressure would be spread evenly over the GPCP assembly as assumed and there was a limited supply of membrane at the time. The temperature was increased to make sure that the mPBI would mold around the catalyst on the surface of the CCGDL. MEA **1** adhered to the GPCP, and could not be removed without tearing the MEA. Figure 4.1 shows the MEA before and after removal from the GPCP for MEA **1**. Figure 4.1 also shows examples of an undamaged and delaminated MEAs.

A) 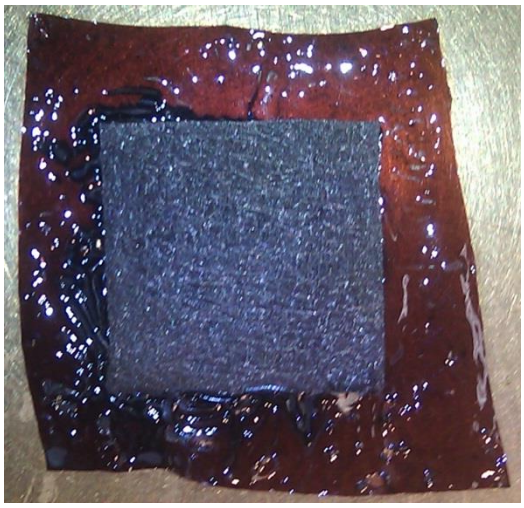 B) 

C)  D) 

Figure 4.1: A) MEA **1** before removal from the GPCP. B) MEA **1** after removal from the GPCP. C) A good example of an undamaged MEA (MEA **3**). D) Delamination of the cathode of MEA **4**.

For MEA **2**, the temperature was lowered to 130 °C as recommended by Kongstein et al.[77] The MEA did peel off the GPCP without any problems. However, when a fuel cell was constructed with this MEA (chapter 2.6.1) the gas leak test showed that there was a crossover of gas between the two sides of the MEA. No amount of rearrangement of the gaskets inside the fuel cell assembly could fix the

problem. There were no visible holes seen around the peripheral membrane of the MEA. However, that does not mean there were no holes in the membrane that was sandwiched between the porous electrodes. MEAs are fragile and can be perforated easily, even during fuel cell operation.[24] This occurs because MEAs are often exposed to major stressors like temperature and pressure changes during the operation of the fuel cell.[24]

After the testing for MEA **2** was completed, it was discovered that the assumption made for the distribution of pressure was incorrect.[39] The pressure applied to the MEAs using the CHU was determined to have far exceeded the amount prescribed by Kongstein et al.[39,77] The pressure exerted by the CHU was found to only apply to the MEA and not the GPCP assembly as a whole.[39] Therefore, the pressure exerted by the CHU would have to be reduced to 363 lbs to account for the 1 sq. in. area of the MEA. Unfortunately, the lowest pressure the CHU could achieve was 2,000 lbs. Therefore, all hot-pressed MEAs would be pressed with 2,000 lbs of pressure as the required equipment for pressing the MEA at 363 lbs of pressure at 130 °C was unavailable.

For MEA **3**, lowering the applied pressure from the CHU to 2,000 lbs produced an MEA that was fused together and easy to remove from the GPCP with a spatula. Upon further examination, it was clear that there were no leaks in the gas test when the MEA was inside the fuel cell assembly. Unfortunately, this was not an entirely reproducible result. The components of MEA **4** would not stick together after 25 min at 130 °C with 2,000 lbs of pressure. Therefore, the components of MEA **4** were placed back into the GPCP assembly, which was placed inside the CHU at a new pressure of 5,000 lbs for 25 min. After MEA **4** had been removed from the GPCP assembly, it was found that the MEA had delaminated at the cathode. The delamination of the cathode on MEA **4** is shown in Figure 4.1D. It appeared as though the catalyst bed was cut in half, with some of the catalyst bed embedded into the membrane and some of the catalyst bed on the CCGDL. This result was replicated by MEA **5**, but it was achieved after the MEA

had been subjected to 2,000 lbs of pressure at 130 °C for 25 min. Delamination between the catalyst and the membrane significantly increases the ohmic resistance of the MEA in a non-linear manner,[78] which in turn reduces the power output of the fuel cell. MEAs **6** and **7** suffered from high resistance levels due to the high pressure exerted by the CHU on the MEA during the MEA fabrication process. This high pressure could have pressed the H_3PO_4 out of the MEA causing the high resistance levels within the MEA.

It was thought that maybe the time these MEAs spent in the CHU was incorrect. Therefore, MEAs **8**-**10** were kept at 2,000 lbs of pressure at 130 °C but were hot-pressed for different times. However, this procedure resulted in MEA **8** being hot-pressed for an excessive period of time. The result caused MEA **8** to become damaged when removed from the GPCP. In contrast, MEAs **9** and **10** were peeled off the GPCP with ease and contained no visible holes. The lower amount of time spent inside the CHU prevented excessive adhesion to the GPCP, and therefore, prevented damage to MEAs **9** and **10** when they were removed from the GPCP. The ohmic resistances for both MEAs **9** and **10** were low compared to the many of the other MEAs.

Ohmic resistances are important in determining the performance of the MEA in a fuel cell. High resistances are caused by a lack of contact between the catalyst and the electrolyte.[78] If the electrolyte is not in sufficient contact with the catalyst due to an improper connection between the catalyst and membrane then the ohmic resistance will increase. The lower the resistance of the MEA, the better it should perform in a fuel cell. The resistance of the fuel cell at room temperature was only used as a relative measure of H^+ conductivity to other MEAs. Under the higher operating temperatures of the fuel cell the resistance of the fuel cell is more relevant than at room temperature. This is because at the operating temperature of the fuel cell a current is expected to be drawn. The resistances of all MEAs

were found to be much lower at higher temperatures when inside a fuel cell than at room temperature. This effect is also seen in the literature for PBI-based PEMFCs.[79]

4.1.2 Cross linked m-phenylene polybenzimidazole (CDPS PBI)

There were three different MEAs made with the CDPS PBI membrane. However, the electrodes contained in these MEAs used the same catalysts seen in chapter 4.1.1 but with higher catalyst loadings (40 wt% Pd or Pt on Vulcan XC-72 instead of 20 wt% Pd or Pt on Vulcan XC-72). The same PBI S26 binder was used in the catalyst ink for the CDPS PBI MEAs because CDPS PBI could not be dissolved in a solvent. Table 4.2 shows the results for the CDPS PBI MEAs.

Table 4.2: Components, initial resistance and fabrication conditions for CDPS PBI MEAs.

MEA No.	Metal Loading on CCM (mg metal/cm^2)		H_3PO_4 Doping Level (eq)[c]	Pressure (lbs)	Time (min)	Temperature (°C)	Resistance (Ω) (25 °C)
	Anode[a]	Cathode[b]					
11	0.32	0.30	0.8	2,000	2	130	0.35
12	0.37	0.20	1.7	2,000	2	130	0.34
13	0.50	0.63	3.2	2,000	2	130	1.46

[a] The anode catalyst is Pt/Vulcan XC-72. [b] The cathode catalyst for MEAs **11** and **12** are Pd/Vulcan XC-72, MEA **13** is Pt/XC-72. [c] Number of equivalents of H_3PO_4 per repeating unit of mPBI. Data taken from Table 3.14.

The hot-pressing procedure was altered to try and reduce the actual pressure felt by the MEA. A CDPS PBI CCM was placed between two GDLs, two Teflon® gaskets and two flow field plates. This procedure is described in the last paragraph of chapter 2.5.5. The flow plate assembly was then placed inside the CHU for hot-pressing. After the flow plate assembly was removed from the CHU it was cooled to room temperature and then bolted together with the endplates and current collectors to create a fuel cell. Judging by the low resistance levels measured on these fuel cells, this new hot-pressing method performed successfully. The flow field plates are 7.5 cm x 7.5 cm in area. Therefore, the area that the CHU pressed on was 56.25 cm^2 or 8.72 sq. in. Assuming the gaskets had leveled the pressure across the MEA and both of the flow field plates, the pressure felt by the flow field assembly was calculated to be 229 PSI.

The hot-pressing time was reduced to 2 min by suggestion from a colleague. This would reduce the amount of damage that was being done to the MEAs caused by exposing them to high pressures for long periods of time. There was a balance that had to be struck between creating a good connection between the electrodes and the membrane versus creating holes in the membrane or squeezing out H_3PO_4 from the MEA. The low resistance levels of MEAs **11** to **13** compared to many of the others shown in Table 4.1 suggested that the hot-pressing conditions were sufficient.

4.2 Scanning electron microscopy of a CDPS PBI MEA

Scanning electron microscopy with energy dispersive x-ray spectroscopy (SEM-EDS) was utilized on MEA **12** to observe the mapping of P, Pt, and Pd on the surface of the catalyst bed. SEM backscattered electron imaging (SEM-BEI) was used to highlight where the heavier elements are on the

surface of the catalyst bed with increasing brightness in areas containing heavier elements, whilst also showing topography. SEM-BEI would also show how large the polymer regions and catalyst agglomerations are. Secondary electron emission SEM images were also taken to show just the topography. Figure 4.2 shows these SEM and SEM-EDS micrographs for the cathode of MEA **12**. Figure 4.2A shows that there is a small amount of palladium measured across the entire mapping surface of the images shown in Figures 4.2B and C, along with a small amount of phosphorus in the form of H_3PO_4. It is small because a lot of the area shown in Figures 4.2B-C is the carbon tape that was used to host the sample. The characters K and L that are listed next to each element in Figure 4.2A represent the principal quantum number for an electron that was released from an atom to the x-ray detector. The K and L bands shown in Figure 4.2A represent detected electrons from the first and second shells of each element, respectively. The carbon tape is shown as black in colour in Figures 4.2B-D. Figures 4.2B and 4.2C also show a significant amount of palladium and phosphorus within the structure that is shown in more detail in Figure 4.2D. As phosphorus is isolated to this structure, it is suggested that this piece is a mass of mPBI film containing agglomerations of Pd/Vulcan XC-72. Alternatively, the mass at the centre of the images shown in Figures 4.2B and 4.2C could be carbon rods covered by a large amount of H_3PO_4 or palladium. The carbon rods at the bottom of Figure 4.2D appear to host palladium particles on their surface according to Figure 4.2C. There is very little H_3PO_4 present on these rods according to Figure 4.2B. In the SEM-EDS image maps the dark areas are where the mapped elements are not seen. Therefore, the images of Figure 4.2 tell us that both H_3PO_4 and palladium catalyst are present throughout the sample but visual evidence of the polymer is not seen in these images.

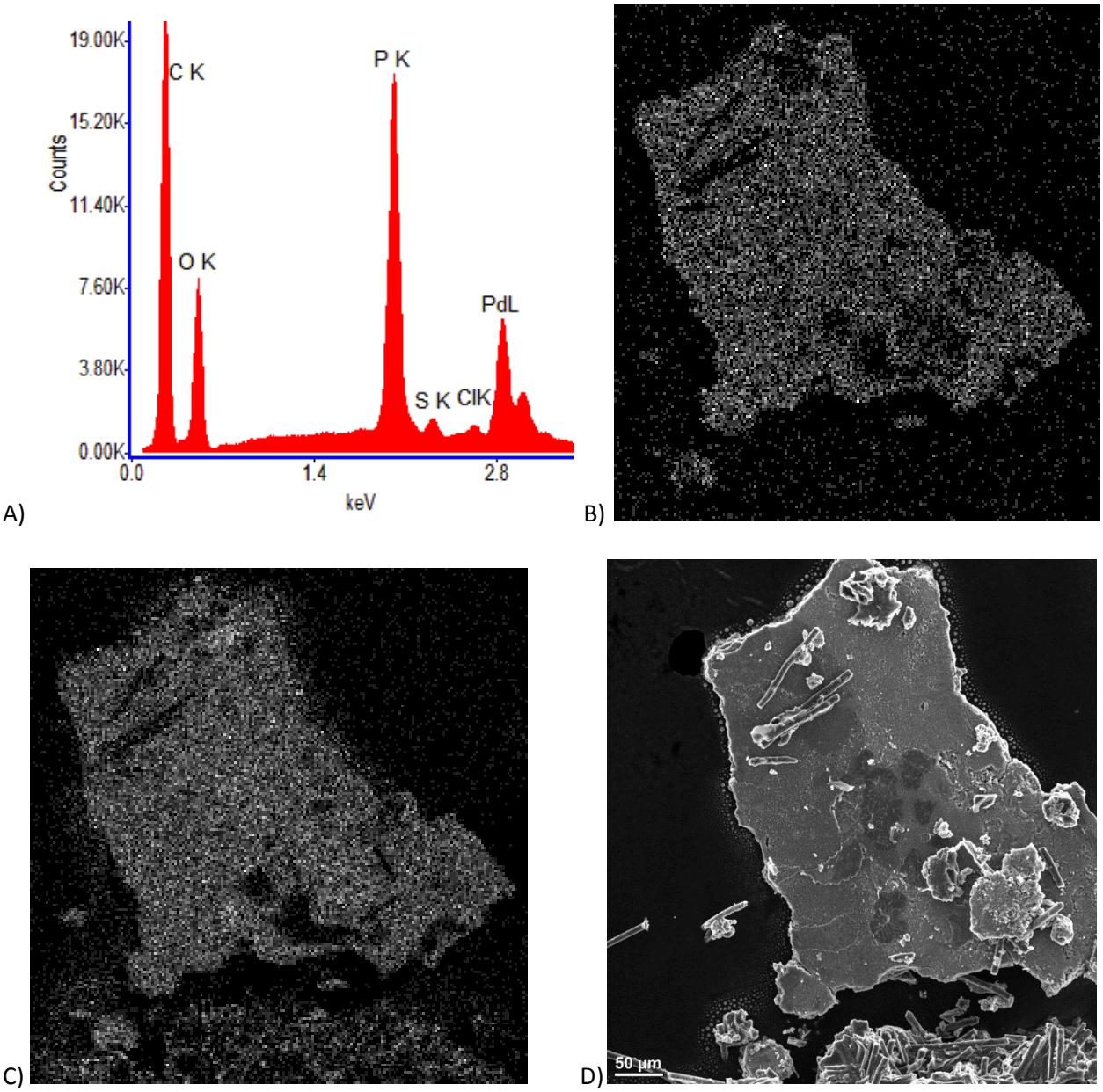

Figure 4.2: SEM-EDS and SEM micrographs of the MEA **12** cathode surface. The amount of each element present in the area represented by images B-D are shown in A. B-D shows the same article with all of the images using the same 50 µm scale shown in D. B and C show elemental mapping of phosphorus and palladium, respectively. Bright areas for B and C indicate increased signal for the mapped element. A secondary electron SEM image of the same area is shown in D.

Figure 4.3B shows some carbon rods from the carbon paper (GDL) and what appears to be an image of an mPBI film (highlighted by the orange circle). Figure 4.3C shows an image captured by SEM-BEI, which is of the same area shown in Figure 4.3B. SEM-BEI shows the presence of elements based on each element's mass. Carbon is a light element and will appear black versus the heavier elements like platnium, which will appear white. However, the surrounding topography is soaked in H_3PO_4 so the determination between palladium and H_3PO_4-doped mPBI (depicted by phosphorus detection) is difficult. This is because the brightness levels appear to be approximately the same for both phosphorus and palladium in Figure 4.3C. The rods are from the carbon paper GDL. The area indicated by the orange circle looks different from the surrounding area. This area looks like it contains a film rather than particle agglomerations, indicating the presence of mBPI. It can also be said that this film contains H_3PO_4-doped within the mBPI as the area appears bright in the SEM-BEI image shown in Figure 4.3C. The SEM-EDS map confirms the presence of both phosphorus and palladium in the sample. The EDS spectrum shown in Figure 4.3A also shows that chlorine is present in the observed sample. The chlorine came from LiCl that was used in the ink deposition procedure. The peaks in the spectrum can only show the presence of an element and not its association or bonding with another. However, it is possible that chlorine may have adsorbed to the surface of palladium during the preparation of the electrodes and thus deactivated these catalyst sites. Chlorine is also present in the EDS spectra shown in Figures 4.2A.

A)

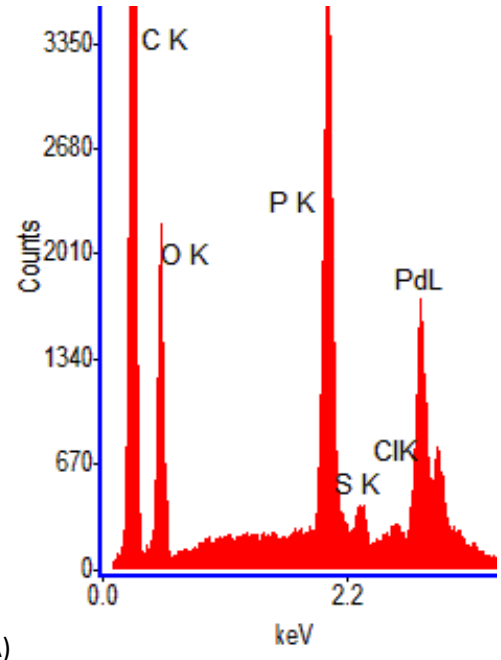

B)

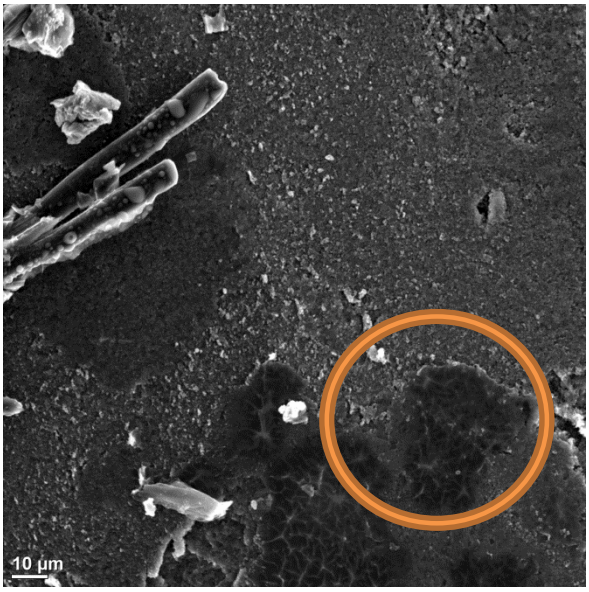

C)

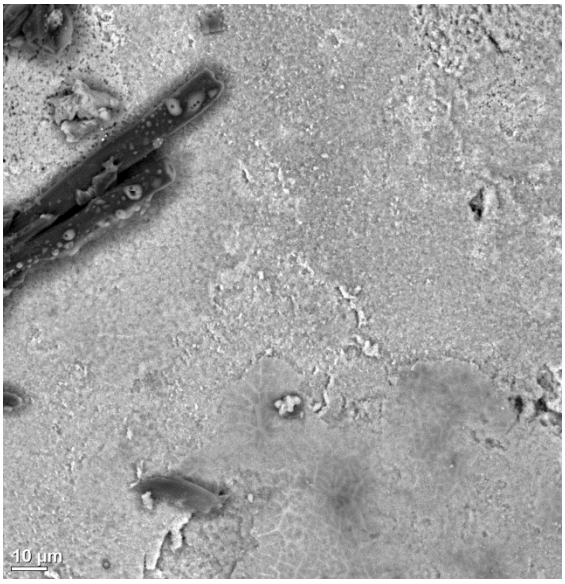

Figure 4.3: SEM-EDS spectrum (A), SEM-EDS (B) and SEM-BEI (C) micrographs of the cathode surface of MEA **12**. The elements present in the area represented by images B and C are shown in the SEM-EDS plot shown in A. B and C show a magnified version of the same large structure shown in Figure 4.2D. The bright shades in Figure 4.3C show the location of phosphorus and palladium, whilst the dark shades show the location of carbon. B is an overlay of both phosphorus and palladium maps.

There are similar images available for the anode of MEA **12**. Figure 4.4 shows a SEM-EDS spectrum and maps of the anode of MEA **12**. The peaks for phosphorus and platinum overlap but both are still present in the spectrum shown in Figure 4.4A. Both maps seen in Figures 4.4C and 4.4D show the location of both platinum and phosphorus. Both elements appear uniformly spread around the carbon rods in the same areas. Figure 4.4B shows the location of carbon within the same area. The large substance between the rods in the top right corner of Figure 4.4B could be where the mPBI polymer is located. However, this area seems to be absent of both platinum and phosphorus. There are several other areas within these images that share the same relationship. This suggests that there are large areas in the electrode where mPBI was not doped with H_3PO_4 and where mPBI was not uniformly distributed with platinum catalyst during the deposition of the catalyst bed. These large regions of polymer would hinder the performance of the electrode in a fuel cell as it is a non-operational material. These areas reduce the catalyst loading with respect to the area of the electrode. However, there are some small spots of polymer seen on the rods in Figure 4.4B that are illuminated in the phosphorus and platinum maps suggesting that there are some areas where mPBI is doped with both platinum catalyst and H_3PO_4. This would be conducive to allow catalytically active areas to produce H^+, which can transport through the electrode and into the membrane. Fortunately, chlorine could not be found on the surface of the anode using SEM-EDS, which could be because of the ion repulsion caused by the negatively charged anode when using the fuel cell containing this MEA.

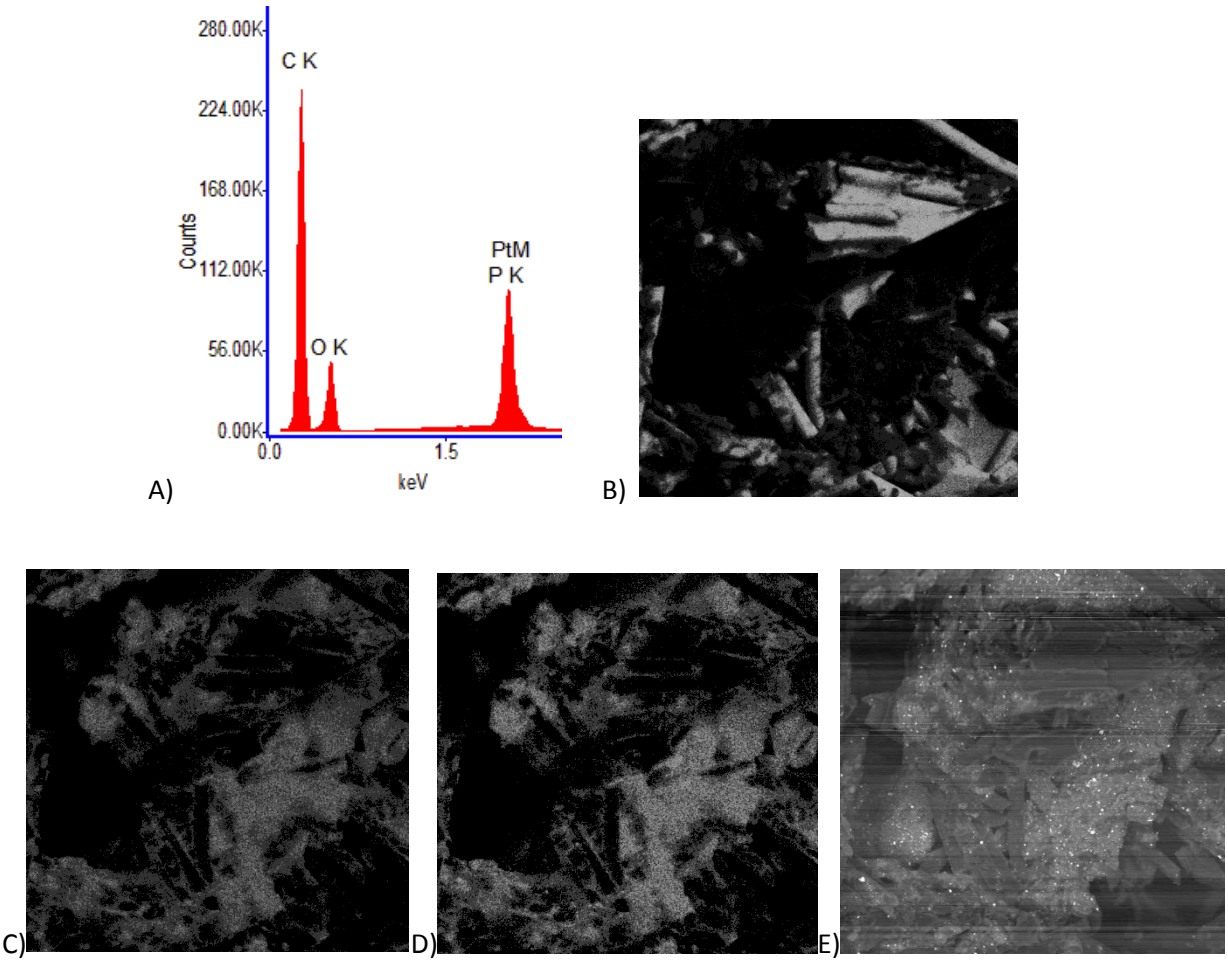

Figure 4.4: SEM-EDS maps and spectrum of the MEA **12** anode. B, C and D show an SEM-EDS map of carbon, phosphorus and platinum, respectively. The elements present in the area represented by images B, C and D are shown in A. The secondary electron SEM micrograph of the area detailed in B, C, and D is shown in E.

Figure 4.5 shows a SEM-BEI micrograph of the MEA **12** anode. The micrograph shows agglomerations of platinum (white) scattered between the slightly lighter areas of the mPBI, which is highlighted due to the phosphorus signal from H_3PO_4. The rods that are shown in the micrograph are from the carbon paper and appear darker than the other materials shown in the image as carbon atoms

have less mass than the other elements present in the sample. Figure 4.5 clearly shows the presence of both mPBI, platinum catalyst and H_3PO_4 in contact with each other and the electrically conducting carbon rods. Therefore, there are areas in this electrode that should allow for catalytic activity and active H^+ conduction through the electrode.

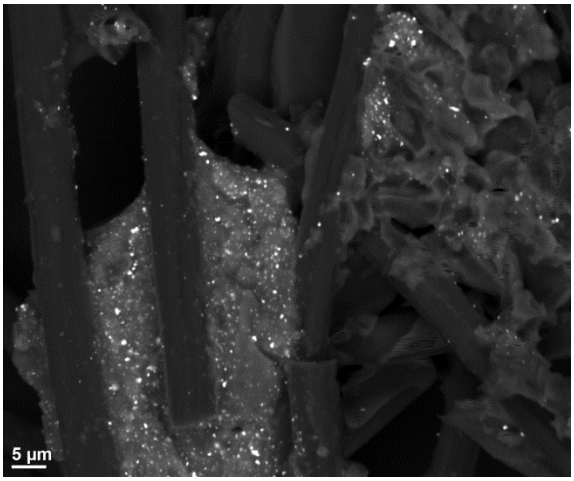

Figure 4.5: An SEM-BEI micrograph of the MEA **12** anode. The brightest areas of the image represent platinum with the next brightest being phosphorus. The darkest grey is carbon.

All of the images seen in this chapter show the interaction between the mPBI binder, the H_3PO_4 electrolyte and the catalyst. There are many areas where the mPBI microfilms are too large, which would reduce catalyst availability during fuel cell operation. However, the three phase boundary between the catalyst, H_3PO_4-doped mPBI and the open atmosphere cannot be seen at this resolution. The following section displays two transmission electron microscopy (TEM) images of the cathode as an attempt to show this three phase boundary.

4.3 Transmission electron microscopy (TEM) of a CDPS PBI MEA

Figure 4.6 shows TEM micrographs of the MEA **12** cathode catalyst bed. The orange circle in Figure 4.6A details several catalyst agglomerations that are in contact with the electrolyte in the mPBI, the supporting carbon and the atmosphere. This is the three phase boundary. Figure 4.6B likely shows this boundary as well with the catalyst agglomerations that are shown, but the viewing angle does not show this boundary directly. It is also possible that some of these catalyst agglomerations are embedded entirely into the mPBI, rendering the catalyst catalytically inactive in a H_2/O_2 PEMFC.

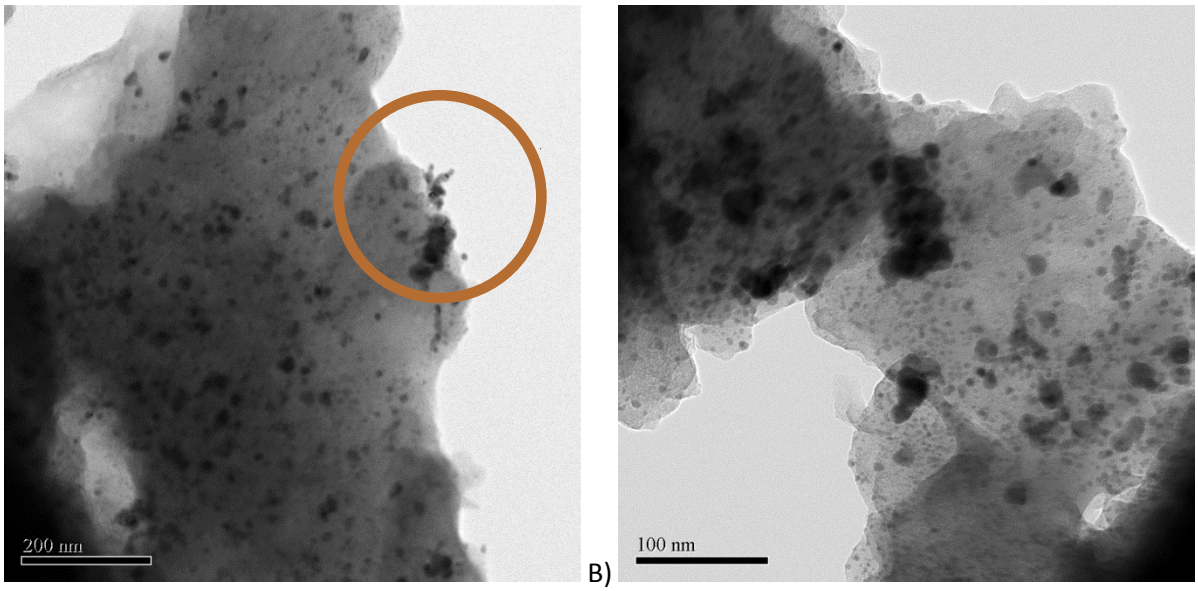

Figure 4.6: TEM micrographs of a sample of the MEA **12** cathode. Both images show catalyst on supported carbon agglomerations (black) attached to or embedded in H_3PO_4-doped mPBI (grey).

4.4 H_2/air fuel cell operation

All MEAs detailed in Tables 4.1 and 4.2 except MEAs **1** and **8** were assembled into a fuel cell. MEA **3** was the first MEA that was of good enough quality (no gas crossover, and low initial resistance) to put inside a fuel cell assembly for fuel cell testing. Figure 4.7 shows the polarization curve for MEA **3** for the H_2/air fed fuel cell test. The polarization and power density curves seen in Figure 4.7 show an increase in performance of the fuel cell with temperature until 160 ° C. The best peformance was seen at 140 °C where the maximum power density was approximately 0.19 W/cm^2. Mader et al. showed a H_3PO_4-doped mPBI PEMFC with 1.0 mg/cm^2 Pt loading in the electrodes (30% Pt on carbon) achieving 0.40 W/cm^2 at 140 °C.[33] The open circuit voltage (OCV) of the fuel cell containing MEA **3** measured 0.57 V, which is comparably lower than the results showcased Mader et al.[33] They reported that a H_3PO_4-doped mPBI PEMFC should have an OCV of roughly 0.8 V when fed with H_2/air.[33] This is to be compared to the theoretical maximum OCV of 1.23 V for a H_2/O_2 PEMFC.[6,80] The low OCV value for MEA 3 could be due to H_2/air crossover caused by very small holes in the MEA. This crossover of fuel would create mixed potentials at the cathode that would act to reduce the OCV.[80] Mixed potentials are caused by the normal oxygen reduction reaction at the cathode and the oxidation of Pt to an oxide or the oxidation of impurities at the anode.[80]

Table 4.3 shows the maximum OCV at room temperature and the results of the H_2/air fuel cell test for each MEA. Figure 4.7 shows the only stable MEA out of the 13 that were made for the H_2/air fed PEMFC. None of the others could reach the power output that was shown in Figure 4.7. It is unclear why the power output could not be matched for all of the other MEAs. None of the MEAs that were tested under H_2 and air in a fuel cell test station, except MEA **3**, could sustain a load exceeding 0.2 A

(0.04 A/cm^2) before the voltage fell to zero. Most could not handle any more than 0.1 A (0.02 A/cm^2). Figure 4.8 shows the typical polarization and power density curves for MEAs **5-7**, **9-13**, showing specifically MEA **12**. The maximum current draw that Kongstein et al. report for a mPBI PEMFC running at 150 °C is 2.2 A/cm^2 at 0.45 V.[77] This is far higher than the load capabilities found in this work for MEAs **3**, **5-7**, **9-13**. The mPBI-based MEA that Kongstein et al. made contained Pt loadings of 0.6 mg/cm^2 on the cathode and 0.4 mg/cm^2 on the anode.[7] These loadings are similar to the ~0.5 mg/cm^2 of Pd/Vulcan XC-72 on the cathode and ~0.5 mg/cm^2 Pt/Vulcan XC-72 on the anode that are present in MEAs **1-13**. However, the performance of MEAs **3**, **5-7**, **9-13** cannot match the performance that Kongstein and Mader et al. have detailed.[33,77]

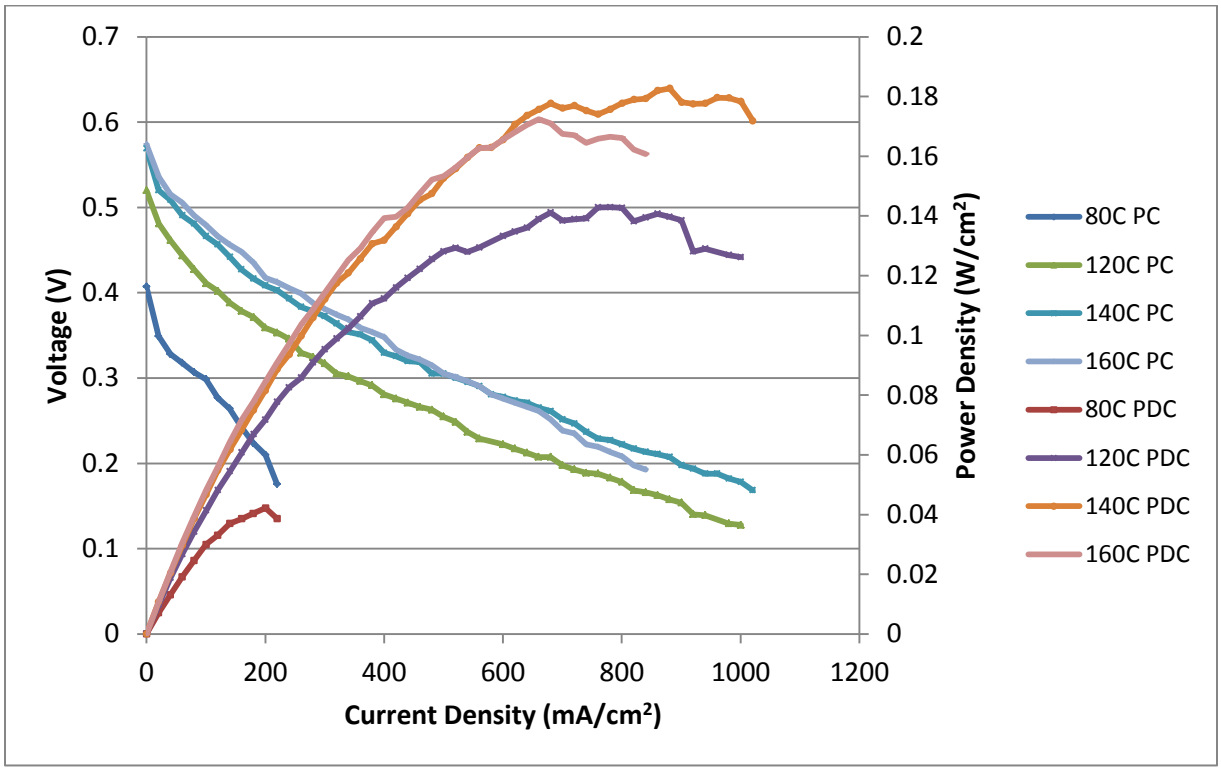

Figure 4.7: The H_2/air fed fuel cell polarization and power density curves for MEA **3** at differing temperatures. PC = polarization curve, and PDC = power density curve.

Table 4.3: The maximum OCV at room temperature for PBI S26 and CDPS PBI-based MEAs and the results of the H_2/air fuel cell test using these MEAs.

MEA No.	OCV* (V)	Notes
1	N/A	Holes visible in the MEA.
2	N/A	Gas leak when the MEA was in the fuel cell assembly.
3	0.360	Described in Figure 4.7.*
4	N/A	Gas leak when the MEA was in the fuel cell assembly.
5	0.593	No voltage was seen after 40 mA/cm^2 current density applied.*
6	0.574	The OCV declined to 0.320 V, at 115 °C. H_3PO_4 had leaked between the gaskets (observed after the fuel cell assembly was opened).** No load was applied
7	0.210 V	The OCV rapidly decreased after fuel cell temperature >60 °C. No voltage seen after 20 mA/cm^2 load at 110 °C.**
8	N/A	Holes observed in MEA.
9	0.159 V	The fuel cell leaked with 0.07 mm Teflon® gaskets but did not leak with reinforced silicone 0.15 mm gaskets. The OCV increased to 0.281 V at 60 °C, and then declined to 0.222 V at 140 °C. The cell couldn't handle a current load of 20 mA/cm^2. When the fuel cell was conditioned, the OCV increased to 0.566 V at 140 °C. After conditioning, the fuel cell still couldn't handle 20 mA/cm^2 load.
10	0.320 V	The OCV declined to 0.164 V at 60 °C, then recovered steadily up to 0.515 V at 160 °C. The fuel cell still couldn't handle a current density beyond 20 mA/cm^2.*
11	0.350 V	The maximum current density was 12 mA/cm^2 at 0 V at 140 °C.
12	0.310 V	The OCV continually increased to 0.489 V at 140 °C. I managed to get a non-zero voltage up to 23 mA/cm^2 applied load.
13	N/A	The surface of the MEA electrodes were crinkled from localized overheating when doping with H_3PO_4 at 80 °C. I did not run the fuel cell with H_2/air.

* Silicone gaskets (0.15 mm thick, each). ** Teflon® gaskets (0.07 mm thick, each). MEAs **3**, **5-7**, **9**, **10** were tested on the Hydrogenics G60. MEAs **11-13** were tested on the custom Autolab test station.

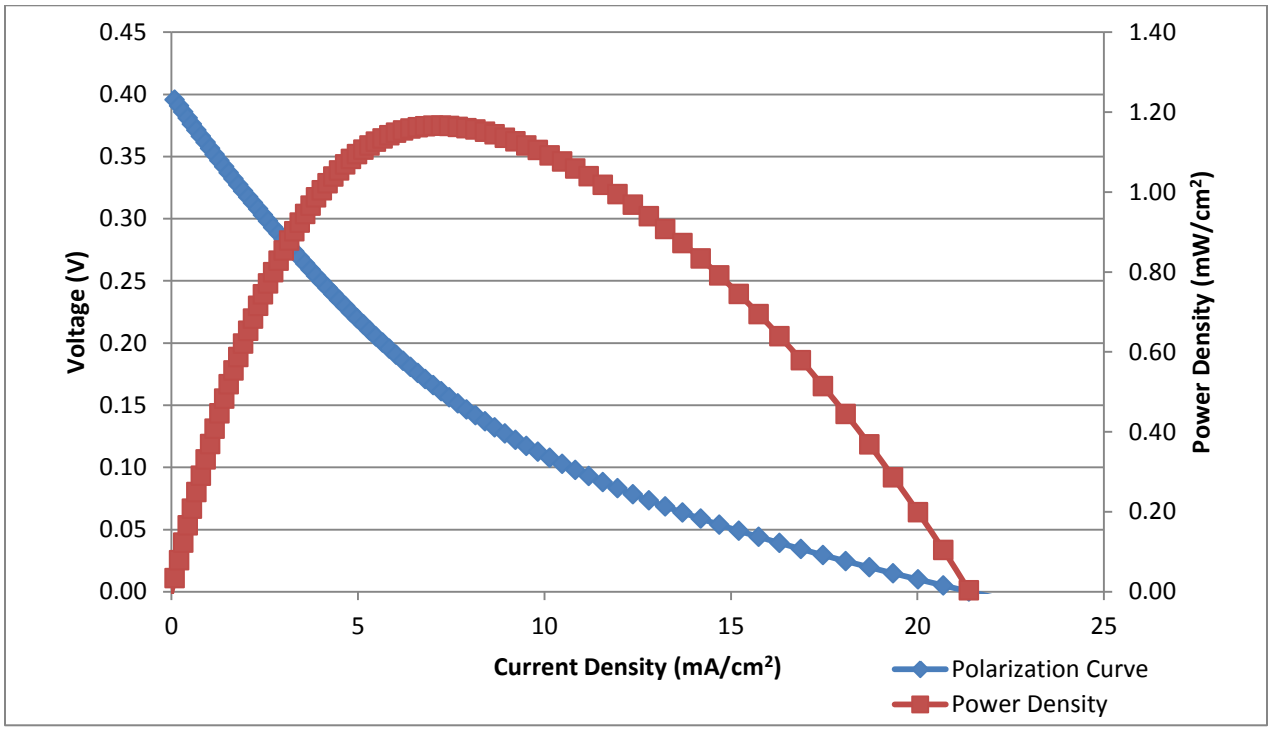

Figure 4.8: H_2/air fed H_3PO_4-doped mPBI-based PEMFC polarization and power density curve for MEA **12**.

The SEM micrographs mentioned in chapter 4.2 may be able to explain why the fuel cell performance of MEAs made in this work were not as good as those shown in the literature.[33,77] The SEM micrographs for MEA **12** show the H_3PO_4-doped mPBI in large as well as small films measuring up to several microns across. The larger films would hinder the diffusivity of H_2 and O_2 through the catalyst bed as well as minimize the contact of the film with the catalyst. Poor H_2/O_2 diffusivity would introduce mass transport losses, which would prematurely cut the performance of the fuel cell by under-utilizing the catalyst surface. The reduced performance could also be due to adsorption of $H_2PO_4^-$, which could slow the oxygen reduction reaction (ORR) considerably.[81]

Electrochemical impedance spectroscopy (EIS) was conducted on MEAs **11** and **12** whilst they were in the fuel cell assembly (separately) under H_2/air gas flow at 140 °C. The EI spectra are shown in Figures 4.9 and 4.10, respectively. Both figures show that the ohmic resistances of MEAs **11** and **12** are 0.12 Ω and 1.0 Ω, respectively, at 140 °C. The one band shown in both Figures represents the impedance response of the cathode.[82] The anode impedance is negligible and therefore does not show due to the facile reaction kinetics of the hydrogen oxidation reaction (HOR).[6,82] The relatively high impedance for MEA **11**, compared to MEA **12**, would suggest that the diffusion rate of air into the cathode catalyst bed is slower for MEA **11**.[82] It may also be that the Pd catalyst on MEA **11** had been deactivated by $H_2PO_4^-$ or by an impurity present in the catalyst bed.[81]

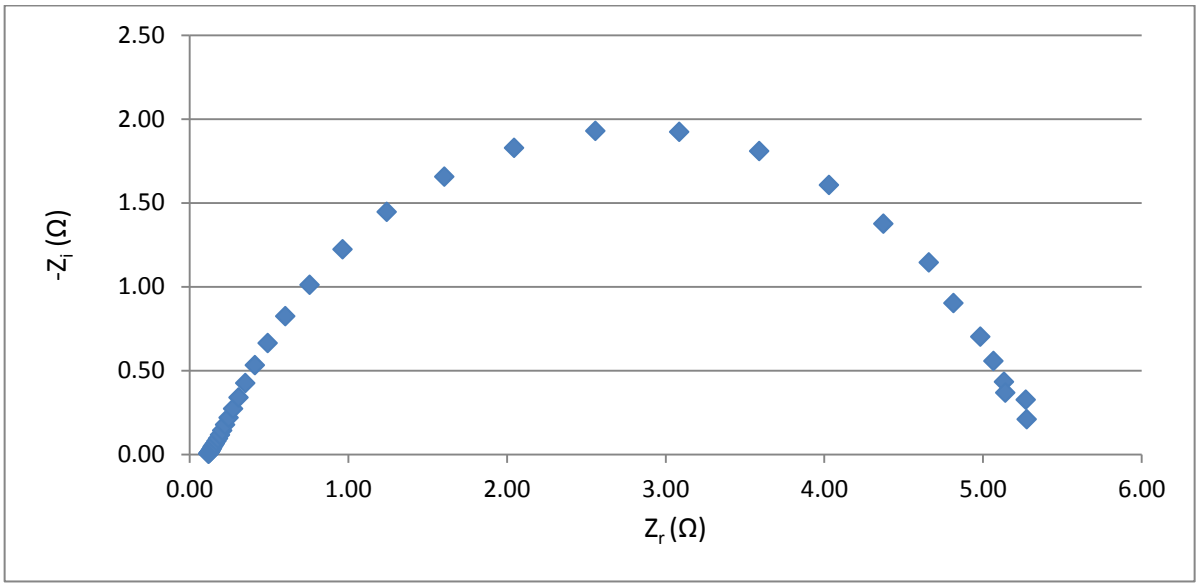

Figure 4.9: Nyquist plot showing the EI spectrum for MEA **11** at 140 °C. The frequency range was between 50,000-0.01 Hz. The EI spectrum was measured at 0 V and 23 mA/cm^2.

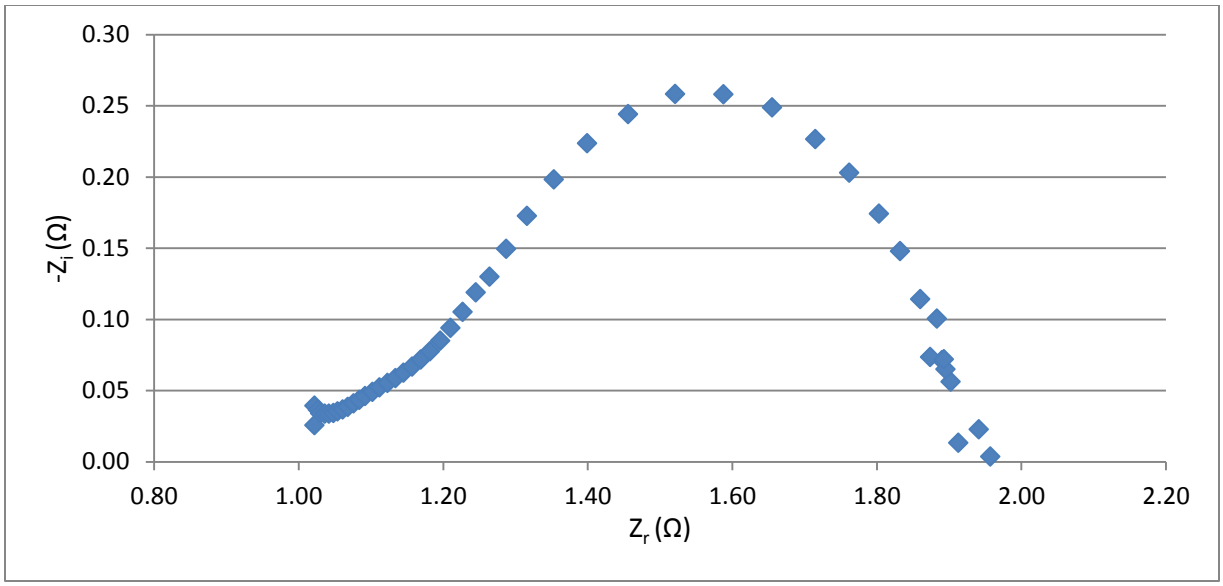

Figure 4.10: Nyquist plot showing the EIS curve for MEA **12** at 140 °C. The frequency range was between 50,000-0.01 Hz. The EI spectrum was measured at 0.08 V and 1.2 mA/cm^2.

4.5 H_2/propiophenone fuel cell operation

Some of the MEAs (**3**, **11** and **12**) that were tested in the H_2/air fed fuel cell setup were now tested with H_2 and propiophenone as the feed fuels for the fuel cell. This test is analogous to the proposed TRFC system but uses 100% propiophenone instead of a 46/54 w/w mixture of 1-phenyl-1-propanol and propiophenone, respectively. The 46/54 w/w ratio for 1-phenyl-1-propanol and propiophenone was calculated to be the equilibrium point for the dehydrogenation reaction of 1-phenyl-1-propanol at 200 °C in the dehydrogenation reaction chamber.[11] Using 100% propiophenone would give the fuel cell the best chance for propiophenone to undergo the reduction reaction to 1-phenyl-1-propanol as there would be no 1-phenyl-1-propanol to initially dilute the propiophenone

feed. If the fuel cell can be proven to work using exclusively H_2 and propiophenone as the oxidant and reductant fuels for this fuel cell, respecively, then it can be said that the proposed TRFC concept works. MEA **3** was tested on the Hydrogenics G60 fuel cell test station and MEAs **11** and **12** were tested on the custom fuel cell test station containing the Autolab potentiostat.

The polarization and power density curves for the H_2/propiophenone fed, H_3PO_4-doped mPBI-based MEAs (**3** and **11**) are shown in Figures 4.11 (**3**) and 4.12 (**11**), respectively. MEA **3** performed well in comparison to MEA **11** but the modified Hydrogenics G60 fuel cell testing station that was used (shown in chapter 2.6.3, Figure 2.6) was not degassed to eliminate the residual air in the propiophenone or the tubing. Therefore, most of the performance associated with MEA **3** was probably due to the presence of O_2. The theoretical maximum voltage for propiophenone hydrogenation on Pd/Vulcan XC-72 is 61.5 mV. The theoretical maximum voltage for ORR is 1.23 V.[6] Therefore, the presence of O_2 will make the fuel cell appear to perform better than it should when measuring the fuel cell's polarization curve. As the propiophenone was cycled through the fuel cell and back into the reactor, the O_2 dissolved in 200 g of propiophenone has to be taken into account. Although solubility data is unavailable for O_2 in propiophenone, the mole fraction of O_2 in propyl benzene (a close relative) is 1.35×10^{-3} at 298.15 K and 101.325 KPa.[83] Many other organic compounds that are listed as similar to propyl benzene are within one order of magnitude for O_2 solubility.[83] Therefore, there would be approximately 2×10^{-3} mol of O_2 present in 200 g of propiophenone. The amount of O_2 available would be enough to consume 8×10^{-3} mol of electrons or sustain 0.15 A/cm^2 for the duration of the 1050 s test, which is far more current than is seen in Figure 4.11. Therefore, it is more likely that the true performance of the H_2/propiophenone fed, H_3PO_4-doped mPBI PEMFC is seen in Figure 4.12. For MEAs **11-13**, N_2 was bubbled into the propiophenone reservoir to eliminate any O_2 dissolved in the propiophenone. The propiophenone was pumped into and out of the fuel cell for 30 s to remove any air in the tubing and the fuel cell.

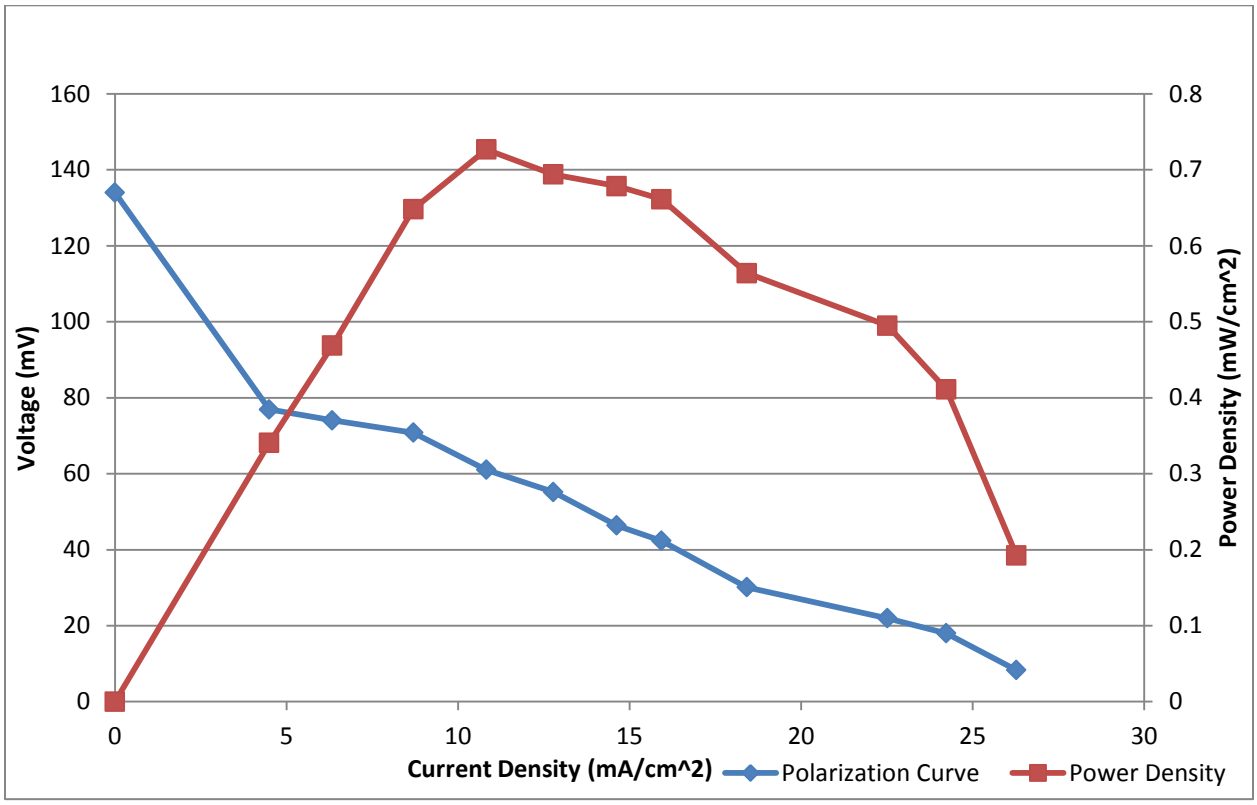

Figure 4.11: The polarization and power density curves for the H_2/propiophenone fed, H_3PO_4-doped mPBI-based MEA **3**. The temperature of the fuel cell was 140 °C.

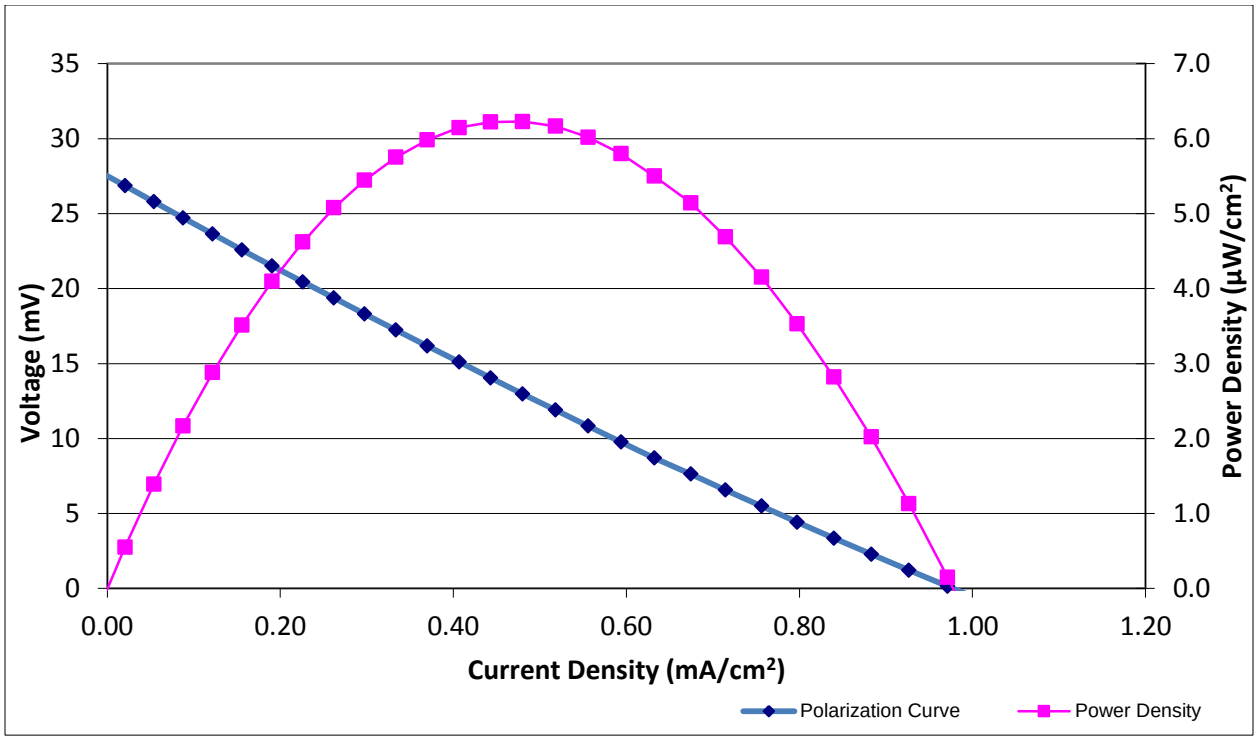

Figure 4.12: The polarization and power density curves for the H_2/propiophenone fed, H_3PO_4-doped mPBI-based MEA**11**. The temperature of the fuel cell was 140 °C. The propiophenone was degassed prior to collecting this data.

Ando et al. mangaged to achieve a current density of up to 20 mA/cm^2 for their acetone/isopropanol TRFC system.[12] Unfortunately, the analogous setup for the proposed TRFC in this work using H_2 and propiophenone could not compare with Ando's system.[12] The maximum current density output of MEA **11** is an order of magnitude less than Ando's optimized system.[12] The previous work of Ando et al. found that an unoptimized version of the acetone/isopropanol TRFC system could yield a maximum power density of approximately 175 µW/cm^2.[7] This is 30 times better than what was achieved with MEA **11**. This may be because a lot of the catalyst surface may have been deactivated by the presence of adsorbed Cl^- and $H_2PO_4^-$ as indicated by the poor H_2/air-fed fuel cell performance.

Another possiblity could be that the electrochemical reduction of propiophenone is too slow to produce a power density similar to Ando's system.

The polarization and power density curves for MEA **12** could not be completed correctly (Figure 4.13). The measured current appeared to be random as the potential was decreased from 27 mV to 0 mV. The current density ranged from 2.75 mA/cm^2 to 1.15 mA/cm^2. It is not known why the Autolab potentiostat could not keep a stable reading of the current as the potentials were decreased.

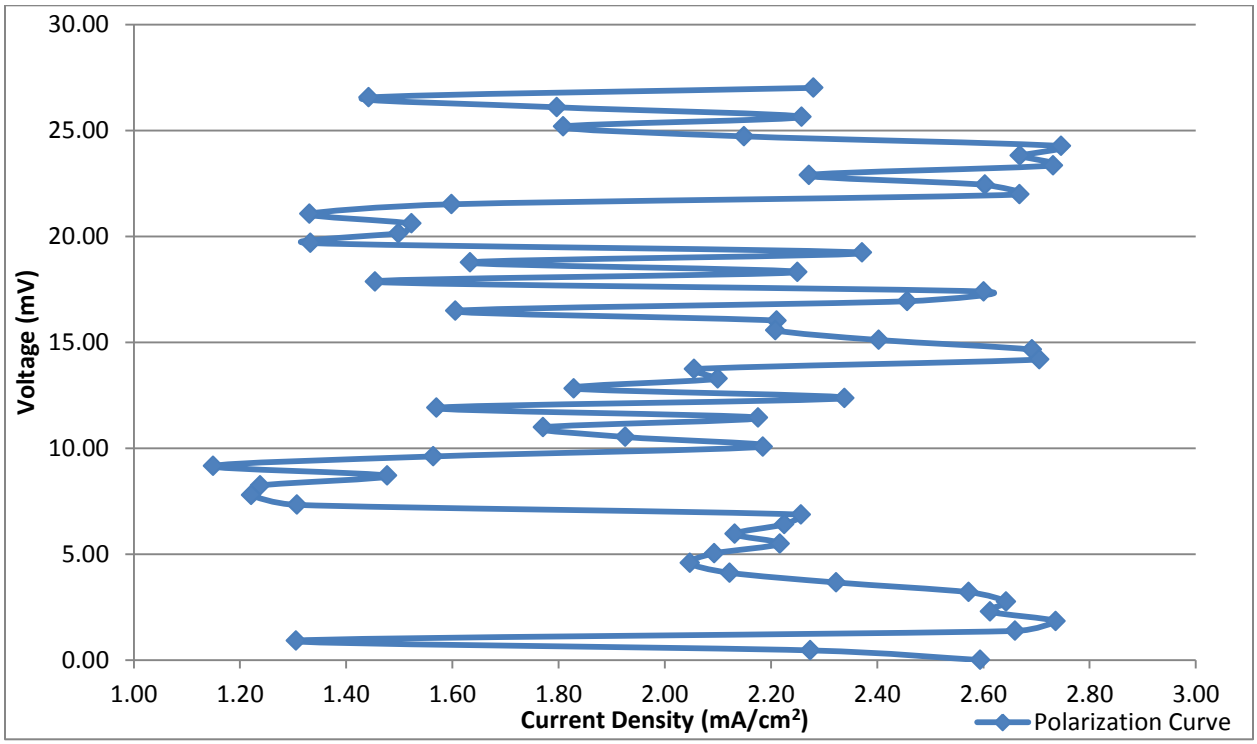

Figure 4.13: H_2/propiopheneone fed, H_3PO_4-doped mPBI-based PEMFC polarization curve for MEA **12**. The temperature of the fuel cell was 140 °C.

Figure 4.14 shows that the ohmic resistance of MEA **11** is 0.23 Ω at 140 °C. EIS was not completed for MEA **12** as the polarization curve shown in Figure 4.13 indicated there would be little point in analyzing an MEA that could not maintain a stable negative slope correlation with respect to the polarization curve when fed H_2 and propiophenone in the fuel cell assembly. The two peaks shown in Figure 4.14 could be the impedance responses of the anode (high frequency, left peak) and cathode (low frequency, right peak). However, as the anode is being fed H_2, the anode impedance would be generally negligible due to the facile reaction kinetics of the hydrogen oxidation reaction (HOR).[6,82] Therefore, the anode impedance would not show as a peak in the EI spectrum.[6] This means that no anode band is visible in the EI spectrum of Figure 4.14. If the reduction of propiophenone was occuring, the two peaks could represent the proposed 2 step reduction process of propiophenone at the cathode,[84] where each peak represents each reduction. The scheme that details the mechanism for the electrochemical reduction of phenyl ketones is shown in Scheme 4.1. However, this two-step reduction mechanism has not been proven beyond a reasonable doubt.[8] The second reduction as proposed in Scheme 4.1 may also be too facile to register in EIS, just like the HOR. As the protonated propiophenone molecule is already adsorbed onto the catalyst surface, adding an electron to the propiophenone molecule from electrically conductive materials (supported carbon and carbon paper) under current load would be relatively quick compared to the first reduction. The first reduction should be slower as a H^+ has to find and connect with the propiophenone molecule whilst it is attached to the catalyst surface in order for the reduction to occur. The most likely explanation for the two bands in Figure 4.14 is that the peak on the left is due to the charge transfer reaction of propiophenone and the right peak represents the mass transfer of the propiophenone from the flow channels to the catalyst layer. A mass transport peak as shown in Figure 4.14 would suggest fuel starvation problems at the cathode.

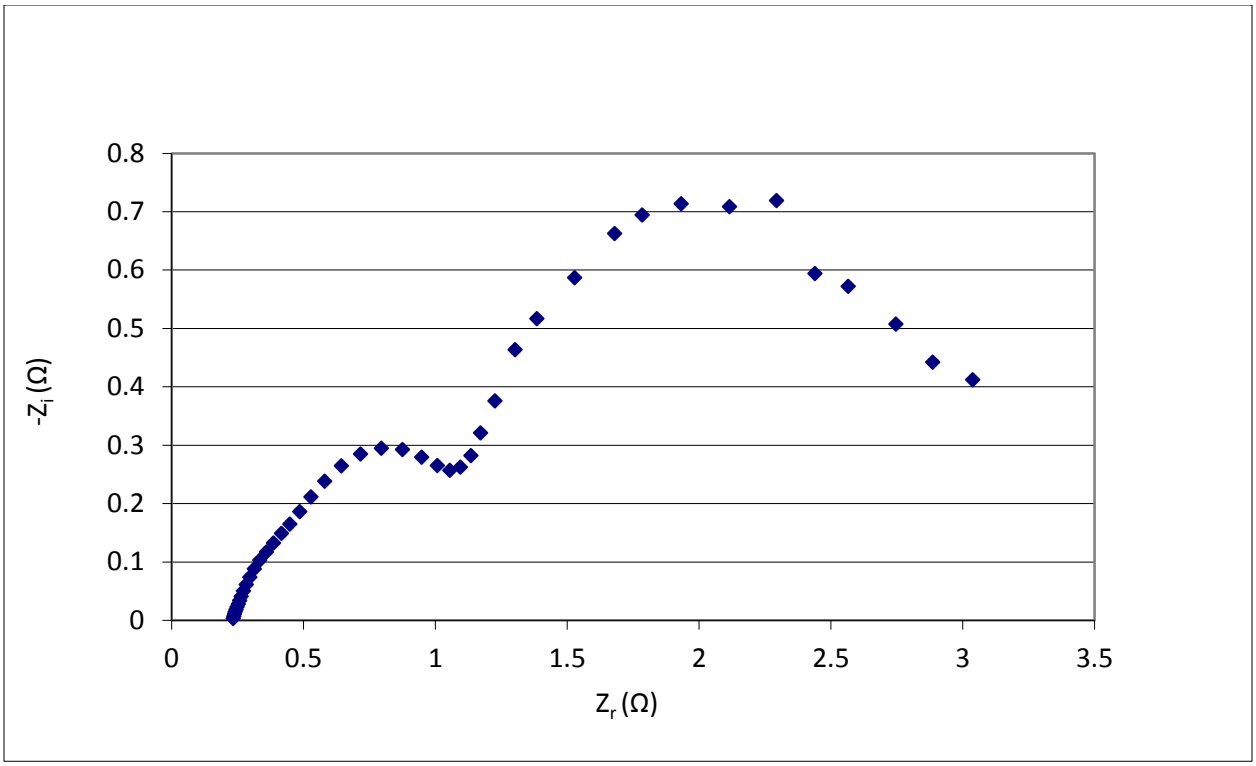

Figure 4.14: Nyquist plot showing the EIS curve for MEA **11** at 140 °C for the H_2/propiopheneone fed, H_3PO_4-doped mPBI-based PEMFC. The frequency range was between 50,000-0.01 Hz. The EI spectrum was measured at 0.08 V and 1.2 mA/cm^2.

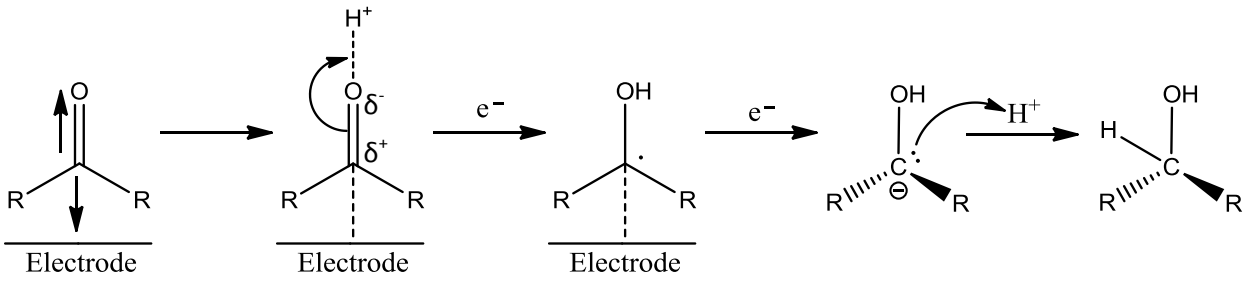

Scheme 4.1: Proposed mechanism for the electrochemical reduction of phenyl ketones.[8,84,85]

A cyclic voltammogram (CV) was collected for MEA **11** when it was inside the fuel cell assembly under active H_2 flow to the anode and propiophenone to the cathode (Figure 4.15). A reduction peak for propiophenone should appear as a negative current in the CV. Previous research by Sharma et al. has placed the reduction of propiophenone on platinum at -671 mV versus a Ag/AgCl reference electrode (-472 mV versus standard hydrogen electrode (SHE)) in 1 M KCl.[86] However, Sharma et al. only detected one peak for the reduction of propiophenone in cyclic voltammetry.[86] The peak at -1140 mV on the uncorrected CV in Figure 4.15 could be the reduction of propiophenone. Significant ohmic resistances will cause a voltage drop and, therefore, shift the reduction peak to more negative potentials. However, when the ohmic resistance of the membrane (0.25 Ω) is taken into account, the reduction potential of this peak is still only -972 mV. Sharma et al. also conducted pH studies on the reduction of propiophenone on platinum.[86] They discovered that the reduction shifts to more positive potentials with a relatively low pH.[86] As the CV shown in Figure 4.15 was completed in the presence of concentrated H_3PO_4, it would suggest that the peak shown at -972 mV is not the reduction of propiophenone. However, Sharma et al. did not complete the CV using a Pd working electrode unlike the CV collected for MEA **11**, which could change the location of the propiophenone reduction peak in the CV.[86]

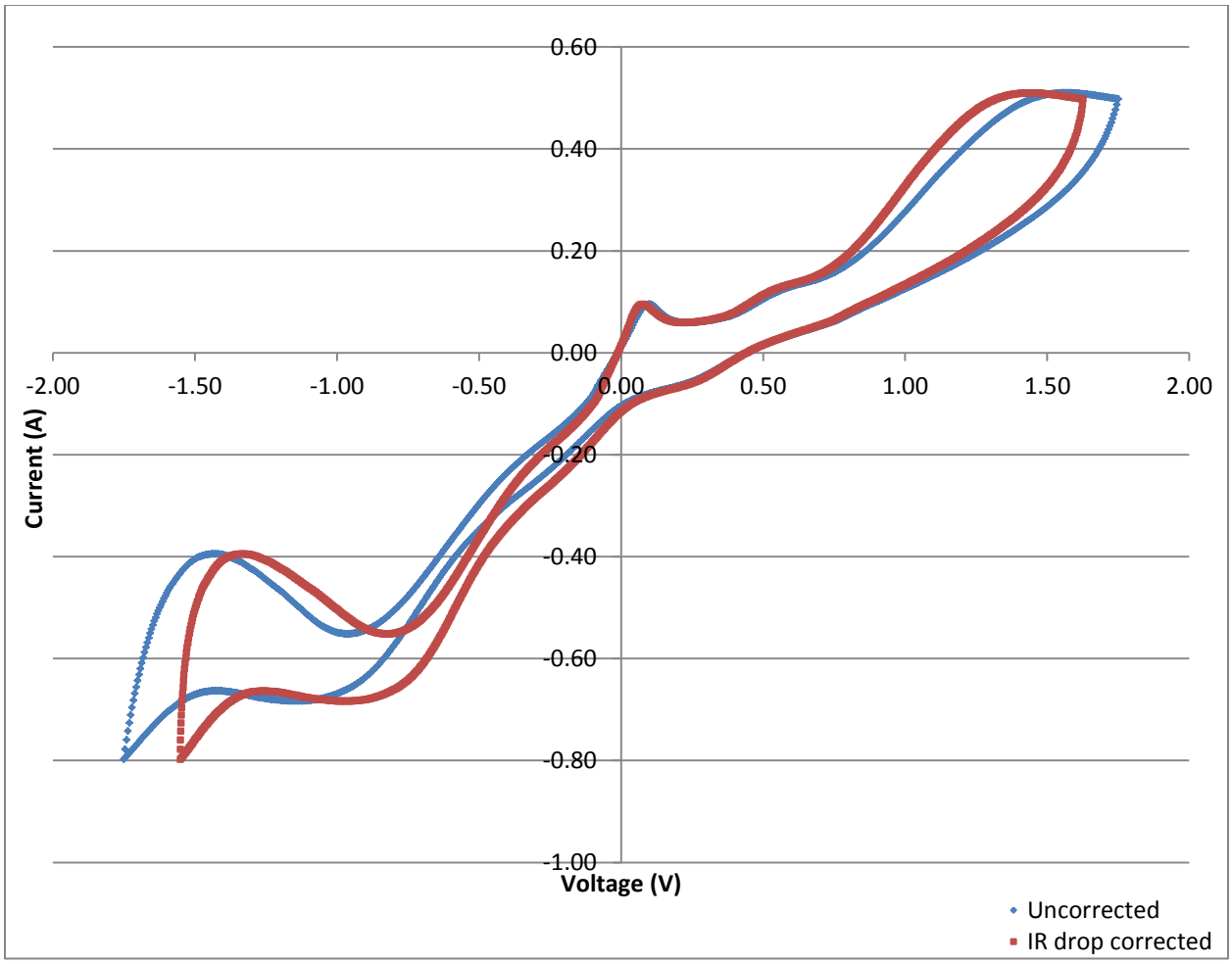

Figure 4.15: Uncorrected and voltage (IR) drop corrected cyclic voltammograms of MEA **11** in an H_2/propiophenone-fed PEMFC. The scan rate was 0.075 V/s at 140 °C. The flow rate of propiophenone was 0 mL/min. The flow rate of H_2 was 0.055 L/min and the fuel cell active area was 5 cm^2.

The oxidation peaks could be from 1-phenyl-1-propanol, an associated reduced product of propiophenone or from the electrodissolution of the palladium surface. The H_2 oxidation peak is not represented on this CV as the H_2 oxidation is on the reference/counter electrode. The electrodissolution of palladium metal could cause a peak to appear between 1.15 and 1.75 V RHE in acidic media under steady state conditions,[87] which would match the peak shown at 1.37 V on the IR drop corrected CV

presented in Figure 4.15. One of the peaks shown at 0.042 mV and -1350 mV on the IR drop corrected CV could be the oxidation product of the previously reduced product observed at -972 mV. However, it is not known which peak would be associated with the reduction peak at -972 mV and whether that reduction peak was actually from propiophenone. It could be that multiple products are being made from the reduction of propiophenone and that these products are associated with the oxidation peaks seen at 0.042 mV and -1350 mV. Many of these products are described by Carrier et al.[11]

Gas chromatography using a flame ionization detector (GC/FID, Shimadsu GC-17A) was used to determine the presence of 1-phenyl-1-propanol in the propiophenone effluent of the fuel cell (using MEA **11**) after 20 min of constant voltage fuel cell operation. The constant voltage was 14 mV, which was determined to be the voltage required to obtain the maximum power density of the fuel cell. The flow rate of propiophenone during this operation was set at 0 mL/min to ensure that the concentration of any 1-phenyl-1-propanol would be high enough in the effluent to detect it by GC/FID. The effluent was collected (1 mL) after the 20 min test and diluted to make a 5 mmol/L solution of propiophenone in HPLC grade MeOH. A small aliquot (2 µL) of this solution was placed inside the GC/FID with a syringe for analysis.

The result of the GC/FID test showed that no 1-phenyl-1-propanol was present in the effluent. The current density remained constant at 0.47 mA/cm^2 for the entire period of the constant voltage test, suggesting that the rates of the fuel cell oxidation and reduction reactions were stable. If there was any dissolved O_2 in the propiophenone, the current density would have significantly decreased over the duration of the test because half of the O_2 would have undergone reduction to H_2O. If the propiophenone was saturated with O_2, then approximately 1.5×10^{-5} mol of O_2 would exist in 1.5 mL (1.5 g) of propiophenone (approximate volume of the flow field plate), assuming the O_2 solubility in propyl benzene (a close relative of propiophenone) is similar to propiophenone.[83] The electrons

produced during the 20 min fuel cell test at a constant current density of 0.47 mA/cm^2 and a 0 mL/min flow rate of propiophenone should have produced either 1.46 x 10^{-5} mol of 1-phenyl-1-propanol or 1.46 x 10^{-5} mol of H_2O using only O_2 as the reducing agent. Therefore, the amount of O_2 consumed if all of the current was attributed to the oxygen reduction reaction would be 7.31 x 10^{-6} mol or 50% of the maximum available total O_2. As the propiophenone was degassed with N_2 before use, it is unlikely that the propiophenone was saturated with O_2. Even if O_2 was present in significant quantities, the current density would have decreased as the rate of diffusion of O_2 through propiophenone decreased. Therefore, it is likely that propiophenone was reduced at the Pd cathode of the fuel cell. However, as 1-phenyl-1-propanol was not present in the effluent from the 20 min test at a constant voltage of 14 mV, it cannot be proven with certainty.

Another GC-FID test was conducted to determine if the 1-phenyl-1-propanol was trapped inside the catalyst bed. MEA **11** was cut such that the membrane surrounding the electrodes was discarded. The remaining piece of the MEA was placed inside a 20 mL glass vial along with 15 mL of HPLC grade methanol and a magnetic stir bar. The mixture was stirred for several hours at room temperature. The methanol was then filtered through a Chromspec 0.45 µm NYL micropore filter to capture any suspended catalyst particles. The methanol filtrate (2 µL) was then injected into the GC-FID for analysis. The method and column used for GC-FID analysis is detailed by Dean.[8] Propiophenone was seen at 5.71 min in the chromatogram, but there were 2 unidentifiable peaks at 1.52 min and 5.59 min. Neither of these peaks matched 1-phenyl-1-propanol, which appeared in a separate analysis at 5.46 min. The peak at 1.51 min is rather large and is present only in very small quantities in the solvent. It is possible that the peak at 1.51 min in the solvent represents a different compound that elutes at the same time as the unknown compound in the methanol wash of MEA **11**. The unknown compounds were determined not to be propyl benzene or 1-cyclohexyl-1-propanol, which appeared at 2.91 min and 5.33 min, respectively in separate chromatograms using the same method and column as described by Dean.[8]

Both propyl benzene and 1-cyclohexyl-1-propanol are possible by-products of the reduction of propiophenone.[11] However, the large unknown peak at 1.51 min in the GC-FID chromatogram could be another product of the electrochemical reduction of propiophenone.

Another possibility could be that the 1-phenyl-1-propanol created by the reduction of propiophenone at the cathode of MEA **11** reacted with H_3PO_4 to produce organic phosphate esters, which has been seen before in H_3PO_4-doped PBI fuel cells.[39] An experiment was conducted to see if these possible esters existed. Treatment of the core of the MEA with a strong acid should release 1-phenyl-1-propanol from any phosphoric acid esters that may have been made during the operation of the fuel cell. Any amount of 1-phenyl-1-propanol collected in the acid could be isolated in an organic solvent and injected in the GC for analysis. The actual procedure consisted of soaking the core of MEA **11** in 37 wt% $HCl_{(aq)}$ for 1 h in a 20 mL glass vial. The mixture was then neutralized by adding concentrated $NaOH_{(aq)}$. The MEA was removed from the mixture and the aqueous solution was extracted with 3 aliquots of chloroform (20 mL). The chloroform was evaporated in a 20 mL glass vial and was replaced by 15 mL of HPLC grade methanol. A small aliquot (2 µL) was injected into the GC-FID for analysis. The chromatogram showed no traces of 1-phenyl-1-propanol but the relatively large peak at 1.51 min was still present. Therefore, no phosphoric acid esters were made according to the GC results. As the peak at 1.51 min from the GC-FID was still present, it is likely that this peak represents the compound that was created when propiophenone was reduced in the fuel cell.

4.6 Conclusion and Recommendations

The MEA components (either 2 GDLs and 1 CCM or 2 CCGDLs and 1 membrane) that were chosen for MEA fabrication were bound together using a hot-press (CHU). However, hot-pressing the H_3PO_4-doped mPBI MEAs could not provide reproducible results when conditions of the CHU were held constant. Some MEAs delaminated at the electrode-membrane interface, while others were damaged with holes inside the membrane. Some MEAs would not fuse together at all in the CHU. However, the best results were seen when the pressure exerted by the CHU was 2,000 lbs using the GPCP or flow field plate assemblies at 130 °C.

SEM-EDS and SEM-BEI micrographs showed that the electrolyte was embedded in the catalyst bed, along with the mPBI binder in MEA **12**. The micrographs also show that the catalyst particles were embedded in and around the H_3PO_4-doped mPBI. The combination of the SEM micrographs with TEM micrographs also demonstrates the size of the H_3PO_4-doped mPBI microfilms. They range from approximately one hundred nanometers to several micrometers in width across the horizontal plane. The three-phase boundary of the catalyst surface, the ionomer (H_3PO_4-doped mPBI), and the fuel pathway (free space) was also seen by TEM, which proves that at least some of the catalyst particles are catalytically active to the reactants of the fuel cell.

Polarization and power density curves suggest that the best maximum power density from all of the MEAs tested is approximately half as much as the power density detailed by Mader et al. for a H_2/air fed H_3PO_4-doped mPBI PEMFC.[33] However, the catalyst loading in the catalyst bed was also approximately half for the MEAs **3**, **5-7**, **9-13** (~0.5 mg Pd or Pt/cm^2) compared to the H_3PO_4-doped mPBI PEMFCs shown by Mader et al. (1.0 mg Pt/cm^2).[33] The OCV was also less than the values described by

Mader et al.[33] This could be due to mixed potentials caused by reactant crossover or the electrochemical reduction or oxidation of impurities. Many of the MEAs tested in this work could not exceed a current denisty of 0.02 A/cm^2 when placed inside a H_2/air fed fuel cell. This could be due to poor diffusivity of H_2 and O_2 in the catalyst bed caused by large mPBI films or high localized H_3PO_4 concentrations inside the catalyst bed. Another cause of the low current density could be $H_2PO_4^-$ adsorbing onto the surface of the catalyst, which would deactivate it for the ORR.[81] There are many variables that have to be accounted for in the manufacture of MEAs. Some of these variables include ink deposition technique and evaporation rate of the ink solvent from the electrode surface; membrane casting solvent and temperature of evaporation; hot-pressing pressure and temperature; gasket material and the amount of torque to apply to the screws of the fuel cell assembly. It would take much more experimentation to find the correct conditions to build an MEA for a particular polymer/catalyst bed combination.

For the H_2/propiophenone fed H_3PO_4-doped mPBI PEMFC, the maximum power density achieved was 6.23 μW/cm^2. This is approximately 30 times less than the unoptimized acetone/isopropanol fed TRFC system tested by Ando et al.[7] This may be because a lot of the catalyst surface may have been deactivated by the presence of adbsorbed Cl^- and $H_2PO_4^-$ as evidenced by the poor H_2/air fed fuel cell performance. Another possibility could be that the electrochemical reduction reaction of propiophenone is too slow to produce a power density similar to Ando's system. The constant voltage test conducted on MEA **11** suggested that propiophenone was being reduced at the cathode. However, 1-phenyl-1-propanol could not be definitively proven as the product of this reduction by EIS, CV or the polarization and power density curves of MEA **11** fed by H_2 and propiophenone inside the fuel cell. GC/FID of the effluent and of the MEA core wash could also not prove the existence of 1-phenyl-1-propanol as the electrochemical reduction product of propiophenone. However, there was an unknown substance that was identified by both GC analyses that could be the product of the

propiophenone reduction. As 1-phenyl-1-propanol was not discovered in the extracted HCl wash of the MEA **12** core, 1-phenyl-1-propanol did not react with H_3PO_4 to produce phosphoric acid esters.

The viability of the proposed TRFC system was not verified. The leaching of H_3PO_4 from the MEA makes it impossible to use H_3PO_4-doped PBI as the electrolyte in the final version of the MEA in the TRFC system. The loss of H_3PO_4 would reduce the power density of the fuel cell over time as fewer protons are able to be transported from anode to cathode. Focus should now be shifted to sulfonated polymers that operate in the presence of water rather than H_3PO_4 to avoid the leaching of the electrolyte. Additional work, beyond the scope of this thesis, would be required to determine what is being reduced at the cathode of the MEA when fed with propiophenone.

References

1. Coley, D. *Energy and climate change: Creating a sustainable future*; John Wiley and Sons Ltd: Chichester, 2008.
2. Pennisi, E., *Science*, **1999**, 283, 2004.
3. U.S. Energy Information Administration (unknown author(s)). *International Energy Statistics, Petroleum Production and Consumption*, 1980-2010. http://www.eia.gov/cfapps/ipdbproject/IEDIndex3.cfm?tid=5&pid=5&aid=8 (accessed September 10, 2012)
4. Capeleiro Pinto, A. C.; Branco, C. C. M.; de Mastos, J. S.; Vieira, P. M.; da Silva Guedes, S.; Pedroso Jr, C.; Decnop Coelho, A. C.; Ceciliano, M. M.; Petrobras S. A. *Offshore Technology Conference*, **2003**, 15283.
5. Sørensen, B. *Renewable Energy: Physics, Engineering, Environmental Impacts, Economics and Planning,* 4th Ed.; Academic Press: Burlington, MA, 2011.
6. O'Hayre, R.; Cha, S. W.; Colella, W.; Prinz, F. B. *Fuel Cell Fundamentals*, 2nd Ed.; John Wiley and Sons Inc: Hoboken, NJ, 2009.
7. Ando, Y.; Tanaka, T.; Doi, T.; Takashima, T. *Energy Convers. Manage.*, **2001**, 42, 1807-1816.
8. Dean, D. *Hydrogen Fuel Technologies for Vehicular Transportation.* Ph.D. Thesis, Queen's University, 2012.
9. Demidoven, N.; Deutch, J. *Science,* **2004**, 305, 974-976.
10. J. P. Hermans, *Basic Research Needs to Assure a Secure Energy Future* – DOE Report from the Basic Energy Sciences Advisory Committee, 2003. (http://science.energy.gov/~/media/bes/besac/pdf/Basic_research_needs_to_assure_a_secure_energy_future_feb_2003.pdf)

11. Carrier, A.; Dean, D.; Little, V. R.; Vandersleen, J.; Davis, B.; Jessop, P. G. *Energy Environ. Sci.,* **2012**, 5, 7111-7123.
12. Ando, Y.; Aoyama, Y.; Sasaki, T.; Saito, Y.; Hatori, H.; Tanaka, T. *Bull Chem. Soc. Jpn.,* **2004**, 77, 1855-1859.
13. Akimoto, K. *Jp. Pat. 2007287357 A, November 1, **2007.***
14. Spiegel, C. S. *Designing and Building Fuel Cells*, 1st Ed.; McGraw Hill: New York, NY, 2007.
15. Thomas, C. E. *Int. J. Hydrogen Energy,* **2009**, 34, 6005-6020.
16. Ma, Y. L.; Wainright, J. S.; Litt, M. H.; Savinell, R. F. *J. Electrochem. Soc.*, **2004**, 151, A8-A16.
17. Zhang, J.; Zhang, J.; Tang, Y.; Song, C. *J. Power Sources*, **2007**, 72, 163-171.
18. Ariza, M. J.; Jones, D. J.; Rozière, J. *Desalination*, **2002**, 147, 183-189.
19. Pivovar, B. S.; Wang, Y.; Cussler, E. L. *J. Mem. Sci.*, **1999**, 154, 155-162.
20. Toshida, T.; Tokumasu, T. *ECS. Trans.,* **2010**, 33, 1055-1066.
21. Litster, S.; McLean, G. J. *Power Sources,* **2004**, 130, 61-76.
22. Weber, A. Z.; Newman, J. *J. Electrochem. Soc.,* **2005**, 152, A677-A688.
23. Wang, Y.; Wang, C. Y.; Chen, K. S. *Electrochim. Acta,* **2007**, 52, 3965-3975.
24. Wang, H.; Yuan, X. Z.; Li, H. *PEM Fuel Cell Diagnostic Tools*: CRC Press: Boca Raton, FL, 2012.
25. Yu, Y.; Tu, Z.; Zhang, H.; Pan, M. *J. Power Sources,* **2011**, 196, 5077-5083.
26. Zhao, D.; Yi, B.L.; Zhang, H. M.; Liu, M. *J. Power Sources*, **2010**, 195, 4600-4612.
27. Zhai, Y.; Zhang, H.; Liu, G.; Hu, J.; Yi, B. *J. Electrochem. Soc.,* **2007**, 154, B72-B76.
28. Wang, Z.; Tang, H.; Pan, M. *J. Power Sources,* **2011**, 369, 250-257.
29. Base, A. B.; Shaik, R.; Mawdsley, J. *J. Power Sources,* **2008**, 182, 61-65.
30. Gurau, V.; Mann Jr., J.A. *Advances in Mechanical Engineering*, **2010**, 37, 2795.
31. Chatenet, M.; Dubau, L.; Job, N.; Maillard, F. *Catal. Today*, **2010**, 156, 76-86.
32. Kamat, A.; Huth, A.; Klein, O.; Scholl, S. *Fuel Cells 10,* **2010**, 6, 983-992.

33. Mader, J.; Xiao, L.; Schmidt, T. *J. Adv. Polym Sci.,* **2008**, 216, 63-124.

34. Seland, F.; Berning, T.; Børresen, B.; Tunold, R. *J. Power Sources,* **2006**, 160, 27-36.

35. Busby, R. L. *Hydrogen and Fuel Cells: A Comprehensive Guide*. Penwell: Tulsa, OK, 2005.

36. Ito, H.; Hasegawa, Y.; Ito, Y.; *J. Appl. Electrochem.,* **2005**, 35-507-512.

37. Angus, J. C. *Adv. Chem.,* **1967**, 64, 11-16.

38. Carrier, A. *The Transportation and Transformation of Energy through Reversible Hydrogenation.* Ph.D. Thesis, Queen's University, 2011.

39. Allward, T. *Membrane Electrode Assembly Fabrication and Test Method Development For a Novel Thermally Regenerative Fuel Cell Concept*. M.Sc Thesis, Queen's University, 2012.

40. Bozkurt, A. *Synthesis and Characterization of Proton Conducting Polymer Electrolytes Based on Phosphoric Acid.* Ph.D. Thesis, Universität zu Mainz; 1999.

41. Asensio, J. A.; Borrós, S.; Gómez-Romero, P. *Electrochim. Acta,* **2004**, 49, 4461-4466.

42. Boerstoel, H.; Maatman, H.; Westerink, J. B.; Koenders, B. M. *Polymer*, **2001**, 42, 7371-7379.

43. Kamide, K.; Miyamoto, I.; Okajima, K. *Polym. J.*, **1993**, 25, 453-461.

44. Pinar, F. J.; Ca*ñizares, P.; Rodrigo, M. A.; Úbeda, D.; Lobato, J. J. Power Sources,* **2011**, 196, 4306-4313.

45. Li, N.; Li, S.; Zhang, S.; Wang, J. *J. Power Sources,* **2009**, 187, 67-73.

46. Ping-Lin, K.; Wei-Fu, C.; Wuu-Jyh, L. *J. Polym. Sci., Part A: Polym. Chem.,* **2005**, 43, 3359-3367.

47. Taylor, A. D.; Michel, M.; Sekol, R. C.; Kizuka, J. M.; Kotov, N. A.; Thompson, L.T. *Adv. Funct. Mater.,* **2008**, 18, 3003-3009.

48. Bozkurt, A.; Ise, M.; Kreuer, K. D.; Meyer, W. H.; Wegner, G. *Solid State Ionics,* **1999**, 125, 225-233.

49. Bozkurt, A*. Turk J. Chem.,* **2002**, 26, 663-668.

50. Parcero, E.; Herrera, R.; Nunes, S. P. *J. Membr. Sci.,* **2006**, 285, 206-213.

51. Ningping, C.; Liang, H. *Solid State Ionics,* **2002**, 377-385.

52. Zhao, J.; Yuan, W. Z.; Anhou, A.; Lu, Y.; Zhang, Y. *Reactive and Functional Polymers,* **2011**, 71, 1102-1109.

53. Hong, W.; Stucky, G. D.; Tasaki, K. *US. Pat. 20060148953 A1 20060706,* **2006.**

54. Saha, M. S.; Malevich, D.; Halliop, E.; Pharoah, J. G.; Peppley, B. A.; Karan, K. *J. Electrochem. Soc.,* **2011**, 158, B562-B567.

55. Ngo, T. T.; Yu, T. L.; Lin, H. L. *J. Power Sources,* **2013**, 225, 293-303.

56. Atkins, P.; De Paula, J. *Atkins' Physical Chemistry,*8th Ed.; W. H. Freeman and Company: New York, 2006.

57. Kamlet, M. J.; Abboud J-L. M.; Abraham, M. H.; Taft, R. W. *J Org. Chem.,* **1983**, 48, 2877-2887.

58. Hellal, F.; Phan-Tan-Luu, R.; Siouffi, A. M. *J. Liq. Chromatogr.,* **1994**, 17, 2845-2869.

59. Huang, D. C.; Yu, P. J.; Liu, F. J.; Huang, S.L.; Hsueh, K.L.; Chen, Y.C.; Wu, C.H.; Chang, W.C.; Tsau, F.H. *Int. J. Electrochem. Sci.,* **2011**, 6, 2552-2565.

60. Sample, T. E.; Hatch, L. F. *J. Chem. Educ.,* **1968**, 45, 55-56.

61. Steinbach, A. J.; Hamilton Jr., C. V.; Debe, M. K. *ECS Trans.,* **2007**, 11, 889-902.

62. Östlund, Å.; Lundberg, D.; Nordstierna, L.; Holmberg, K.; Nydén, M. *Biomacromolecules,* **2009**, 10, 2401-2407.

63. Morgan, R. J.; Butler, N. L. *Polym. Bull.,* **1992**, 27, 689-696.

64. Tanner, D.; Fitzgerald, J. A.; Phillips, B. R. *Adv. Mater.,* **1989**, 1, 151-156.

65. Li, H.; Zhang, S.; Qian, W.; Yu, Y.; Yuan, X. Z.; Wang, H.; Jiang, M.; Wessel, S.; Cheng, T. T. H. *J. Power Sources,* **2012**, 218, 375-382.

66. Seo, M.; Aomi, M. *J. Electroanal. Chem.,* **1993**, 347, 185-194.

67. Holleman, A. F.; Wiberg, E. *Inorganic Chemistry. Academic Press:* San Diego, CA, 2001.

68. Kozuka, H.; Ishikawa, Y.; Ashibe, N. *Journal of Sol Gel Science and Technology,* **2004**, 31, 245-248.

69. Mader, J. A. *Novel Sulfonated Polybenzimidazole Derivatives for High Temperature Fuel Cell Applications. Ph.D. Thesis, Rensselaer Polytechnic Institute,* 2010.
70. Glipa, X.; Haddad, M. E.; Jones, D. J.; Rozière, J. *Solid State Ionics*, **1997**, 97, 323-331.
71. Paulson, F. G.; Shajaie, S. S.; Krantz, W. B. *J. Membr. Sci.,* **1994**, 91, 265-282.
72. Li, Q.; He, R.; Berg, R. W.; Hjuler, H. A.; Bjerrum, N. J. *Solid State Ionics,* **2004**, 168, 177-185.
73. Lund Myhre, C. E.; Christensen, D. H.; Nicolaisen, F. M.; Nielsen, C. J. *J. Phys. Chem. A.*, **2003**, 107, 1979-1991.
74. Peron, J.; Ruiz, E.; Jones, D. J.; Rozière, J. *J. Membr. Sci.,* **2008**, 314, 247-256.
75. Ayers, G. P.; Gillet, R. W.; Gras, J. L. *Geophys. Res. Lett.,* **1980**, 7, 433-436.
76. Nasirzadeh, K.; Neueder, R.; Kunz, W. *J. Chem. Eng. Data.,* **2005**, 50, 26-28.
77. Kongstein, O. E.; Berning, T.; Børresen, B.; Seland, F.; Tunold, R. *Energy*, **2007**, 32, 418-422.
78. Kim, S.; Khandelwal, M.; Chacko, C.; Mench, M. M. *J .Electrochem. Soc.,* **2009**, 156, B99-B108.
79. Chen, C. Y.; Lai, W. H. *J. Power Sources,* **2010**, 195, 7152-7159.
80. Zhang, J.; Tang, Y.; Song, C.; Zhang, J.; Wang, H. *J. Power Sources,* **2006**, 532-537.
81. Neyerlin, K. C.; Singh, A.; Chu, D. *J. Power Sources,* **2008**, 176, 112-117.
82. Kondratenko, M. S.; Gallyamou, M. O.; Khokhlov, A. R. *Int. J. Hydrogen Energy,* **2012**, 37, 2596-2602.
83. Battino, R.; Rettich, T. R.; Tominaga, T. *J. Phys. Chem. Ref. Data,* **1983**, 12, 163-178.
84. Elving, P. J.; Leone, J. T. *J. Am. Chem. Soc.,* **1957**, 80, 1021-1029.
85. Davies, W. C.; Evans, D. P. *J. Chem. Soc.,* **1939**, 546-554.
86. Sharma, A.; Ojha, P.; Verma, P. S.; Sharma, I. K. *International Journal of Applied Biology and Pharmaceutical Technology,* **2011**,2, 277-286.
87. Grdeń, M.; Łukaszewski, M.; Jerkiewicz, G.; Czerwiński, A. *Electrochim. Acta*, **2003**, 53, 7583-7598.

Appendix - Figures

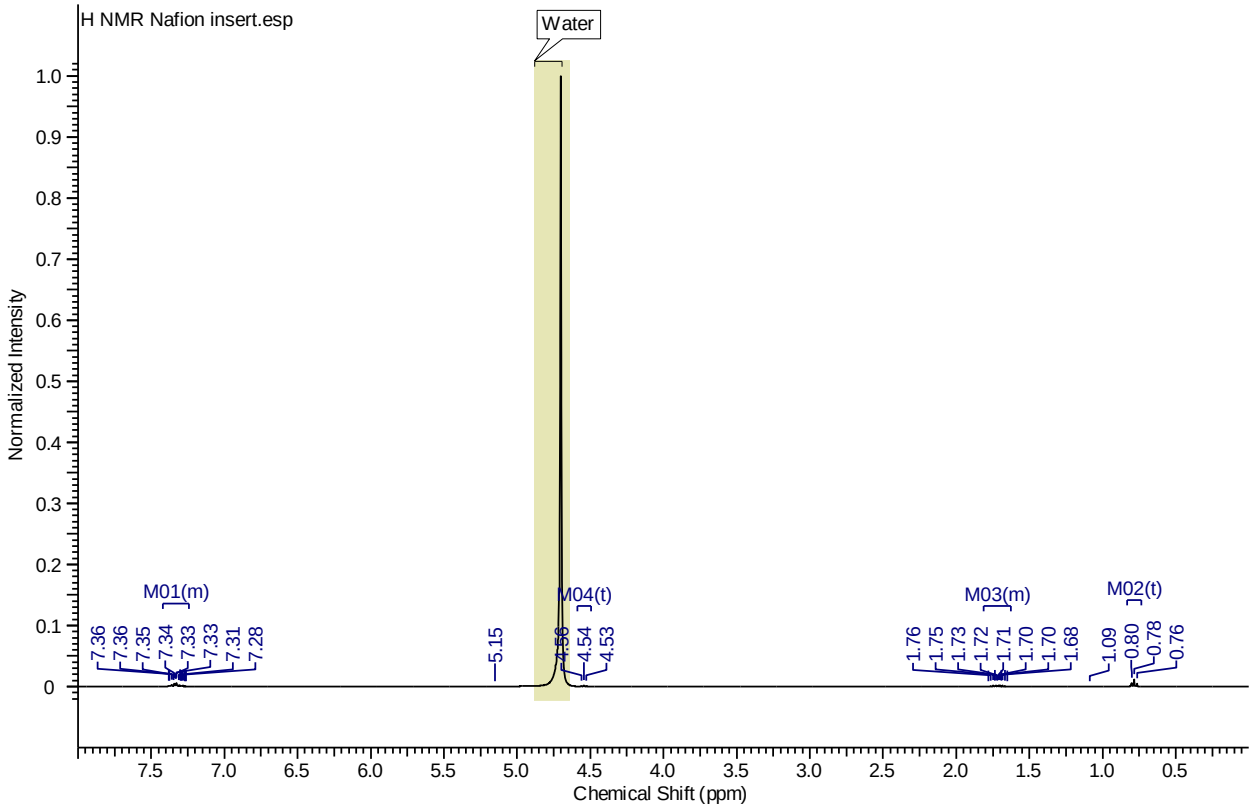

Figure A1: ^{1}H NMR spectrum of the second fluid phase in D_2O, 298 K that was present after exposing a membrane of Nafion® to a mixture of 96 wt% 1-phenyl-1-propanol and 4 wt% propiophenone. The spectrum shows water as the main component of the sample. M01-M04 represents 1-phenyl-1-propanol.

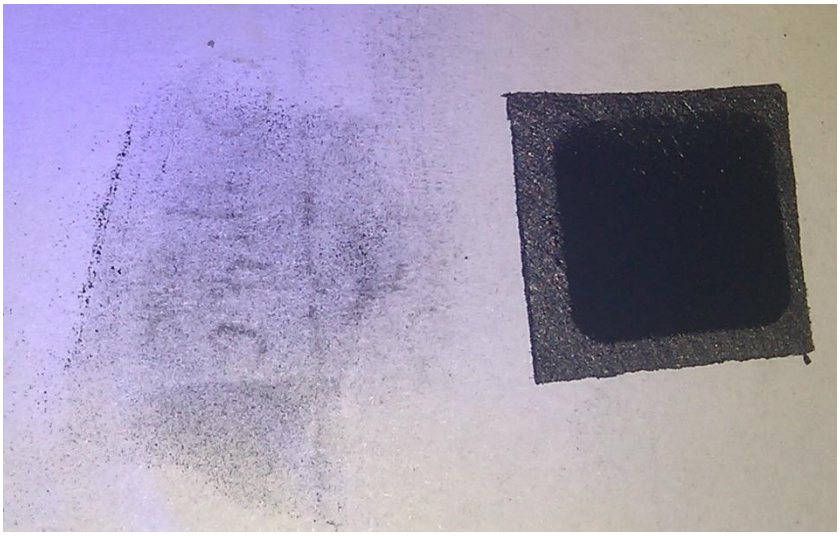

Figure A2: At right, a Nafion®-based CCGDL after exposure to 1-phenyl-1-propanol for 1 h at 130 °C. At left, catalyst powder that was easily removed by abrasion of the pictured CCGDL onto the white paper surface.

A) 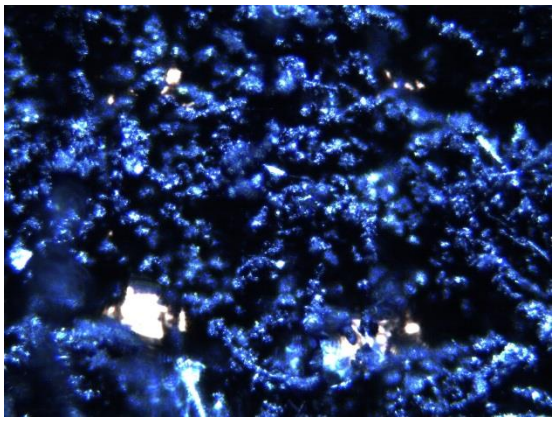 B) 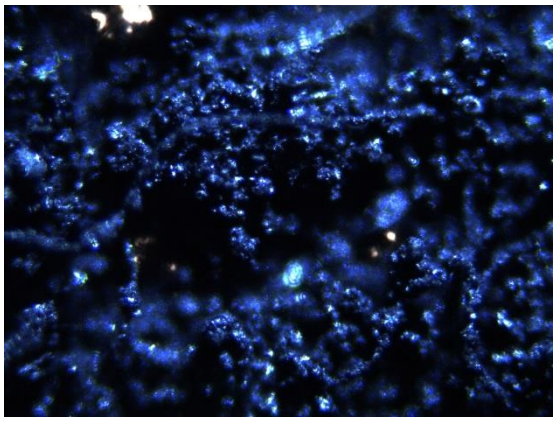

Figure A3: Micrographs that depict the effect of glycerol on the deposition of Vulcan XC-72 carbon onto the surface of a carbon paper GDL. A) The surface of the Vulcan XC-72-coated carbon paper GDL. The ink that was used to deposit the Vulcan XC-72 contained glycerol (Table 3.10, trial **B**). B) The surface of the Vulcan XC-72-coated carbon paper GDL. The ink that was used to deposit the Vulcan XC-72 contained no glycerol B (Table 3.10, trial **C**).

A) 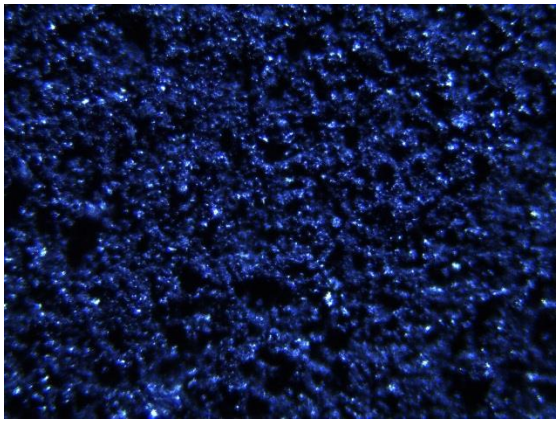 B) 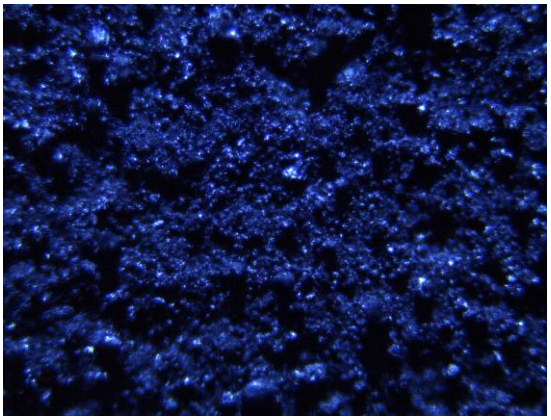

Figure A4: A) A micrograph of the first layer of Vulcan XC-72 for a DPS PBI-based CCGDL (trial **D**, Table 3.10). B) A micrograph of the second layer of Vulcan XC-72 for the same trial. Magnification for both is 10x.

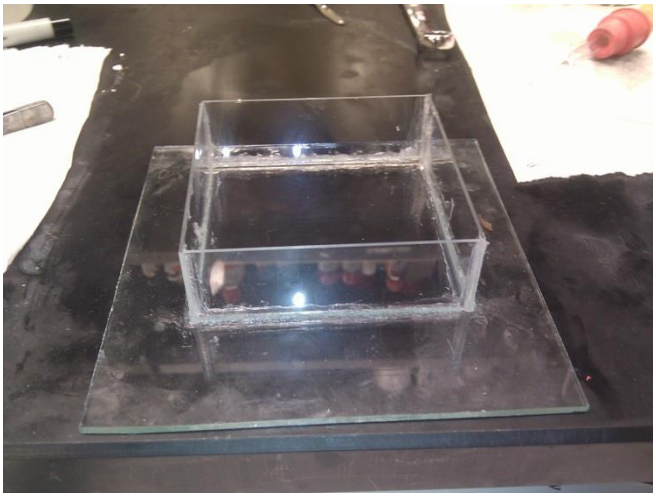

Figure A5: A template that consisted of a plate glass floor and plate glass walls (microscope slides). The template was used in an attempt to make PBI S26 membranes (procedure described in chapter 2.4.2).

Figure A6: A template for casting PBI S26 that consisted of a plate glass floor and a steel cylinder wall. The template was used to make PBI S26 membranes (procedure described in chapter 2.4.2).

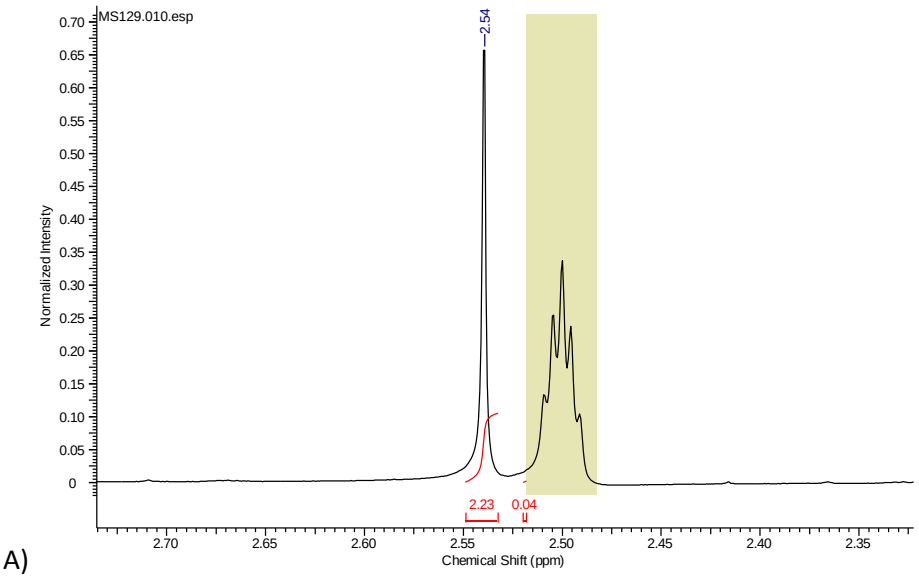

A)

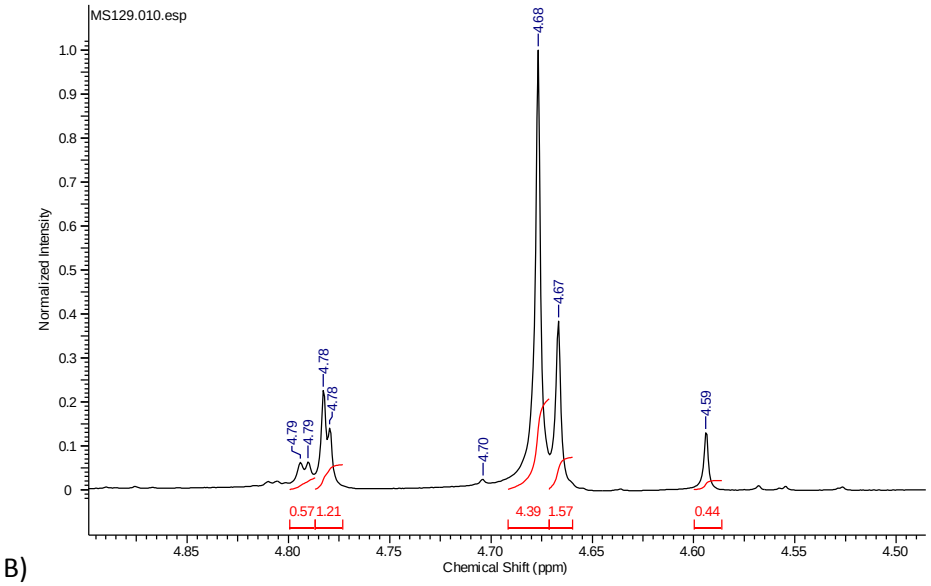

B)

Figure A7: A-B) ^{1}H NMR spectrum in DMSO-d_6 of the unknown plasticizer in PBI 0.8IV.

C)

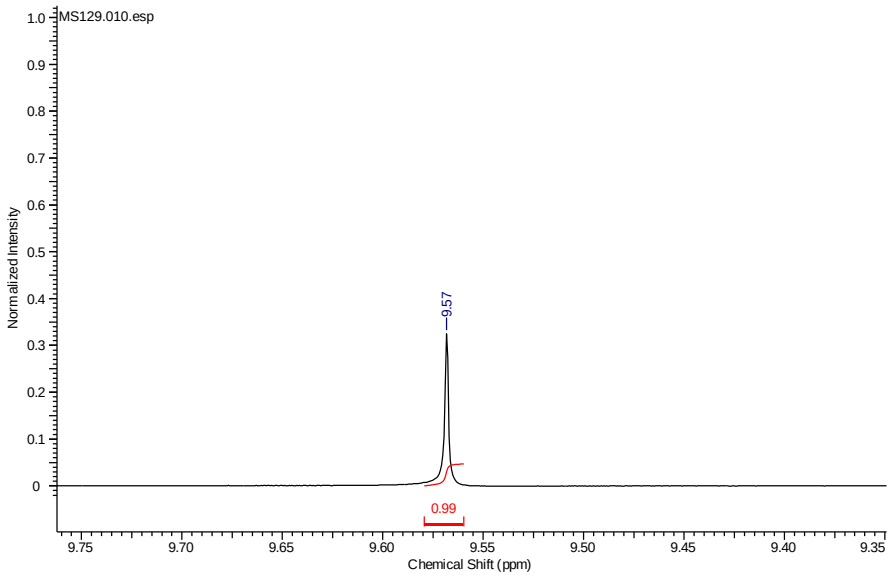

Figure A7 continued: C) ^{1}H NMR spectrum in DMSO-d_6 of the unknown plasticizer in PBI 0.8IV.

A) B) C)

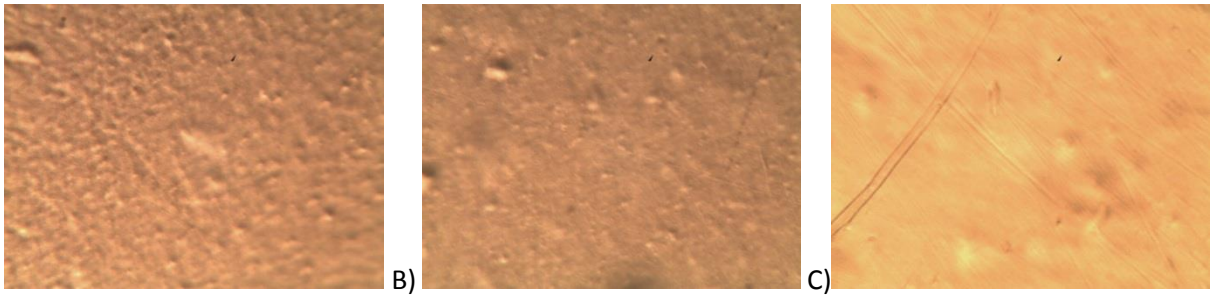

Figure A8: CDPS PBI membranes at 100x magnification. The membranes were orange in colour. A) Non-doped CDPS PBI membrane. B) H_3PO_4-doped (~2.1 eq PRU mPBI) CDPS PBI membrane. C) H_3PO_4-doped (~2.1 eq PRU mPBI) CDPS PBI membrane after exposure to a mixture of 85 wt% 1-phenyl-1-propanol and 15 wt% propiophenone for 21 h at 140 °C.